This electronic thesis or dissertation has been downloaded from the King's Research Portal at https://kclpure.kcl.ac.uk/portal/

Black Holes and Vacuum Tunnelling and Scattering

Hu, Shiqian

Awarding institution:
King's College London

The copyright of this thesis rests with the author and no quotation from it or information derived from it may be published without proper acknowledgement.

END USER LICENCE AGREEMENT

Unless another licence is stated on the immediately following page this work is licensed under a Creative Commons Attribution-NonCommercial-NoDerivatives 4.0 International licence. https://creativecommons.org/licenses/by-nc-nd/4.0/

You are free to copy, distribute and transmit the work

Under the following conditions:

- Attribution: You must attribute the work in the manner specified by the author (but not in any way that suggests that they endorse you or your use of the work).
- Non Commercial: You may not use this work for commercial purposes.
- No Derivative Works - You may not alter, transform, or build upon this work.

Any of these conditions can be waived if you receive permission from the author. Your fair dealings and other rights are in no way affected by the above.

Take down policy

If you believe that this document breaches copyright please contact librarypure@kcl.ac.uk providing details, and we will remove access to the work immediately and investigate your claim.

Download date: 06. Oct. 2025

Black Holes and Vacuum

Tunnelling and Scattering

Shi-Qian Hu

Supervisor: Prof. Ruth Gregory

The Department of Physics
King’s College London

This dissertation is submitted for the degree of
Doctor of Philosophy

January 2025

I would like to dedicate this thesis to my loving parents, family and friends.

Declaration

I hereby declare that except where specific reference is made to the work of others, the contents of this thesis are original and have not been submitted in whole or in part for consideration for any other degree or qualification in this, or any other university.

This thesis is my own work and includes papers that have been carried out in collaboration with Ruth Gregory, Theo Torres, Mohamed Ould El Hadj, Louis Hamaide, Lucien Heurtier, and Andrew Cheek.

Part of the thesis has been published in the following papers:

- L. Hamaide, L. Heurtier, S.Q. Hu, & A. Cheek. Primordial Black Holes Are True Vacuum Nurseries, *Physics Letters B*, 856 138895 , 2024.
- R. Gregory, S.Q. Hu. Testing Higher Derivative Gravity through Tunnelling, *Particles*, 7(1):144-160, 2024.
- R. Gregory, S.Q. Hu. Seeded vacuum decay with Gauss-Bonnet. *Journal of High Energy Physics*, 11 072, 2023.
- T. Torres, M. Ould El Hadj, S.Q. Hu, R. Gregory, Regge pole description of scattering by dirty black holes, *Physical Review D* 107, 064028, 2023.

Shi-Qian Hu
January 2025

Acknowledgements

First and foremost, I would like to express my deepest gratitude to my supervisor, Prof. Ruth Gregory, who has always been a role model for me in theoretical physics. Thanks for her motivation, support, and encouragement throughout my journey. I particularly appreciate for her providing me (and the group) with the opportunity to visit the Perimeter Institute and spend quality time in Canada. Besides academics, her efforts in driving us on travels and hosting weekend dinners made me feel like having an academic family living on the other side of the world. I am also extremely grateful for all the direct and helpful suggestions she provided at every step of my PhD journey.

I would also like to extend my heartfelt thanks to Xiao-Mei Kuang, Yen Chin Ong, De-chang Dai and Kang Zhou for introducing me to the field of theoretical physics and for their continuous support since my time as a Master's student.

I feel incredibly fortunate to have been surrounded by so many wonderful friends and colleagues during my time at King's College London. My deepest thanks to everyone at TPPC for creating such an excellent work environment and for all the memorable moments we shared. I am truly grateful to be part of TPPC, thanks to Angelo, Ansh, Ben, Charlie, Chiara, Clelia, Claire, Damon, Drew, Eloy, John, Kai, Leonardo, Lewis, Leqian, Liina, Louis, Matt, Max, Michelle, Mudit, Nick, Nicole, Panos, Victor for making this journal special. Thanks to Jingyi and Yi for your friendship and unwavering support.

I would like to express my sincere gratitude to my collaborators, Andrew Cheek, Louis Hamaide, Lucien Heurtier, Mohamed Ould El Hadj and Theo Torres, for many intriguing discussions and enjoyable collaborative projects. Special thanks to Wenyuan Ai, Lucien Heurtier, and Malcolm Fairbairn for your support with my postdoc applications.

Thanks to my partner for endless patience and wonderful companionship over the past three years, making my time in London truly special.

Last but not least, I would like to thank my parents for their unconditional love and support throughout my life. Thanks to my brother and his wife, my niece and nephew for being lovely family members, which bring me great comfort and joy. I would not be who I am without your never-ending love and encouragement.

I am grateful to the KCSC scholarship scheme that supports my PhD and to the Department of Physics at King's College London for providing travel expenses to attend conferences and academic visits. Thank Perimeter Institute for hosting and accommodating me during my visits in 2023 and 2024. Thanks to Quantum Simulator and Fundamental Physics collaboration for financing my trip to QSimFP 2nd workshop at Perimeter Institute and Analogy Gravity meeting in Benasque in 2023.

Abstract

Black holes are very mysterious objects that can be studied mathematically in General Relativity as they are solutions to Einstein equations, providing intriguing insights into the nature of gravity and spacetime. Recent advancements in the observation of black holes, including the detection of gravitational waves and the images of black holes, have not only confirmed theoretical predictions but also opened new avenues for exploring novel physics.

In this thesis, we focus on different aspects of black holes. The first part is related to the decay of false vacuum catalysed by black holes, while the second part studies the scattering phenomena of plane monochromatic scalar waves impinging upon black holes.

False vacuum decay is a first-order phase transition that happened in the early universe and plays an essential role in the metastability of the electroweak vacuum, baryogenesis creates baryon anti-baryon asymmetry, modifies and sets the dark matter abundance, can create a large abundance of primordial black holes, can create magnetic fields, and produce a stochastic gravitational waves background.

Recent literature suggests that the presence of small black holes can drastically increase the decay rate, while their Hawking radiation is significant enough to reheat the surrounding plasma locally, forming hot spots that survive throughout their lifetime. We use the temperature profile of such hot spots to calculate the decay rate of metastable vacua in cosmology and apply the formalism to constrain the primordial black hole abundance. We also investigate false vacuum decay catalysed by black holes under the influence of the higher order Gauss-Bonnet term, studying both bubble nucleation and Hawking-Moss types of phase transition in arbitrary dimensions. The signatures of higher derivative terms can be captured through the tunnelling processes.

The second part of the thesis studies the problem of plane monochromatic scalar waves impinging upon a Schwarzschild dirty black hole using the complex angular momentum

approach. We recap general results concerning the differential scattering cross-section in the classical limit through a null geodesic analysis by exploring different configurations of the shell. We compute the Regge pole spectrum for various shell configurations, providing the complex angular momentum representation of the differential scattering cross-section, and examine the role of the different Regge pole branches. Also, we show the critical effects - orbiting, glory, grazing and rainbow scattering, and their impact on the differential scattering cross-section.

Table of contents

List of figures **11**

List of tables **18**

Nomenclature **19**

1 Introduction **21**

2 Black holes **26**

2.1 History of Black holes 26

2.2 Modern evidence of black holes 28

2.3 Primordial black holes 29

2.4 Other aspects of black holes 31

2.4.1 Black hole solution in modified gravity 31

2.4.2 Dirty black hole 32

3 Quantum tunnelling **34**

3.1 Tunnelling in quantum mechanics 35

3.2 Instanton and bounce 36

3.2.1 Euclidean path integral 36

3.2.2 The double well and instantons 40

3.2.3 Unstable states and bounces 44

3.3 Tunnelling in quantum field theory 46

3.4 Tunnelling in curved spacetime 51

3.5 Seeded tunnelling 53

3.5.1 Bubble dynamics and decay rate . . . 53
3.5.2 Hawking Moss transition . . . 55

4 False vacuum decay with primordial black holes 58
4.1 Introduction . . . 58
4.2 Bubble action . . . 59
4.3 Thermal profile around PBHs . . . 61
4.4 Bounce solution and nucleation rate . . . 64
4.5 The Electroweak Vacuum . . . 66
4.6 Primordial black hole bounds . . . 67
4.7 Summary . . . 69

5 Seeded Vacuum Decay with Gauss-Bonnet 71
5.1 Introduction . . . 71
5.2 Bubble-nucleated decay . . . 74
5.2.1 The instanton solution . . . 75
5.2.2 Computing the instanton action . . . 78
5.3 The Hawking-Moss Instanton . . . 83
5.4 Higher dimensions . . . 87
5.5 Four dimensions . . . 90
5.5.1 Bubble nucleated vacuum transitions . . . 91
5.5.2 Hawking-Moss Tunnelling . . . 94
5.6 Summary . . . 95

6 Scattering by dirty black holes 96
6.1 Introduction . . . 96
6.2 Dirty Black Hole spacetime . . . 98
6.3 Geodesic motion on a dirty black hole spacetime . . . 101
6.3.1 Deflection angle and classical scattering . . . 103
6.3.2 Critical effects in DBH spacetimes . . . 107
6.4 Waves on a dirty black hole spacetime . . . 110
6.5 Resonances of the dirty black holes . . . 111

6.5.1 Quasinormal modes and Regge poles 111
6.5.2 Numerical method 112
6.5.3 Results: The Regge pole spectrum 114
6.5.4 The WKB approximation 122
6.6 Wave Scattering by a dirty black hole 126
6.6.1 The differential scattering cross section: Partial waves expansion . 126
6.6.2 CAM representation of the scattering amplitude 126
6.6.3 Computational methods 128
6.6.4 Numerical Results and comments: Scattering cross sections . . . 129
6.7 Summary 133

7 Conclusion and outlook **135**
7.1 Black hole catalysed vacuum decay 135
7.1.1 Vacuum metastability with primordial black holes 135
7.1.2 Seeded vacuum decay with Gauss-Bonnet 136
7.1.3 The controversy on black hole seeded false vacuum decay 137
7.2 Scattering of dirty black holes 139
7.3 Future work 140

References **142**

Appendix A WKB approximation **157**

Appendix B Conical deficit **160**

List of figures

3.1 A sketch of quantum tunnelling with potential $U(x)$. 35

3.2 A potential for a particle tunnelling from a local, classically stable minimum to the lower minimum separated by a barrier. 40

3.3 The potential $U(x)$ with two degenerate minima at $x_{\pm}$. 41

3.4 Left: The inverted double well potential $-U(x)$. Right: Instanton trajectories for the symmetric double well. 42

3.5 A potential barrier separates the local minimum, from a lower and broader minimum and its converted potential. 44

3.6 Illustration of the three stages of false vacuum decay. (a) Bubble nucleation: true vacuum bubbles fluctuate into existence in the false vacuum background. (b) Bubble expansion: Bubbles grow and expand within the false vacuum. (c) Bubble collision: Bubbles collide with each other, and the bubble wall coalesces. 47

3.7 Left: The potential of a scalar field. The local minimum of $U(\phi)$ is defined as the false vacuum at $\phi = \phi_+$, while the global minimum is a true vacuum at $\phi = \phi_-$. The black dot at p is a turning point. Right: The inverted potential $-U(\phi)$. 48

3.8 The schematic plot of a one-dimensional potential that has two different minima, with the higher (lower) representing false (true) vacuum, labelled as ϕ_{FV} and ϕ_{TV}, respectively. The top of the potential barrier is labelled as ϕ_{Top}. A particle initially at the local minimum can arrive at the global minimum by two mechanisms: (i) Bubble nucleation (red) - quantum tunnelling to true vacuum or (ii) HM transition (blue) - climbing to the top of the potential and then rolling down to the true vacuum. 56

4.1 Sketch of the temperature profile around PBHs throughout the evaporation process. 63

4.2 Evolution of $\Gamma_{\mathrm{FVD}}/\Gamma_{\mathrm{ev}}$ with the PBH mass, using the initial plateau temperature T_{plateau} (red curve). In the grey-shaded area, $M < M_\star$, and in the red-shaded area, the ratio is larger than unity. 66

4.3 Constraints on the primodal black hole energy fraction at formation, $\beta'_{\mathrm{PBH}} \equiv \gamma^{1/2}(g_\star(T_f)/106.75)^{-1/4}\beta_{\mathrm{PBH}}$. The orange(red)-shaded region corresponds to constraints derived with $T = T_{\mathrm{max}}$ (T_{plateau}). 69

5.1 The ratios of tunnelling components B/B_{HM} change with the seed black hole mass in 5D spacetime, M_F/M_N, for fixed values of $\ell_F = 5$, $\ell_T = 4.5$, and $\alpha = 0.2$ where the relative mass gap is $M_C \approx 0.06M_N$. The blue solid lines represent remnant black hole masses ranging from lower to higher as “$0.2M_N$, $0.4M_N$, $0.6M_N$, $0.8M_N$, M_N", respectively; while the black solid line represents a remnant critical mass M_{crit}. The vertical dashed lines indicate the lower and upper bounds of the seed black hole mass. The red curve corresponds to the cosmological equal area limit. The cyan line represents a transition to a final de Sitter state without a remnant black hole, while the dots on the left axis show the transitions from pure de Sitter to remnant masses. The dashed lines on the left part of the graph, and the inset, represent a seed mass below the mass gap. 86

5.2 The ratios of tunnelling exponents B/B_{HM} as a function of seed mass in 6D spacetime, M_F/M_N, shown for parameter values $\ell_F = 5, \ell_T = 4.5$ and $\alpha = 0.2$. The dashed vertical line marks the Nariai limit for the seed mass. Blue solid lines represent different remnant black hole masses, ranging from $0.1M_N$ to $0.7M_N$ with steps of $0.1M_N$ from lower to higher. The red curve gives the equal horizon area constraint. The cyan line represents a transition from a seed black hole to pure de Sitter spacetime. The dots represent a transition from pure de Sitter spacetime to a spacetime with a remnant black hole. 88

5.3 The shift in entropy of the critical instanton in 5D as a function of $\tilde{\alpha}/\ell^2$ for the given bubble wall tensions indicated, $\bar{\sigma} = 0.1, 0.125, 0.15, 0.175$, respectively. 91

5.4 The shift in entropy of the critical instanton in 6D as a function of $\tilde{\alpha}/\ell^2$ for the given bubble wall tensions indicated, $\bar{\sigma} = 0.1, 0.125, 0.15, 0.175$, respectively. 91

6.1 Schematic diagram of a black hole surrounded by a thin shell (the thickness of the shell is ignored) located at $r = R_s$. 100

6.2 Illustration of the geodesic potential for the two configurations of DBH studied later on with $M = 1.5M_{\rm BH}$ and $R_S = 4M_{\rm BH}$ (blue curve) or $R_S = 5M_{\rm BH}$ (red curve). In the latter case, the shell is located outside of the outer light-ring (OLR) and therefore only exhibits a single light-ring structure. The former has the shell between the OLR and inner light-ring (ILR) and exhibits the two light-rings structure. (Features of the potential have been exaggerated to better illustrate the structure.) 103

6.3 Illustration of the various critical effects in a dirty black hole spacetime. Here we have chosen the configuration where the shell lies outside the light-ring of the exterior geometry, i.e., $R_S = 5M_{\rm BH}$ and $M_\infty = 1.5M_{\rm BH}$. In all pictures, the black disc represents the inner black hole with mass $M_{\rm BH}$, the dashed green circle represents the location of the shell at $r = R_S$ and the dashed black circle depicts the inner light-ring at $r = 3M_{\rm BH}$. a) The picture depicts glory scattering. In this case, the defection angle function $\Theta(b)$ passes smoothly through π, i.e., geodesics are scattered in the backward direction. b) The picture illustrates rainbow scattering. In this case, a congruence of geodesics centred around the rainbow impact parameter $b = b_r$ is presented (solid red curves). The rainbow ray (black solid curve) defines an extremal angle, called the rainbow angle, beyond which rays cannot be deflected locally. c) The picture depicts the orbiting phenomenon. In this case, the deflection angle is divergent for a critical impact parameter $b = b_c$ and a particle orbits indefinitely at $r = 3M_{\rm BH}$ around the light-ring. d) The picture represents grazing rays. A congruence of rays centred around the grazing impact parameter $b = b_{R_s}$ is shown (solid red curves). The grazing ray (solid black curve) sets the boundary of the so-called edge region. 104

6.4 Deflection angle as a function of the impact parameter obtained from (6.13). Here we assume $M_\infty = 1.5M_{\rm BH}$, and the shell position $R_s = 4M_{\rm BH}$. The deflection angle diverges at both critical parameters $b_{\ell_-} = 3\sqrt{3}M_{\rm BH}/\sqrt{\alpha}$ and $b_{\ell_+} = 3\sqrt{3}M_\infty$ associated with a light-ring at $r_{\ell_-} = 3M_{\rm BH}$ and $r_{\ell_+} = 3M_\infty$ respectively. There is also a stationary point in the deflection angle, i.e. $\Theta'_{\rm geo}(b_r) = 0$, leading to the rainbow effect. 107

6.5 Deflection angle as a function of the impact parameter obtained from (6.13). Here we assume $M_\infty = 1.5M_{\rm BH}$, and the shell position $R_s = 5M_{\rm BH}$. The deflection angle diverges at a critical parameter $b_{\ell_-} = 3\sqrt{3}M_{\rm BH}/\sqrt{\alpha}$ associated with a light-ring at $r_{\ell_-} = 3M_{\rm BH}$. There is also a stationary point in the deflection angle, i.e. $\Theta^{'}_{\rm geo}(b_r) = 0$, leading to the rainbow effect. A local maximum occurring at $b = b_{R_s} = \sqrt{R_S^3/(R_S - 2M_\infty)}$ is also present, leading to grazing. A congruence of geodesics in this specific DBH configuration is represented in Fig. 6.6. 108

6.6 Null geodesics scattered by a DBH. In this case, we assume $M_\infty = 1.5M_{\rm BH}$ and $R_s = 5M_{\rm BH}$ and the incident geodesics are equally spaced. The impact parameter varies between $0.95b_c < b < 1.35b_c$ with a fixed step size $\Delta b = 0.04b_c$. The red solid line is the rainbow ray and has an impact parameter ($b = b_r = 1.1677b_c$) and, we can see a high concentration of rays in this direction leading to the characteristic amplification of the rainbow effect. The olive curve represents the grazing ray. 109

6.7 The ($\ell = 1, n = 1, \ldots, 10$) quasinormal modes of the scalar field. We assume $2M_{\rm BH} = 1$. 115

6.8 The Regge poles $\lambda_n(\omega)$ for the scalar field in a DBH spacetime with parameters $M_\infty = 1.5M_{\rm BH}$, $R_S = 4M_{\rm BH}$ and for frequencies $2M_\infty\omega = 3$ (upper panel) and $2M_\infty\omega = 6$ (lower panel). (We take $2M_{\rm BH} = 1$ to produce these plots). In both panels, the blue circle and red square branches correspond to the outer and inner surface waves for the DBH spacetime while the black diamond branch is the one for an isolated black hole of mass $M_{\rm BH}$. 117

6.9 The Regge poles $\lambda_n(\omega)$ for the scalar field in the DBH spacetime with parameters $M_\infty = 1.5M_{\rm BH}$ and $R_s = 4M_{\rm BH}$ at frequencies $2M_\infty\omega = 16$ (upper panel) and $2M_\infty\omega = 32$ (lower panel). We assume $2M_{\rm BH} = 1$. In both panels, the blue circle and red square branches correspond to the outer and inner surface waves for the DBH spacetime while the black diamond branch is the one for an isolated black hole. The purple triangles in the lower panel depict the third branch of broad resonances. 118

6.10 The Regge poles $\lambda_n(\omega)$ for the scalar field in the DBH spacetime with parameters $M_\infty = 1.5M_{\rm BH}$ and $R_s = 5M_{\rm BH}$ at frequencies $2M_\infty\omega = 16$ (upper panel) and $2M_\infty\omega = 32$ (lower panel). We assume $2M_{\rm BH} = 1$. In both panels, the blue circle and red square branches correspond to the outer (creeping modes) and inner surface waves for the DBH spacetime while the black diamond branch is the one for an isolated black hole. The purple triangles depict the third branch of broad resonances. As the frequency increases the surface wave branches move away and more broad resonances appear in between them. 119

6.11 Illustration of the connection formula (6.48) obtained by combining the propagating, tunnelling and connection matrix to relate the WKB modal coefficient across the turning points and the shell. The oscillating (growing/decaying) lines represent the propagation of WKB modes with real (imaginary) momenta p. 125

6.12 The scalar cross section of DBH for $2M_\infty\omega = 6$, $R_s = 4M_{\rm BH}$ and $M_\infty = 1.5M_{\rm BH}$ and its Regge pole approximation. The plots show the effect of including successively more Regge poles. 129

6.13 The scalar cross section of DBH for $2M_\infty\omega = 16$, $R_s = 4M_{\rm BH}$ and $M_\infty = 1.5M_{\rm BH}$ and its Regge pole approximation. The plots show the effect of including successively more Regge poles. 130

6.14 The scalar cross section of DBH for $2M_\infty\omega = 16$, $R_s = 5M_{\rm BH}$ and $M_\infty = 1.5M_{\rm BH}$ and its Regge pole approximation. The plots show the effect of including successively more Regge poles. 130

6.15 The scalar cross section of DBH for $2M_{\infty}\omega = 16$, and $M_{\infty} = 1.5M_{\text{BH}}$. a) We compare $R_s = 5M_{\text{BH}}$ to $R_s = 4M_{\text{BH}}$. We can see that the scattering amplitude is enhanced by the rainbow effect for $R_s = 5M_{\text{BH}}$ at the rainbow angle $\theta_r \approx 157.8°$ (blue dotdashed line). b) We compare $R_s = 5M_{\text{BH}}$ to $R_s = 5.7M_{\text{BH}}$. We can see that the scattering amplitude is enhanced at $\theta_r \approx 115.3°$ (red line) for $R_s = 5M_{\text{BH}}$ and at $\theta_r \approx 157.8°$ (blue dotdashed line). 131

6.16 The scalar cross section of DBH for $2M_{\infty}\omega = 16$, and $M_{\infty} = 1.5M_{\text{BH}}$. a) We compare $R_s = 5M_{\text{BH}}$ to $R_s = 4M_{\text{BH}}$. We can see that the scattering amplitude is enhanced by the rainbow effect for $R_s = 5M_{\text{BH}}$ at the rainbow angle $\theta_r \approx 157.8°$ (blue dotdashed line). b) We compare $R_s = 5M_{\text{BH}}$ to $R_s = 5.7M_{\text{BH}}$. We can see that the scattering amplitude is enhanced at $\theta_r \approx 115.3°$ (red line) for $R_s = 5M_{\text{BH}}$ and at $\theta_r \approx 157.8°$ (blue dotdashed line). 132

A.1 Classical region of a particle is moving in a one dimension potential with $E > U(x)$. 158

A.2 Scattering from a rectangular barrier with a bumpy top 159

List of tables

6.1 A sample of the first quasinormal frequencies $\omega_{\ell n}$ of the scalar field. The radius of the thin shell is $R_s = 2.52M_{\mathrm{BH}}$ and the ADM mass is $M_\infty = 1.02M_{BH}$. We assume $2M_{\mathrm{BH}} = 1/2$. 116

6.2 The lowest Regge poles $\lambda_n(\omega)$ for the scalar field. The radius of the thin shell is $R_s = 4M_{BH}$ and the ADM mass is $M_\infty = 1.5M_{BH}$. 120

6.3 The lowest Regge poles $\lambda_n(\omega)$ for the scalar field. The radius of the thin shell is $R_s = 5M_{BH}$ and the ADM mass is $M_\infty = 1.5M_{BH}$. 121

Nomenclature

Acronyms / Abbreviations

BBN	Big Bang Nucleosynthesis
BHHM	Black-Hole-Hawking-Moss
CDL	Coleman de-Luccia
CMB	Cosmic Microwave Background (CMB)
CMS	The Compact Muon Solenoid
DBH	Dirty Black Hole
dS	de Sitter
EGB	Einstein Gauss-Bonnet
EHT	Event Horizon Telescope
FOPT	First-Order Phase Transition
FVD	False Vacuum Decay
GB	Gauss-Bonnet
HM	Hawking Moss
PBH	Primordial Black Hole
QFT	Quantum Field Theory

QNM	Quasinormal Mode
BAO	Baryon Acoustic Oscillations
CAM	Complex Angular Momentum
CMB	Cosmic Microwave Background
LSS	Large-scale Structure
RP	Regge Pole
SM	Standard Model
WKB	Wentzel-Kramers-Brillouin

Chapter 1

Introduction

General Relativity (GR) and Quantum Field Theory (QFT) are the two most successful and well-established theories in physics. GR describes gravity and the structure of spacetime on large scales, while QFT, primarily applied in the realm of microphysics, explains elementary particles as quantized excitations of underlying fields. Despite both theories being experimentally verified to incredible precision, there are problems in each theory that need to be carefully treated. It seems inevitable that spacetime singularities will form via the description of classical GR, leading to a breakdown of infinite curvature. A major issue in QFT is that one always encounters infinities in calculations; although renormalization techniques can resolve some of these problems, they do not apply universally, which endangers the consistency and completeness of QFT. Hence, the call for a consistent and comprehensive theory that can address these existing problems is imminent.

The necessity of a deeper theory of quantum gravity also hides in the study of black hole physics. Black holes have gained significant attention due to their fascinating properties and simplicity since being predicted by GR. However, the blossoming of black hole physics only came around with the establishment of black hole thermodynamics in the 1970s. Bekenstein [1] and Hawking [2] showed that black holes can radiate energy, with their temperature and entropy[1]

$$T_H = \frac{\kappa}{2\pi}, \quad S_{BH} = \frac{A}{4G} \tag{1.1}$$

---

[1] We use natural units of $\hbar = c = 1$, and the reduced Planck mass $M_p^2 = 1/8\pi G$.

are proportional to the surface gravity κ and the area of the event horizon. Hawking made the first attempt to incorporate quantum mechanical effects with classical black holes, which led to Hawking radiation [2]. This description predicted black hole evaporation due to the emission of thermal radiation with the same spectrum as a black body. A natural suspicion from this is that quantum information encoded with the initial stages of black holes may be destroyed, which yields the *information paradox* (see [3] for a review).

Over the past fifty years, many proposals and models have been suggested, with black holes considered a good candidate for studying the microscopic structure of spacetime. However, there is still a lack of consensus. Recent developments have shown that the direct quantisation of GR is difficult. One is, therefore, motivated to seek alternatives which facilitate more feasible constructions of a quantum theory of gravity.

One approach we can take is to consider the quantum effects in the presence of gravity. This thesis focuses on the specific topic of false vacuum decay in the presence of gravity and explores how the scenario is affected by the existence of black holes. False vacuum decay involves the study of a system that is classically stable but becomes metastable due to quantum fluctuations. One of the mysteries at the core of the conflict between gravity and particle physics is the nature of the vacuum. Assumptions about the vacuum underlie Hawking radiation and inflation. But how do we define the vacuum? The simplest way is to say it is the state of "lowest energy". However, this presupposes that there is a lower bound and that we live in it! Measurement of Standard Model (SM) parameters, particularly the Higgs and top quark masses, reveal the possibility of lower vacuum energy in the effective potential of the SM Higgs field at high Higgs values [4–9]. This suggests that our universe may be in a metastable vacuum that can undergo a phase transition from our local minimum to a global minimum, which is the decay channel of interest. In a sequence of papers by Coleman and collaborators [10, 11], they described the process of a bubble of true vacuum nucleating in the ambient false vacuum, named bubble nucleation (the presence of gravity can be found in [12]). This bubble nucleation is usually triggered by impurities in our early Universe, with the simplest impurity being a black hole. Part of this thesis will focus on vacuum decay seeded by black holes.

Another focus of this thesis relates to the scattering of black holes with matter in their vicinity. In recent years, we have developed observational techniques for testing strong-field regions at the horizon scale of black holes. There are two main results that show direct evidence of black holes: The first images of black holes by Event Horizon Telescope [13], and the first gravitational wave detection by LIGO/Virgo collaboration [14]. Governed by observational signatures of black holes, it is particularly interesting to study black hole dynamics by analysing ambient test fields. Therefore, we investigate the scattering and absorption of black holes. The physics of particle scattering from various types of black holes has been one of the most active topics of strong gravitational fields over the past few decades.

A black hole spacetime exhibits similar scattering phenomena of geometric optics, such as glory, orbiting and rainbow, that happen in nature. These characteristic scattering phenomena are associated with specific features of the deflection function. Ford and Wheeler showed the connection between the classical deflection function and the quantum-mechanical scattering amplitude through a semiclassical analysis in [15]. The study of black hole scattering also provides a good tool for examining the tension between gravity and quantum effects.

Recent measurements have placed black holes in a more realistic realm, showing that black holes live in our matter-filled, inhomogeneous Universe. Therefore, we study this topic by considering black holes not only as isolated objects but also within their environment. We employ a toy model of plane monochromatic scalar waves impinging upon a Schwarzschild dirty black hole - a Schwarzschild black hole surrounded by a spherical thin shell.

The thesis is organized as follows: Chapters 1 and 2 give the general overview of the key background to the presented work. In Chapter 2, we review the mathematical and physical concepts of black holes, tracing their evolution from theoretical origins to contemporary observational discoveries. Particularly, this chapter places emphasis on black holes in modified gravity and introduces the definition of “dirty black holes” to build the background for our research work.

In Chapter 3, we briefly review the basic philosophy of instantons as a prelude to Chapters 4 and 5. We start with quantum tunnelling in one-dimensional quantum mechanics. A new method of calculating the tunnelling rate – Euclidean path integral – brought out the knowledge of the instantons and bounces. We then extend these studies to quantum field theory, where tunnelling from a local minimum to the global minimum of the potential is referred to as *false vacuum decay* in the literature. Subsequently, we present the standard Coleman de Luccia bubbles in curved spacetime and compute the decay rate. The main goal of this chapter is to lay the groundwork for further research on the catalysis of vacuum decay by black holes.

In Chapter 4, we apply the seeded false vacuum decay to light primordial black holes, which is hard to observe by modern experimental data, as they have, in principle, evaporated due to their strong Hawking radiation. We compare the decay rate with Hawking evaporation rate, and check if the seeded decay happens before the black hole has totally evaporated. We then add constraints to primordial black hole abundance based on our results.

In Chapter 5, we investigate false vacuum decay catalysed by black holes under the influence of the higher order Gauss-Bonnet term. We study both bubble nucleation and Hawking-Moss types of phase transition in arbitrary dimensions. The equations of motion of “bounce” solutions in which bubbles nucleate around arbitrary dimensional black holes are found in the thin wall approximation, and the instanton action is computed.

In Chapter 6, we study the problem of plane monochromatic scalar waves impinging upon a Schwarzschild dirty black hole. We show that dirty black hole spacetimes may exhibit various critical effects for geometrical optics via a null geodesic description. We then compute the Regge pole spectrum for various dirty black hole configurations and show that it exhibits two or three distinct branches of poles. Also, we provide the complex angular momentum representation of the differential scattering cross section and examine the role of the different Regge pole branches.

We conclude the main research results of the presented work in Chapter 7 and outline future research interests.

Lastly, detailed calculations of the methodologies that we omitted throughout the text are included in Appendices A and B, as supplementary materials to the thesis.

Chapter 2

Black holes

The work in this thesis is based on studies of different aspects of black holes. The first part will show how light black holes can act as nucleation sites to seed false vacuum decay (a quantum tunnelling process in quantum field theory) and investigate how the higher curvature terms vary the tunnelling rate. In the second part, the scattering problem involving black holes is visited. Hence, prior to diving into the actual research, we will provide a brief overview of black holes, including their origins and modern developments.

2.1 History of Black holes

Black holes are regions with massive amounts of matter stored in a tiny volume in spacetime. This concentrated mass creates strong gravity that overwhelms all other forces and leads to everything being absorbed - even light cannot escape. The special properties of black holes make them the best candidates to probe the nature of gravity mathematically and experimentally.

Studies of black holes have provided among the most intriguing problems in physics since their special features were proven. The first clue dates back to 1783, John Michell, a British scientist, who did the first rigorous calculations of the size of a ‘dark star’ in terms of the mass of the sun. The theoretical basis of black holes was established with the birth of GR by Albert Einstein in 1915. In his theory, gravity is shown to be simply described by an elegant mathematical structure – the differential geometry of the curved spacetime. The mathematical definitions of black holes are given by the solutions of Einstein's equation, which connects the change of curvature to the presence of matter and energy in spacetime:

$$G_{\mu\nu} \equiv R_{\mu\nu} - \frac{1}{2} R g_{\mu\nu} = 8\pi G T_{\mu\nu} \tag{2.1}$$

The Einstein tensor, $G_{\mu\nu}$, is a specific divergence free combination of the Ricci tensor $R_{\mu\nu}$ and the geometrical metric $g_{\mu\nu}$ ($R = g^{\mu\nu}R_{\mu\nu}$). On the right-hand side, $T_{\mu\nu}$ is the energy-momentum tensor,where G is the Newtonian constant of gravitation.

A spherically symmetric vacuum solution to Einstein's equation was derived by Karl Schwarschild in 1916. Since we are in vacuo, taking $T_{\mu\nu} = 0$ in (2.1), then we get the simplest solution, which is described by a Schwarzschild metric:

$$ds^2 = -\left(1 - \frac{2GM}{r}\right) dt^2 + \left(1 - \frac{2GM}{r}\right)^{-1} dr^2 + r^2 d\Omega^2 \tag{2.2}$$

It can be used for any spherically symmetric vacuum solution to (2.1). M functions as the conventional "mass" of the black hole. Soon after, the Reissner-Nordström black hole was found when the Maxwell field entered the energy-momentum tensor in (2.1). The first stationary and axisymmetric solution parameterized by mass and angular momentum was discovered by Roy Patrick Kerr around 50 years later, in 1963, which is a generalisation of Schwarzschild. The two sets of solutions established the mathematical principles of black holes. The study of black holes in nature is then a study of these mathematical solutions that reveal fascinating physical phenomena.

It is worth mentioning that early physicists called these compact objects 'dark stars' or 'collapsed stars'. Even though mathematical solutions were discovered in the early twentieth century, they remained a mathematical curiosity until the 1960s, when their full mathematical structure was understood and John Wheeler coined the term 'Black Holes' that we know nowadays.

Later on, the development of quantum mechanics introduced new categories for investigating black holes. Until 1974, black holes were considered completely black objects that absorbed everything. However, this would conflict with classical thermodynamics because potentially a black hole could swallow entropy. The discovery that black holes can radiate as black bodies has significantly changed our understanding. Black holes are now considered thermodynamic objects; Bekenstein proposed that the entropy of black holes is proportional to the surface area of its event horizon [1]. Stephen Hawking showed that a black hole can evaporate in the context of quantum field theory, with virtual particles jumping into existence and annihilating each other all the time. When this process occurs around the event horizon, one of the paired particles and anti-particles can be captured by gravity and fall into black holes while the other escapes to infinity. Hence, black holes behave like a radiating black body, known as Hawking radiation[16]. The temperature of the black hole is shown to be proportional to its surface gravity. Since then, studies of black holes have entered a new era of being not only classical objects but also having quantum mechanical characteristics.

2.2 Modern evidence of black holes

Even though the astrophysical existence of black holes had been predicted for over 100 years, the physical and mathematical studies of black holes had been popular for only half of a century. Seeing a black hole directly is still impossible as it absorbs everything, even light. However, there are some theoretical principles that favour finding hints of the presence of black holes. We list three different detection methods that have only recently borne fruit after many years of effort.

- *Stellar motions:* Tracking objects circulating around black holes. The strong gravitational pull from black holes affects the movements of nearby objects. Visible objects orbit around or move towards a dark area. The exact properties, like how heavy the black hole is, can be analysed through analysis of the trajectories.

- *Gravitational Waves:* Hearing the “sound” of black hole mergers. The inspiral and merger of a binary black hole and the ringdown of the resulting single black hole create spacetime ripples, known as gravitational waves. The waveform predicted by GR provides the basis for detecting gravitational wave signals at a certain frequency. The detected waveform matches the predictions of the GR for the inspiral and merger of a pair of black holes and the ringdown of the resulting single black hole.

- *Black Hole Shadow:* Looking at the interstellar gas or dust falling into black holes. Matter that drifts around black holes will accelerate at a very high speed and become extremely hot when it approaches a black hole. The glowing brightness can be seen as a ring with a dark area in the centre, which is a black hole shadow. The captured light bent by the strong gravity is massive and favours experimental observations.

Based on these theories and predictions in GR, the existence of the black hole was proved experimentally after nearly a century of studying and searching. The measurement of stellar velocities in the innermost regions of the Milky Way revealed the existence of a supermassive black hole in the centre of our galaxy [17]. The announcement of the direct detection of gravitational waves from the steller-mass black holes merger by the LIGO-Virgo collaborations [14] unveils the first mystery of the experimental proof of black holes. They have announced nearly around 100 detections of gravitational wave signals since then. Following the signals that we hear from the black hole mergers, the first image of a supermassive black hole candidate in the centre of the giant elliptical galaxy M87 was released in 2019 by EHT [13]. The observed image is consistent with expectations for the shadow of a Kerr black hole as predicted by GR. In 2022, the EHT collaboration presented the first direct visual evidence of Sagittarius A*, the black hole at the centre of the Milky Way galaxy [18].

Another convincing evidence from astronomical and cosmological observations is that $\approx 85\%$ of the matter that exists in our Universe is non-baryonic dark matter. One possibility is that the dark matter might instead consist of black holes that were formed before the epoch of Big Bang nucleosynthesis and with masses below the sensitivity range of microlensing surveys.

2.3 Primordial black holes

Stellar mass and supermassive stars collapse to form black holes when their gravitational pull dominates over other forces, however this does not account for all populations of observed black holes. There is a particular interest in primordial black holes (PBHs) which formed in hot and dense regions of the early Universe. Although PBHs have not been experimentally confirmed, studies of PBHs have been seriously considered in recent years for multiple reasons.

The existence of PBHs is a natural result of many inflationary models [19–21] and can help to remove the undesirable defects that existed in the early Universe [22, 23]. The mass of PBHs can vary greatly depending on the time of formation, such that the Hawking radiation is significant if the mass of PBH is sufficiently small. More importantly, PBHs are popular for their ability to constitute part or even all of the dark matter [24–26]. The coalescence events observed by the LIGO-Virgo collaboration [27–30] can be explained by PBHs. Hence, the study of PBHs is crucial in further understanding the early Universe.

The mass and abundance of PBHs depend on the formation mechanisms and are closely related to the underlying inflationary scenario and model. The main origin of PBHs is the gravitational collapse of large curvature perturbations generated during inflation [31, 32]. The collapse of topological defects in the early Universe [33], the dynamics of scalar condensates [34, 35] and collisions of bubble walls during a first-order phase transition [36] are viable alternatives.

Many constraints on the PBH abundance have been discussed over the past decades for different masses (see [25] for a review). However, most of the constraints are subject to underlying assumptions that account for different results. This constraint will be significantly weakened or even removed entirely if we remove those assumptions. Here in this thesis, we focus on black hole evaporation in a certain mass range. The evaporation time is related to its mass via Hawking radiation, $t_{eva} \approx M_{BH}^3$. In principle, all black holes that are lighter than $4.5 \times 10^{14} g$ have evaporated by now. Therefore, it is hard to add constraints from cosmological models or even observations. However, in later chapters, we will discuss how the PBH abundance changes if the false vacuum decay seeded by a black hole is accomplished before it evaporates completely. We add constraints to PBHs in the energy fraction $\beta > 7 \times 10^{-80} (M/\mathrm{g})^{3/2}$ based on our results. The details will be shown in Chapter 4.

2.4 Other aspects of black holes

2.4.1 Black hole solution in modified gravity

General Relativity, together with quantum field theory, stands as a remarkable and revolutionary theory that has unravelled numerous mysteries of the universe. However, the rapid progress in observational telescopes has enabled the testing of fundamental physics on a cosmic scale. The foundations of GR remain unchanged over a century but fail to explain the present accumulation of astrophysical and cosmological data with its ordinary baryon matter. GR encounters a significant challenge in explaining the invisible substance – the so-called "Dark Sector" of the Universe. *Dark energy* is considered to drive the accelerating expansion of the Universe, and *dark matter* was introduced to explain the stable dynamics of galaxies and galaxy clusters. Cosmologists have determined the composition of the universe is 4.9% ordinary matter, 26.8% dark matter and 68.3% dark energy based on a combination of evidence from cosmological data, such as Supernova, Baryon Acoustic Oscillations (BAO), Cosmic Microwave Background (CMB) and Large-scale Structure (LSS). Such recent observations inspire investigations beyond Einstein's theory for suitable alternatives to describe the universe at large scales.

There is a vast range of different ways to modify gravity. For example, adding extra scalar, vector or tensor fields in the gravitational sector [37–40] and introducing extra spatial dimensions to go beyond the standard four-dimensional spacetime [41–45], or replacing the Ricci scalar R with a more general function $F(R)$ in the Einstein-Hilbert action [46, 47] (refer to [48] for a thorough review of modified gravity). All of those modifications are based on the general validity of Einstein equation. Solutions to the modified Einstein equations can give rise to different black hole solutions that will exhibit various properties.

Among the alternatives to GR, higher curvature theories have a uniquely privileged position as they require no extra fundamental fields and can be motivated within a quantum gravity setting. While adding an arbitrary higher derivative term to the gravitational action can result in quartic (or higher) time derivatives, introducing additional degrees of freedom that can lead to ghost instability. The Gauss-Bonnet (GB) term (the lowest order Lovelock contribution [44, 45]) is quadratic in curvature while retaining only second-order field equations. As such, we will study the Einstein Gauss-Bonnet (EGB) gravity as a particular interest to test how these higher curvature terms alter gravitational phenomenology in Chapter 5.

2.4.2 Dirty black hole

Another aspect of black holes is that all black holes are not isolated objects in the Universe. Exploration of black holes can not exclude exotic environments – surrounded by accelerating materials and generating intense radiation. The matter fields around black holes will significantly change observational results from nowadays telescopes. The radiation we receive might not only come from black holes but also originate from the surrounding accelerating disks. Surrounding matter spirals into black holes when its angular momentum reduces due to the dissipation. The gravitational energy converted into heat will eventually leak in the form of radiation, which escapes the disks and follows its geodesics of curved paths to reach our telescopes [49].

The picture from the shadow of the M87 supermassive black hole from the EHT [13] provided the first direct observation of a black hole shadow. By providing the first direct time and spatial signals from black holes, these measurements have taken black holes from a purely theoretical realm into concrete physical objects in our matter-filled, inhomogeneous Universe. This breakthrough highlights the importance of studying black holes not only as isolated objects but also within their environment.

This is by no means a new consideration and there is extensive literature on the study of black holes embedded into rich and varied environments (see for example the review articles [50, 51], motivated by the detection of gravitational waves). A particular emphasis was put on the impact of dark matter surrounding black holes and their imprint of gravitational waveforms [52–54], (however see also, e.g., [55–57] for studies of the interaction of black holes with dark energy). In this thesis, we consider the particular case of what is referred to in the literature as a *dirty black hole* (DBH), that is, a black hole surrounded by a thin-shell of matter. DBHs were introduced as practical toy models to investigate the impact of a local environment on black hole effects [58–60]. We will show more about the scattering of the DBH in Chapter 6.

Chapter 3

Quantum tunnelling

Tunnelling is a fundamental phenomenon in quantum theory for which particles or fields can transit under a barrier that is otherwise forbidden classically. In quantum field theory, it occurs especially for a scalar field having multiple potential minimums, leading to a transition from one higher potential minimum to a lower one, usually dobbed as false vacuum decay (FVD). This phenomenon gives rise to a first-order phase transition (FOPT) through the nucleation of a new phase (true vacuum) in an old phase (false vacuum). The theoretical description of FVD has been developed by Coleman and collaborators in a sequence of papers [10, 11] based on the path integral formulation of quantum theory. Their method relies on instantons which are regular solutions of the Euclidean field equations of motion. For false vacuum decay, the particular instanton is called bounce, which will be discussed in more detail below.

FVD has far-reaching consequences in both cosmology and particle physics. For the latter, the recent measurements of the Higgs mass and the top quark mass indicate the existence of an additional potential minimum of the Higgs field lower than the electroweak vacuum [4–9]. This suggests that our universe could be in a metastable vacuum that can decay into the true vacuum corresponding to the lower Higgs potential minimum. Theoretical consistency requires that the lifetime of the electroweak vacuum must be longer than the age of the Universe, giving constraints of beyond the Standard Model physics.

Before we move to the technical aspects of FVD, we first review quantum tunnelling in quantum mechanics focusing on the description based on path integrals. There, the concepts of instantons and bounces will be introduced. Then we will generalise this description to quantum field theory. Finally, we extend it to curved spacetime and discuss the impact of gravity on false vacuum decay rates.

3.1 Tunnelling in quantum mechanics

Quantum tunnelling occurs when a particle has a lower energy than a potential barrier. Consider a particle moving along the x axis with a potential as shown in Fig. 3.1. Assuming that the particle has an energy $E < U_0$, then the particle is not allowed to enter the region $0 < x < a$ classically. Hence, if the particle is initially located at the left side of the potential barrier, it can never reach the right side.

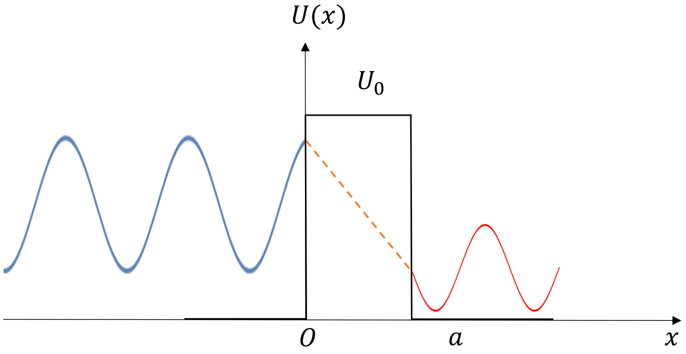

Fig. 3.1 A sketch of quantum tunnelling with potential $U(x)$.

In quantum mechanics, there is a non-zero probability for a particle to transmit over/through the potential barrier, known as quantum tunnelling. All the information of the particle is encoded in its wave function, which is governed by the Schrödinger equation

$$-\frac{\hbar^2}{2m}\frac{d^2\psi}{dx^2} + U(x)\psi = E\psi. \tag{3.1}$$

The kinetic term can be rewritten as

$$-\frac{d^2\psi}{dx^2} = \frac{2m}{\hbar^2}[E - U(x)]\psi \tag{3.2}$$

The probability of the particle tunnelling through the barrier is determined by the ratio of the transmitted coefficients to the incident coefficients, which can be solved by applying appropriate boundary conditions. The transmission rate can be calculated by using the Wentzel-Kramers-Brillouin (WKB) approximation (details can be found in Appendix A), which obeys

$$\Gamma \approx \frac{1}{\hbar}\exp\left(-\int_0^a k\,dx\right) \tag{3.3}$$

with $k = \sqrt{2m(U_0 - E)}$ and a is the width of the potential well. The probability of a particle tunnelling through the barrier is dominated by the exponential factor, which represents the strength of the barrier.

3.2 Instanton and bounce

3.2.1 Euclidean path integral

In this section, we will introduce a new method for calculating tunnelling probability via the Euclidean path integral. To this end, we consider a potential that will have a more direct application in quantum field theory, shown in Fig. 3.2. We will also assume the Lagrangian to be

$$\mathcal{L} = \frac{1}{2}\left(\frac{dx}{dt}\right)^2 - U(x), \tag{3.4}$$

which can be generalised to quantum field theory directly. Assume that a particle is initially trapped around the minimum x_+. This particle can still escape from the minimum x_+ to the lower one x_- via quantum tunnelling. This is reflected by the fact that the ground state energy of the particle at the minimum x_+ is actually complex [61], $E_0 = \mathrm{Re}E_0 + i\mathrm{Im}E_0$. Since the state evolves as $\psi(t) = \psi(t_i)e^{-iE_0 t} = \psi(t_i)e^{-i\mathrm{Re}E_0 t}e^{\mathrm{Im}E_0 t}$, one can see that the state can decay with the decay rate given by

$$\Gamma = -2\mathrm{Im}E_0. \tag{3.5}$$

The imaginary part of the ground state energy $\mathrm{Im}E_0$ can be conveniently computed via the Euclidean path integral. To see that, let us consider the following Euclidean transition amplitude

$$\langle x_+|e^{-HT/\hbar}|x_+\rangle \equiv Z = \int [dx] e^{-\frac{S[x]}{\hbar}}, \tag{3.6}$$

where H is the Hamiltonian and S is the Euclidean action. Above, $[dx]$ denotes the integral measure over all paths $x(\tau)$ with boundary conditions $x(-T/2) = x_+$ and $x(T/2) = x_+$. Inserting a complete set of energy eigenstates $|n\rangle$ into the transition amplitude, one obtains

$$\langle x_+|e^{-HT/\hbar}|x_+\rangle = \sum_n e^{-E_n T/\hbar} \langle x_+|n\rangle \langle n|x_+\rangle \tag{3.7}$$

In the limit of large T, (3.7) is dominated by the contribution of an eigenstate with the lowest energy E_0, i.e.,

$$\langle x_+|e^{-HT/\hbar}|x_+\rangle \cong e^{-E_0 T/\hbar} |\langle x_+|0\rangle|^2. \tag{3.8}$$

Therefore, the decay rate can be expressed as

$$\Gamma = \frac{2}{T}\,\mathrm{Im}\left(\ln Z - \ln|\langle x_+|0\rangle|^2\right) = \frac{2}{T}\,\mathrm{Im}\left(\ln Z\right), \tag{3.9}$$

where we have used the fact that the second logarithmic term is real.

More generally, one can consider Euclidean transition amplitudes with arbitrary boundary conditions

$$\langle x_f|e^{-HT/\hbar}|x_i\rangle = \sum_n e^{-E_n T/\hbar} \langle x_f|n\rangle\langle n|x_i\rangle. \tag{3.10}$$

The leading term for large T contains the information of the ground state energy and the corresponding wave function.

The classical Euclidean action S can be simply obtained by the Wick rotation, $t \rightarrow -i\tau$, and $iS_M \rightarrow -S$ (where S_M is the Minkowksian action),

$$S[x] = \int_{-\frac{T}{2}}^{\frac{T}{2}} d\tau \left[\frac{1}{2}m\dot{x}^2 + U(x)\right]. \tag{3.11}$$

Usually, the Euclidean path integral is computed with the method of steepest descent. In this method, one expands the integral around the stationary points, which are solutions to the classical equation of motion. Note that in the Euclidean action, the potential term has the opposite flipped sign compared with the Minkowskian one. Therefore, a classical Euclidean solution can be understood as a particle moving in the upside-down potential with appropriate boundary conditions set up by the transition amplitude under study. Let's consider a specific stationary point $\bar{x}$, satisfying

$$\left.\frac{\delta S[x]}{\delta x(\tau)}\right|_{x=\bar{x}} = -m\ddot{\bar{x}} + U'(\bar{x}) = 0. \tag{3.12}$$

Expanding about this stationary point, $x(\tau) = \bar{x}(\tau) + \delta x(\tau)$, one obtains

$$S[x(\tau)] = S[\bar{x}(\tau)] + \frac{1}{2}\int d\tau_1 \int d\tau_2 \left.\frac{\delta^2 S}{\delta x(\tau_1)\delta x(\tau_2)}\right|_{\bar{x}} \delta x(\tau_1)\delta x(\tau_2) + \ldots. \tag{3.13}$$

Note that the term linear in δx vanishes due to (3.12). The fluctuation operator can be read from (3.11),

$$\left.\frac{\delta^2 S}{\delta x(\tau_1)\delta x(\tau_2)}\right|_{\bar{x}} = \delta(\tau_1 - \tau_2)\left[-m\frac{d^2}{d\tau_2^2} + U''(\bar{x})\right]. \tag{3.14}$$

with $\delta(\tau_1 - \tau_2) = \delta x(\tau_1)/\delta x(\tau_2)$. The Dirac delta function would be eliminated by one of the integrals in (3.13). Then we have

$$S[x(\tau)] = S[\bar{x}(\tau)] + \frac{1}{2}\int d\tau\, \delta x(\tau)\left[-m\frac{d^2}{d\tau^2} + U''(\bar{x})\right]\delta x(\tau) + \ldots. \tag{3.15}$$

To perform the path integral, we may find a basis for the functional space. A convenient one is the basis $\{x_n(\tau)\}$ constituted by the eigenfunctions $x_n(\tau)$ of the fluctuation operator,

$$\left[-m\frac{d^2}{d\tau^2} + U''(\bar{x})\right] x_n(\tau) = \lambda_n x(\tau). \tag{3.16}$$

The eigenfunctions must satisfy the following orthonormal and boundary conditions

$$\int_{-\frac{T}{2}}^{\frac{T}{2}} d\tau\, x_n(\tau) x_m(\tau) = \delta_{nm}, \qquad x_n\left(\pm\frac{T}{2}\right) = 0. \tag{3.17}$$

On this basis, one can write

$$\delta x(\tau) = \sum_n c_n x_n(\tau) \tag{3.18}$$

and

$$[dx] = N \prod_n \frac{dc_n}{\sqrt{2\pi\hbar}}, \tag{3.19}$$

where N is a normalisation factor that should be chosen properly. The integral becomes a product of Gaussian integrals in the small-$\hbar$ limit, and we obtain

$$Ne^{-S(\bar{x})/\hbar} \prod_n \lambda_n^{-1/2}[1 + \mathcal{O}(\hbar)] = Ne^{-S[\bar{x}]/\hbar}[\det(-\partial_\tau^2 + U''(\bar{x}))]^{-1/2}[1 + \mathcal{O}(\hbar)]. \tag{3.20}$$

Below, we will omit writing the factor of $[1 + \mathcal{O}(\hbar)]$. In this formula, we naively assume all the eigenvalues are positive. However, for the case of tunnelling, there are both negative and zero eigenvalues, which must be dealt with with care, and will be discussed below.

Note that, (3.20) is only the contribution from the stationary point $\bar{x}$ under study to the whole path integral. If there are multiple stationary points, which is generally true, one must sum over all contributions from all the stationary points. Formally, one can write

$$Z = \sum_i Z_i \equiv \sum_i [\bar{x}_i] \tag{3.21}$$

with the subscript i labelling the stationary points. We have introduced a convenient notation $[\bar{x}]$ to denote the contribution to the full path integral from the stationary point $\bar{x}$. In our case, there is a trivial stationary point $\bar{x} = x_+$, whose contribution is

$$[x_+] = N[\det(-\partial_\tau^2 + U''(x_+))]^{-1/2}. \tag{3.22}$$

Actually, properly choosing the normalisation factor N, one can have [62]

$$[x_+] = \left(\frac{\omega}{\pi\hbar}\right)^{1/2} e^{-\frac{\omega T}{2}} \tag{3.23}$$

such that it gives the the ground state energy $E_0 = \frac{\hbar\omega}{2}$ and the wave function $\langle x_+|0\rangle^2 = (\omega/\pi\hbar)^{\frac{1}{2}}$ when x_+ is a stable minimum.

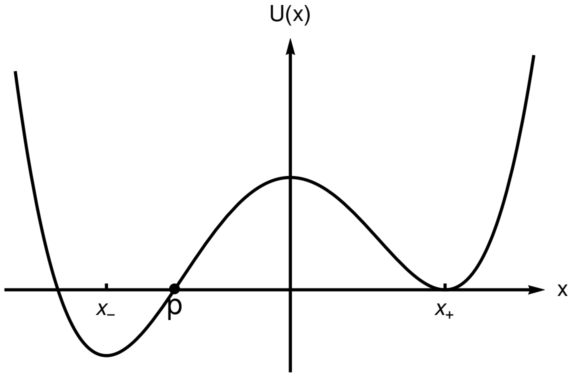

Fig. 3.2 A potential for a particle tunnelling from a local, classically stable minimum to the lower minimum separated by a barrier.

3.2.2 The double well and instantons

Above, we have shown the general idea of why the Euclidean path integral can be used for computing the energy of the ground state near a minimum, including the decay rate when this minimum is metastable. In this section, we apply the Euclidean method to the double-well potential and carry out a detailed calculation of the ground state energy. Through this, we will then introduce the concept of instantons.

The potential is shown in Fig. 3.3. We shall compute

$$\langle x_+|e^{-HT/\hbar}|x_+\rangle = \langle x_-|e^{-HT/\hbar}|x_-\rangle \tag{3.24}$$

and

$$\langle x_-|e^{-HT/\hbar}|x_+\rangle = \langle x_+|e^{-HT/\hbar}|x_-\rangle\,. \tag{3.25}$$

We shall compute these transition amplitudes using the Euclidean path integral and the method of steepest descent. The first step is to find the Euclidean classical solutions, with the boundary conditions consistent with the transition amplitudes.

It turns out that there are two elemental nontrivial classical solutions. All other solutions can be constructed from them. To find these elementary solutions, we consider a particle moving in the inverted potential, as shown in the left panel of Fig. 3.4. Then we can consider a particle initially located at x_- in the distant past, rolls down to the valley and

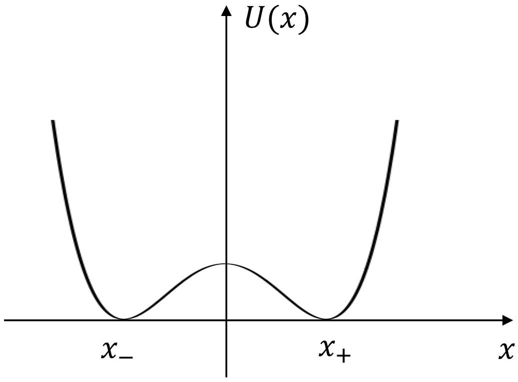

Fig. 3.3 The potential $U(x)$ with two degenerate minima at $x_\pm$.

reaches x_+ in the distant future. This solution can be found precisely and reads

$$\bar{x}_{\text{inst}}(\tau) = v \tanh(\omega(\tau - \tau_1)), \tag{3.26}$$

where $v = |x_\pm|$ (assuming the potential to be symmetric under $x \to -x$ for simplicity) and, $\omega^2 = U''(x_+)$. τ_1 is a free parameter characterising the time-translation invariance of the theory. The profile of this solution is shown on the right panel of Fig. 3.4. Such a solution is called an instanton, initially named by 't Hooft. The "On" implies that these kind of solutions are very similar to solitons; particle-like solutions in classical field theories. However, they are configurations in (Euclidean) time, thus the 'instant'. Note that, however, instanton solutions in quantum field theory are configurations on the four-dimensional Euclidean space, not only on time.

The contribution to the full path integral from the instanton is

$$[\bar{x}_{\text{inst}}] = e^{-S[\bar{x}_{\text{inst}}]/\hbar} \left[\det(-\partial_\tau^2 + U''(\bar{x}_{\text{inst}})) \right]^{-1/2}. \tag{3.27}$$

Now, there is actually one zero mode in the spectrum of the fluctuation operator $-\partial_\tau^2 + U''(\bar{x}_{\text{inst}}))$. The integral over the fluctuations in the zero-mode direction can be traded for the integral over the collective coordinate τ_0 of the instanton [63], inducing an additional factor of $\sqrt{S[\bar{x}_{\text{inst}}]/2\pi}$ for each zero mode [11]. Since for the present case we have only one zero mode, we therefore arrive at

$$[\bar{x}_{\text{inst}}] = \left(\int d\tau_1\right) e^{-S[\bar{x}_{\text{inst}}]/\hbar} \sqrt{\frac{S[\bar{x}_{\text{inst}}]}{2\pi\hbar}} \left[\det{}'(-\partial_\tau^2 + U''(\bar{x}_{\text{inst}}))\right]^{-1/2}. \tag{3.28}$$

where a prime on “det” means that the zero mode is subtracted when evaluating the functional determinant.

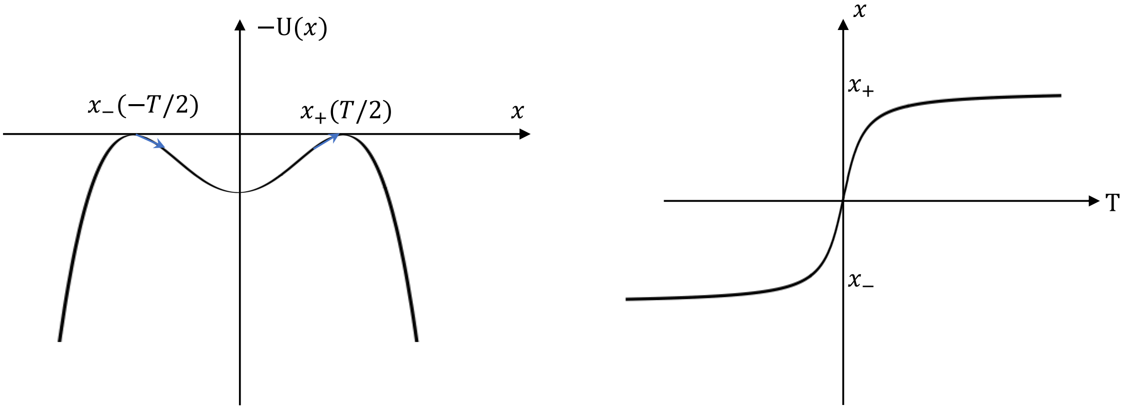

Fig. 3.4 Left: The inverted double well potential $-U(x)$. Right: Instanton trajectories for the symmetric double well.

The other elementary solution is just the time-reversed solution of instanton, called anti-instanton, which has the same action as the instanton. Actually, due to the symmetry, the functional determinants for instanton and anti-instanton are also equal to each other. Therefore, we have $[\bar{x}_{\text{inst}}] = [\bar{x}_{\text{anti-inst}}]$.

In the limit $T \to \infty$, a general solution is actually constituted by these two elementary solutions:

$$\bar{x}_n \approx v(-1)^n \tanh\omega(\tau-\tau_1)\tanh\omega(\tau-\tau_2)\ldots\tanh\omega(\tau-\tau_n), \tag{3.29}$$

and their “anti” ones, which differ by only a minus sign and will be denoted as $\bar{x}_{\bar{n}}$. The contribution from $\bar{x}_n$ to the full path integral can be computed using the so-called dilute instanton gas approximation. It gives [11]

$$\begin{aligned}[\bar{x}_n] &\approx \int_{-\frac{T}{2}}^{\frac{T}{2}} d\tau_1 \int_{\tau_1}^{\frac{T}{2}} d\tau_2 \cdots \int_{\tau_{n-1}}^{\frac{T}{2}} d\tau_n\, [\bar{x}_+] \left(\frac{[\bar{x}_{\text{inst}}]}{[x_+]}\right)^n \\ &= \left(\frac{\omega}{\pi\hbar}\right)^{1/2} e^{\frac{\omega T}{2}} \left(\frac{T^n}{n!} e^{-nS[\bar{x}_{\text{inst}}]/\hbar} K^n\right),\end{aligned} \tag{3.30}$$

where

$$K=\sqrt{\frac{S\left[\bar{x}_{\text{inst}}\right]}{2\pi\hbar}}\left(\frac{\det'(-\partial_\tau^2+U''(\bar{x}_{\text{inst}}))}{\det(-\partial_\tau^2+U''(\bar{x}_{+}))}\right)^{-1/2}. \tag{3.31}$$

From these, one can obtain

$$\begin{aligned}\langle x_-|e^{-HT/\hbar}|x_-\rangle &= \sum_{\text{even } n}[\bar{x}_n]=\left(\frac{\omega}{\pi\hbar}\right)^{1/2}e^{\frac{\omega T}{2}}\sum_{\text{even } n}\left(\frac{T^n}{n!}e^{-nS[\bar{x}_{\text{inst}}]/\hbar}K^n\right)\\ &=\left(\frac{\omega}{\pi\hbar}\right)^{1/2}e^{\frac{\omega T}{2}}\frac{1}{2}\left(e^{KTe^{-S[\bar{x}_{\text{inst}}]/\hbar}}+e^{-KTe^{-S[\bar{x}_{\text{inst}}]/\hbar}}\right)\end{aligned} \tag{3.32}$$

and

$$\begin{aligned}\langle x_-|e^{-HT/\hbar}|x_+\rangle &= \sum_{\text{odd } n}[\bar{x}_n]=\left(\frac{\omega}{\pi\hbar}\right)^{1/2}e^{\frac{\omega T}{2}}\sum_{\text{odd } n}\left(\frac{T^n}{n!}e^{-nS[\bar{x}_{\text{inst}}]/\hbar}K^n\right)\\ &=\left(\frac{\omega}{\pi\hbar}\right)^{1/2}e^{\frac{\omega T}{2}}\frac{1}{2}\left(e^{KTe^{-S[\bar{x}_{\text{inst}}]/\hbar}}-e^{-KTe^{-S[\bar{x}_{\text{inst}}]/\hbar}}\right).\end{aligned} \tag{3.33}$$

Comparing to (3.10), one can see that we have two lowest-lying states with energyes

$$E_\pm=\frac{1}{2}\hbar\omega\pm\hbar Ke^{-S[\bar{x}_{\text{inst}}]/\hbar}. \tag{3.34}$$

The wave functions $|\langle\pm|x_\pm\rangle|^2$ can also be read from the results in Eqs. (3.32) and (3.33).

The result in (3.34) is of course well known. The $\frac{1}{2}\hbar\omega$ is the ground state energy for a harmonic potential $U=\frac{1}{2}\omega^2(x-x_\pm)^2$, which approximates well the local potential near $x_\pm$. The full double well potential presents two degenerate minima and one would naively expect degenerate energies. However, quantum corrections break this degeneracy, causing the splitting of the energy spectrum. This energy splitting is essentially a tunnelling effect; a particle located in the left well can feel the existence of the right well via quantum tunnelling, and vice versa. The exponential function $\exp(-S[\bar{x}_{\text{inst}}])/\hbar$ manifests the WKB suppression of the tunnelling process. The new derivation based on the Euclidean path integral clearly shows that how instantons describe such tunnelling effects. And we see that the WKB suppression is simply given by the Eucldiean action of instantons.

3.2.3 Unstable states and bounces

We can now extend the study to the decay of unstable states with the knowledge of instantons. In this subsection, we focus on the so-called bounce solutions, which are relevant to the decay process of metastable states. An example of a potential barrier that connects two different minima is sketched in Fig. 3.5. The local minimum is considered unstable due to the existence of a lower minimum. In order to compute the decay rate via the Euclidean path integral, we turn the potential upside down (converted potential is shown in the right panel of Fig. 3.5). The 'bounce' is a solution in which a particle starts at the top of the potential at $x = 0$ at time minus infinity, then reaches the turning point p where another zero potential energy lives, and finally bounces back to the top of the hill at time plus infinity[1]. The computation for the matrix element between turning points is similar to the study of instanton in the context of a double-well potential. We choose x_i and x_f in (3.10) to be 0

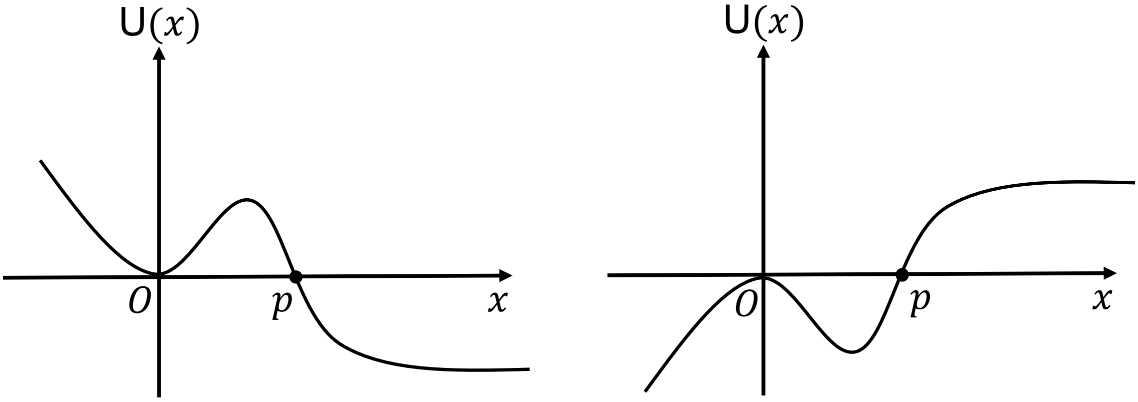

Fig. 3.5 A potential barrier separates the local minimum, from a lower and broader minimum and its converted potential.

$$Z(T) = \langle x_f | e^{-HT/\hbar} | x_i \rangle = \langle 0 | e^{-HT/\hbar} | 0 \rangle \tag{3.35}$$

We can proceed as before and evaluate the path integrals by summing the contributions from the stationary points and approximation stationary points of the action, including a constant solution $x_0(\tau) = 0$, bounce solutions $x_b(\tau)$, and all possible multibounce solutions,

---

[1] We focus on the results for very large T, so we limit ourselves to such motions with infinite T.

which centres at the point $dx/d\tau = 0$. If there are n bounces, with their centres located at $\tau_1, \tau_2, \ldots, \tau_n$, where $-T/2 < \tau_1 < \tau_2 < \cdots < \tau_n < T/2$. Taking the results from the last subsection, we have

$$\begin{aligned} Z &= \frac{N}{\sqrt{\mathrm{Det}\, S''[x_0]}} e^{-\frac{S[x_0]}{\hbar}} \sum_{n=0}^{\infty} \frac{K^n T^n}{n!} e^{\frac{-n(S[x_b]-S[x_0])}{\hbar}} \\ &= \frac{N}{\sqrt{\mathrm{Det}\, S''[x_0]}} e^{-\frac{S[x_0]}{\hbar}} \exp\left[K T e^{\frac{-n(S[x_b]-S[x_0])}{\hbar}} \right] \end{aligned} \tag{3.36}$$

The decay rate can be computed by substituting (3.36) into (3.9), with its imaginary part, is related to decay rate. Before proceeding, we must calculate K in (3.36).

The main difference in the computation when compared to instanton is that the bounce has zero velocity at $\tau = 0$, therefore, $dx_b/d\tau$ has a node, thus cannot be the eigenvector of $S''[x_b]$ with the smallest eigenvalue. This implies that $S''[x_b]$ has an eigenvector with a negative eigenvalue, which is problematic for the determinant. The presence of a negative eigenvalue means that x_b is not the minimum action among all possible paths but a saddle point. To provide a clearer explanation, recall that the bounce solution involves an integral over a path that starts from an initial point, reaches an equipotential surface where $U(x = 0) = U(x = p)$, and then returns to its original position. Negative modes arise from paths that do not return to the equipotential surface, which relate to undershooting or overshooting scenarios that are not stable. These negative modes correspond to alternative paths that are to the Euclidean action rather than the bounce action.

To keep things simple, we now turn to the integral over some path in function space parameterized by a real variable, z,

$$J = \frac{1}{\sqrt{2\pi\hbar}} \int_{-\infty}^{+\infty} dz\, e^{\frac{S(z)}{\hbar}} \tag{3.37}$$

where $S(z)$ is the action along the path. The integral is real and finite as long as the potential energy has an absolute minimum in $x = 0$. It diverges for the region where a lower minimum appears. To address the problem, following the steepest descent method, we deform the contour of integration along the real z axis, and this gives J a constant imaginary part

$$\text{Im}\, J = \text{Im}\frac{1}{\sqrt{2\pi\hbar}}\int_{p}^{p+i\infty} dz\, e^{-\frac{S(z)}{\hbar}} = \frac{1}{\sqrt{2\pi\hbar}}\int_{0}^{+\infty} dz\, e^{-\frac{S(p+iz)}{\hbar}} = \frac{1}{2}e^{-\frac{S(p)}{\hbar}}\frac{1}{\sqrt{|S''(p)|}} \tag{3.38}$$

with $S''(p) < 0$, where the constant $1/2$ arises from the integration of over half of the Gaussian peak. This contour deformation for the negative mode has been more clearly explained in [64, 65].

The value of K can be written as

$$K = \frac{i}{2}\sqrt{\frac{S[x_b] - S[x_0]}{2\pi\hbar m}}\frac{\sqrt{\text{Det}\, S''[x_0]}}{\sqrt{|\text{Det}'\, S''[x_b]|}} \tag{3.39}$$

We finally arrive at the central result of this chapter by using (3.9), which gives the decay probability per unit time of the metastable state

$$\begin{aligned}\Gamma &= \frac{2}{T}\,\text{Im}\,\ln Z(T)\\ &= \sqrt{\frac{S[x_b] - S[x_0]}{2\pi\hbar m}}\frac{\sqrt{\text{Det}\, S''[x_0]}}{\sqrt{|\text{Det}'\, S''[x_b]|}}e^{\frac{-(S[x_b]-S[x_0])}{\hbar}} \equiv Ae^{-B}\end{aligned} \tag{3.40}$$

with

$$A = \sqrt{\frac{S[x_b] - S[x_0]}{2\pi\hbar m}}\frac{\sqrt{\text{Det}\, S''[x_0]}}{\sqrt{|\text{Det}'\, S''[x_b]|}}, \qquad B = \frac{(S[x_b] - S[x_0])}{\hbar}. \tag{3.41}$$

Note that the above formula is essentially the decay rate at the "one-loop". One in principle can compute higher-order corrections using the effective action formalism [66], see e.g. [67].

So far, we have introduced the knowledge of instantons and bounces in one-dimensional quantum mechanics. This is essential as the discussion can be easily generalized to their analogues in quantum field theory, which is relevant to the main projects of the thesis.

3.3 Tunnelling in quantum field theory

False vacuum decay is a first-order phase transition in quantum field theory with a similar picture to the classical transition from fluid to vapour, which describes the process of fields transitioning from the false vacuum (local minimum) to the true vacuum (absolute minimum) of the potential. It is implemented by having a bubble of true vacuum nucleated from the false vacuum background. Once the energy gained from the volume outweighs the cost of forming a bubble wall, it becomes energetically favourable for the bubble to expand until it fills the entire space or merges with other bubbles. Fig. 3.6 shows a visual representation of the false vacuum decay. In this section, we aim to generalise the theory of tunnelling in quantum mechanics to quantum field theory in a similar fashion, which then describes the false vacuum decay. The Euclidean action of a single scalar field in four-dimensional spacetime is

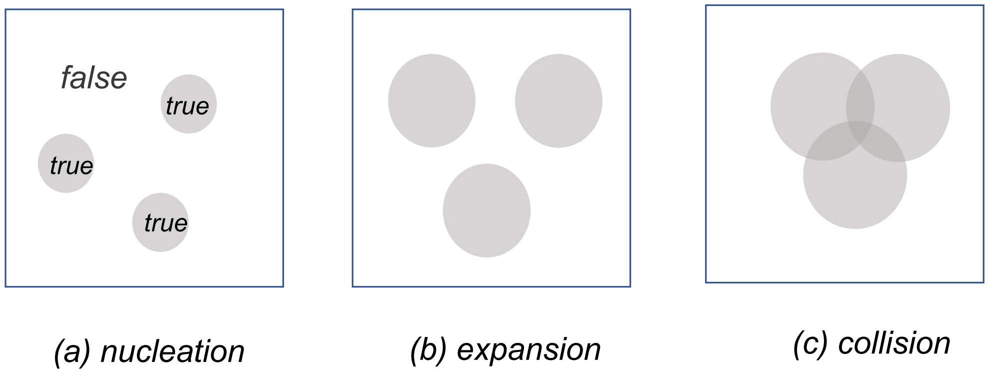

Fig. 3.6 Illustration of the three stages of false vacuum decay. (a) Bubble nucleation: true vacuum bubbles fluctuate into existence in the false vacuum background. (b) Bubble expansion: Bubbles grow and expand within the false vacuum. (c) Bubble collision: Bubbles collide with each other, and the bubble wall coalesces.

$$S_E = \int d^4x \left[\frac{1}{2}(\partial_\mu\phi)^2 + U(\phi)\right] \tag{3.42}$$

where d^4x is the Euclidean spacetime volume element, $(\partial_u\phi)^2$ is the kinetic term, $U(\phi)$ is the potential of the scalar field with two degenerate minima, ϕ_+ and ϕ_-, as illustrated in the left panel of Fig. 3.7. The true vacuum is the lowest energy state with $\phi = \phi_-$. The state with $\phi = \phi_+$ is also a classical equilibrium state, but it becomes unstable through barrier penetration when considering quantum theory, referring to a false vacuum. For simplicity, we renormalise the potential to ensure $U(\phi_+) = 0$. Recapping from the previous section, the tunnelling rate can be calculated by finding a bounce solution to the equations of motion, which describes the decay of an unstable state. The decay rate can be written as

$$\Gamma = Ae^{-B} \tag{3.43}$$

The coefficient B in the vacuum decay amplitude is the difference in Euclidean actions between the two vacua

$$B = S_E(\phi) - S_E(\phi_+) \tag{3.44}$$

The Euclidean equation of motion is

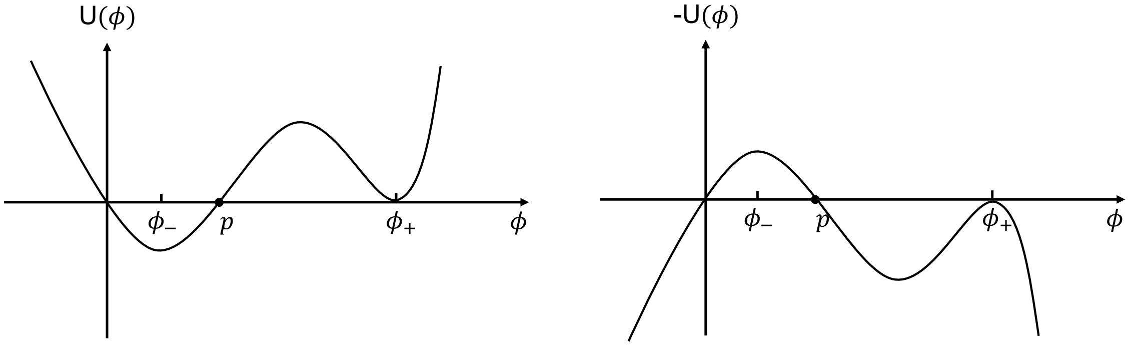

Fig. 3.7 Left: The potential of a scalar field. The local minimum of $U(\phi)$ is defined as the false vacuum at $\phi = \phi_+$, while the global minimum is a true vacuum at $\phi = \phi_-$. The black dot at p is a turning point. Right: The inverted potential $-U(\phi)$.

$$\left(\frac{\partial^2}{\partial\tau^2} + \nabla^2\right)\phi = \frac{dU}{d\phi} \tag{3.45}$$

We start with finding the bounce solution to the equations of motion, denoted by ϕ_b. The boundary condition

$$\lim_{\tau\to\pm\infty} \phi_b = \phi_+ \tag{3.46}$$

which implies the bounce rolls from the false vacuum state at time minus infinity to the potential well and returns to the original vacuum at time plus infinity. The potential well is obtained by flipping the potential upside down. The higher energy barrier, therefore, turns into a potential well, as shown in the right panel of Fig. 3.7.

Additionally, the bounce has zero velocity at $\tau = 0$, where the field arrives at another zero

$$\left.\frac{\partial \phi_b}{\partial \tau}\right|_{\tau=0} = 0 \tag{3.47}$$

Note that in [11], it was argued that there always exists an $O(4)$-invariant bounce with lower action compared to other bounces. Hence, we choose a $O(4)$-invariant bounce solution, and the equation of motion depends only on the radial variable

$$\frac{d^2\phi}{d\rho^2} + \frac{3}{\rho}\frac{d\phi}{d\rho} - U'(\phi) = 0 \tag{3.48}$$

where $\rho = \sqrt{\tau^2 + \mathbf{x}^2}$. The boundary conditions can be rewritten as

$$\lim_{\rho\to\infty} \phi(\rho) = \phi_+, \qquad \left.\frac{d\phi}{d\rho}\right|_{\rho=0} = 0 \tag{3.49}$$

which ensures the solution is regular at the origin.

Following [10, 11], we interpret the field $\phi(\rho)$ as the position of a classical particle and ρ as time. The picture becomes that a particle moves in the flipped potential $-U(\phi)$, subject to a damping force with a coefficient inversely proportional to the time ρ. The particle is initially released at rest at time zero and reaches the false vacuum ϕ_+ at time infinity. The initial position should be properly chosen to avoid undershooting or overshooting. If the released point is sufficiently close to ϕ_-, the overshooting happens and the particle ends up passing ϕ_+ at time infinity. If it is released far from the left of ϕ_-, the particle does not have enough energy to climb the potential barrier and never reaches ϕ_+. It is easy to show undershooting because the viscous damping costs energy:

$$\frac{dE}{d\rho} = \frac{d}{d\rho}\left[\frac{1}{2}\left(\frac{d\phi}{d\rho}\right)^2 - U(\phi)\right] = -\frac{3}{\rho}\left(\frac{d\phi}{d\rho}\right)^2 < 0 \tag{3.50}$$

For overshooting, we linearize the equation of motion around ϕ_-

$$\left(\frac{d^2}{d\rho^2} + \frac{3}{\rho}\frac{d}{d\rho} - \mu^2\right)(\phi - \phi_-) = 0 \tag{3.51}$$

where $\mu^2 = U''(\phi)$. The solution of (3.3) is

$$\phi(\rho) - \phi_- = 2[\phi(0) - \phi_-]\frac{I_1(\mu\rho)}{\mu\rho} \tag{3.52}$$

where $I_1(x) = -iJ_1(ix)$, and J_1 is first order solution of the Bessel differential equation

$$J_1''(x) + \frac{J_1'(x)}{x} + \left(1 - \frac{1}{x^2}\right)J_1(x) = 0. \tag{3.53}$$

If the particle is released close to ϕ_-, it requires very large ρ. But we have the damping force is proportional to $1/\rho$, which can be neglected if ρ is large. Obviously, we conclude that the particle overshoots in the absence of viscous damping. We justify the existence of the $O(4)$-invariant bounce solution.

For a complete introduction to false vacuum decay, we need to compute the exponent coefficient B explicitly via the thin wall approximation. As introduced before, for the nucleated bubble to grow, we must ensure the energy cost for forming the bubble wall should be less than the energy gain from transiting to the true vacuum. We define the model parameters ϵ as the energy density difference between the true and false vacua, and σ is associated with the surface energy density of the bubble wall. It can be approximately expressed as, $\sigma = \int d\phi \sqrt{2(U_\phi - U_{\phi_+})}$, in the thin-wall approximation. The action of the bounce can be written as

$$S_E = -2\pi^2 R^3 \sigma + \frac{\pi^2}{2}\epsilon R^4 \tag{3.54}$$

Any solution should be a stationary point of the action, which can be obtained via

$$\delta S_E = \frac{d}{dR}(-2\pi^2 R^3 \sigma + \frac{\pi^2}{2}\epsilon R^4) = -6\pi^2 R^2 \sigma + 2\pi^2 \epsilon R^3 \equiv 0 \tag{3.55}$$

This energy shift is stationary at $R_{crit} = 3\sigma/\varepsilon$ which corresponds to a calculation of Euclidean field equations. The exponent part of the probability for the critical bubble as

$$B_{crit} = 27\pi^2\sigma^4/2\epsilon^3\hbar \tag{3.56}$$

This gives the nucleation rate of bubbles at a given radius. One should note that the size of the bubble depends on the competition between the wall tension and the energy difference. A critical bubble is formed when the energy gained from tunnelling is just sufficient to balance the wall tension.

3.4 Tunnelling in curved spacetime

The method of describing vacuum decay via the mathematical tool of analytical continuation of imaginary (Euclidean) time has been discussed in the previous section. The intuitive picture demonstrates that a spherical bubble of true vacuum fluctuates into existence from the false vacuum. In this section, we summarize the studies of false vacuum decay in curved spacetime by following Coleman and de Luccia (CDL), where the impact of gravity was first considered in [12].

The studies of quantum tunnelling with gravity come naturally for two main reasons. One is that the energy difference between false and true vacuum may have a different gravitational signature as energy gravitates in curved spacetime. The other refers to the necessity of incorporating quantum phenomena alongside gravitational effects to achieve a more comprehensive understanding of quantum gravity. One might argue that vacuum decay happens on scales with gravitational effects that can be completely neglected. However, this is only a valid point when considering bubble nucleation. As shown in Fig. 3.6, FVD will be completed in three steps: nucleation, expansion and collision. The bubble grows and gains energy from transitioning to the true vacuum after being nucleated. The radius of growing bubbles can eventually be comparable to the Schwarzschild radius [12]. Therefore, it is of significant importance to study FVD under the impact of gravity.

The CDL procedure is to construct a bounce solution which interpolates between the true and false vacuum across the wall, using the Israel conditions to calculate the wall trajectory [68]. We consider the example of a false vacuum that has energy $\Lambda = 8\pi G\epsilon$ in de-Sitter (dS) spacetime, connecting to a true vacuum bubble in Minkowski spacetime. The energy difference ϵ between false and true vacuum is extremely small if we use thin-wall approximation. The length scale, $\ell = \sqrt{3/8\pi G\epsilon}$, is fairly large, such that the dS spacetime can be viewed as approximately flat. We seek a solution to Einstein's equations that precisely describe those properties in the thin wall limit by using the Israel junction condition [68]. The bubble geometry has dS spacetime on the inside and Minkowski on the outside:

$$ds^2 = \begin{cases} d\rho^2 + \ell^2 \sin^2(\rho/\ell) d\Omega_3^2 & \text{FV (dS)} \\ dr^2 + r^2 d\Omega_3^2 & \text{TV (Minkowski)} \end{cases} \tag{3.57}$$

One can stitch the boundary within dS spacetime to the boundary within Minkowski spacetime. The wall is located at $r_0 = \ell \sin(\rho_0/\ell) = R$, with normal $d\rho/dr$. The induced metric h_{ab} on each side are the same, and the wall extrinsic curvature on each side can be written as

$$K_{ab} = -\Gamma^c_{ab} = \begin{cases} \frac{\cot(\rho_0/\ell)}{\ell} h_{ab} & \text{FV (+)} \\ \frac{1}{r_0} h_{ab} & \text{TV (-)} \end{cases} \tag{3.58}$$

The jump in extrinsic curvatures is related to the energy of the wall via the Israel equations

$$K^+_{ab} - K^-_{ab} = -\frac{1}{R}\left(1 - \sqrt{1 - \frac{R^2}{\ell^2}}\right) h_{ab} = -4\pi G\sigma h_{ab} \tag{3.59}$$

The bubble radius can be solved as

$$R_{bubble} = \frac{4\pi\ell^2\bar{\sigma}}{4\pi G\ell^2\bar{\sigma}^2 + 1} \tag{3.60}$$

where we define $\bar{\sigma} = 2\pi G\sigma$ for the compactness of notation. The full Euclidean action of the bubble geometry is composed as

$$S_{E,\ instanton} = \int_{M_+} \frac{\mathcal{R}_+ + 2\Lambda_+}{16\pi G} + \int_{M_-} \frac{\mathcal{R}_- + 2\Lambda_-}{16\pi G} + \int_{wall} \sigma + \int_{\partial M_+} \frac{K_+}{8\pi G} - \int_{\partial M_-} \frac{K_-}{8\pi G} \tag{3.61}$$

We do not need explicit formulations for the contribution from outside of the wall. Because we are only interested in the action difference between the initial and final states, and the two solutions exhibit identical behaviour at infinity, such that the action outside of the bubble reduces to zero after the background subtraction. Only the inside and wall itself contribute to the final expression. Hence, the bubble action is computed by substituting the bubble radius (3.60)

$$S_{bubble} = S_{E,\ instanton} - S_{E,\ fv} = \frac{\pi \ell^2}{G} \frac{16\bar{\sigma}^4 \ell^4}{(1+4\bar{\sigma}^2\ell^2)^2} \tag{3.62}$$

3.5 Seeded tunnelling

The CDL bubbles we described in the last section are idealised with maximal symmetry and no inhomogeneity, however, most first-order phase transitions are triggered by impurities. Especially at the time when phase transition happens, the universe is not smooth and featureless. Impurities may change the rate of bubble nucleation and, subsequently, the growth of the bubble. Taking this idea on board, we look into the studies of seeded tunnelling by impurities. The nature of the impurities varies from local overdensities [69, 70] to topological defects (like cosmic strings [71–73], domain walls [74] or monopoles [75–78]). Here, we focus on the most symmetric example: black holes act as nucleation sites seeding false vacuum decay [79–82]. Black holes are considered gravitational impurities that break the maximal symmetry but retain enough symmetry to allow analytic analysis (for the thin wall approximation).

3.5.1 Bubble dynamics and decay rate

The setup now becomes a black hole embedded in the false vacuum background. A bubble grows in the vicinity of the black hole, with its interior region turning into a true vacuum while the exterior region remains in a false vacuum. We will briefly summarize the result of [79], where the instanton geometry becomes a thin wall solution interpolating between two different Schwarzschild black holes with different cosmological constants. The problem of finding the geometry of a wall in the presence of a bulk black hole reduces to a Birkhoff theorem which was first generalised to arbitrary Λ and black hole curvature in [83], where a domain wall was also included in the analysis. Integrability of the vacuum Einstein equations shows that the general solution is comprised of two exact Schwarzschild (A/dS) geometries are separated by a domain wall that follows a possibly dynamical trajectory

$R(\lambda)$ centered with respect to the black holes. On each side of the wall, the geometry has the form

$$ds^2 = f_\pm(r)d\tau_\pm^2 + \frac{dr^2}{f_\pm(r)} + r^2 d\Omega_{II}^2 \tag{3.63}$$

with

$$f_\pm(r) = 1 - \frac{2M_\pm}{r} - \frac{\Lambda_\pm}{3}r^2 \tag{3.64}$$

It is straightforward to find solutions to the Israel equations, which relate the interior region with mass M_- and cosmological constant Λ_- to the exterior with mass M_+ and cosmological constant Λ_+. The seeded tunnelling will remove some or all of the black hole mass, leaving a remnant black hole or not, so we have $\Lambda_+ \geq \Lambda_-$ and $M_+ \geq M_-$. The trajectory of the bubble is determined by following the Israel junction [68],

$$\dot{R}^2 = 1 - \left(\bar{\sigma}^2 + \frac{\bar{\Lambda}}{3} + \frac{(\Delta\Lambda)^2}{144\bar{\sigma}^2}\right)R^2 - \frac{2G}{R}\left(\bar{M} + \frac{\Delta M \Delta\Lambda}{24\bar{\sigma}^2}\right) - \frac{(G\Delta M)^2}{4R^4\bar{\sigma}^2} \tag{3.65}$$

where $\Delta M = M_+ - M_-$ and $2\bar{M} = M_+ + M_-$, with similar expressions for Λ. $\bar{\sigma}$ is defined for the compactness of notation, $\bar{\sigma} = 2\pi G\sigma$.

Now we turn to the calculations of the decay rate seeded by black holes. We show the general methodology for computing the bounce action, although it is slightly distinct depending on the sign of Λ[2]. The full Euclidean action of the composite system with a thin wall is

$$\begin{aligned} S_E = &-\frac{1}{16\pi G}\int_{\mathcal{M}_+}\sqrt{g}(R_+ + 2\Lambda_+) - \frac{1}{16\pi G}\int_{\mathcal{M}_-}\sqrt{g}(R_- + 2\Lambda_-) \\ &+ \frac{1}{8\pi G}\int_{\partial\mathcal{M}_+}\sqrt{h}K_+ - \frac{1}{8\pi G}\int_{\partial\mathcal{M}_-}\sqrt{h}K_- + \int_{\mathcal{W}}\sigma\sqrt{h} \end{aligned} \tag{3.66}$$

where $\mathcal{M}_\pm$ represent interior/exterior regions of the thin wall, and $\partial\mathcal{M}_\pm$ are the inner/outer boundaries at the wall. The exponential part of the decay rate after subtracting the background action is [79]:

$$B = \frac{\mathcal{A}_+}{4G} - \frac{\mathcal{A}_-}{4G} + \frac{1}{4G}\oint d\lambda\left\{\left(2Rf_+ - R^2 f_+'\right)\dot{\tau}_+ - \left(2Rf_- - R^2 f_-'\right)\dot{\tau}_-\right\} \tag{3.67}$$

---

[2] Different value of Λ has different boundaries at infinity, while it does not affect the final result for the instanton action as its contribution will be eliminated by background subtraction.

This expression indicates the bounce action is the sum of entropy changes and the contribution from the wall. It is independent of any choice of the Euclidean time as well as the cosmological constant.

For a static solution, the action of these instantons is particularly simple, and (3.67) becomes the entropy change in the geometry:

$$B = \frac{\mathcal{A}_+}{4G} - \frac{\mathcal{A}_-}{4G} \tag{3.68}$$

which corresponds neatly to a Boltzmann suppression for tunnelling that decreases entropy.

Based on the result we obtained above, it is now easy to consider the seeded tunnelling with a remnant black hole immersed in the true vacuum. There is an allowed range for M_- with the given vacuum energy differential for each seed mass M_+. The unique M_- that minimises this action, hence dominates the tunnelling amplitude. In [79], it was shown that for small M_+ this minimal M_- vanishes, hence these instantons are perturbed CDL bubbles, whereas for larger M_+ there is a remnant black hole, with a mass determined by M_+, Λ_+ and Λ_-.

A comparison of the decay rate between black hole-seeded vacuum decay and CDL bounces can be found in [79, 80]. The main conclusion is that black holes could speed up the decay, and the decay rate can be enhanced drastically for primordial black holes.

3.5.2 Hawking Moss transition

An alternate description of vacuum decay is given by Hawking Moss (HM) instanton, which describes an up-tunnelling of the false vacuum to a local maximum of the potential, allowing a roll-down to the true minimum [84]. The two tunnelling processes can be best illustrated via the cartoon of a particle in a one-dimensional potential barrier, as shown in Fig. 3.8.

The first order, or bubble nucleation, process corresponds to a particle transitioning from the local minimum on one side of the barrier to the other side. In the HM transition on the other hand, the particle "jumps" to the top of the potential, then rolls down to the true minimum. This HM channel was shown to be relevant for potentials with a gently

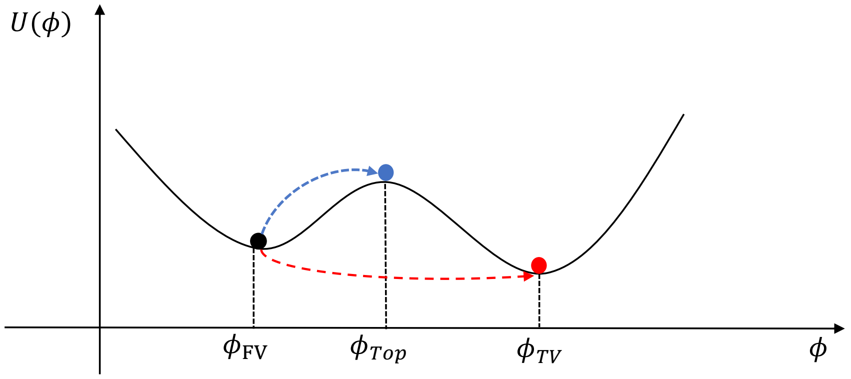

Fig. 3.8 The schematic plot of a one-dimensional potential that has two different minima, with the higher (lower) representing false (true) vacuum, labelled as ϕ_{FV} and ϕ_{TV}, respectively. The top of the potential barrier is labelled as ϕ_{Top}. A particle initially at the local minimum can arrive at the global minimum by two mechanisms: (i) Bubble nucleation (red) - quantum tunnelling to true vacuum or (ii) HM transition (blue) - climbing to the top of the potential and then rolling down to the true vacuum.

varying barrier (the bound being on the second derivative of $V(\phi)$ at the local maximum). The HM rate is given by

$$\Gamma_{F\to T} \sim e^{-B} \tag{3.69}$$

where B is the difference in the Euclidean actions of the two vacuum de Sitter spacetimes:

$$I_{HM} = I_T - I_F = S_F - S_T = \frac{\pi}{G}\left[\ell_F^2 - \ell_T^2\right] \tag{3.70}$$

which again is a Boltzmann factor related to the drop in entropy incurred by the cosmological horizon area decreasing. The corresponding process for the Black-Hole-Hawking-Moss (BHHM) instantons was considered in [85, 86], where the action includes the black hole horizon:

$$B_{F\to T} = I_T - I_F = [S_{CH} + S_{BH}]_F - [S_{CH} + S_{BH}]_T\ . \tag{3.71}$$

where S_{CH} and S_{BH} are the entropy defined at the cosmological horizon and event horizon, correspondingly. In Schwarschild de-Sitter spacetime, the two horizons $r_{c,h}$ coincide when M runs to Nariai maximum,

$$M_N = \frac{\ell}{3\sqrt{3}} \tag{3.72}$$

such that there is an upper bound for the mass parameter. The BHHM transition action is then totally determined by the areas of the horizons, which can be compactly expressed as

$$B = \pi\left[\tfrac{4}{3}\left(\ell_F^2 - \ell_T^2\right) - \tfrac{2}{3}\ell_F^2\cos(2b_F) + \tfrac{2}{3}\ell_T^2\cos(2b_T)\right] \tag{3.73}$$

by using the reparametrisation

$$r_c = \frac{2}{\sqrt{3}}\ell\cos\left(\tfrac{\pi}{3} - b\right), \quad r_h = \frac{2}{\sqrt{3}}\ell\cos\left(\tfrac{\pi}{3} + b\right), \quad b = \frac{1}{3}\cos^{-1}\left(\frac{3\sqrt{3}GM}{\ell}\right) \tag{3.74}$$

in which ℓ_F and ℓ_T are fixed by the potential, and the action difference is determined by the masses of seed or remnant black hole. The full details can be found in [85, 86], with an outcome broadly similar to the bubble nucleation process, namely, that black holes enhance the probability of tunnelling.

It is important to highlight a crucial difference between bubble nucleation and HM transitions. There can only be a remnant black hole if there is a black hole seed to nucleate the decay for bubble nucleation. However, for HM transitions, it is possible to jump from a pure de Sitter false vacuum to a Schwarzschild de Sitter configuration at the top of the potential barrier.

Before concluding this chapter, it is worth noting that the classical analytical results obtained above are within the *thin wall* approximation, in which the vacuum transitions completely and instantaneously across the wall. The thin wall approximation, while excellent for testing gravitational effects, is only a good approximation for vacuum transitions in scalar fields when the potential barrier is sharp. In this thesis, we will stay with the thin wall approximation. In the following chapter, we propose that a primordial black hole lives in the ambient of the plasma heated by its Hawking radiation and reaches thermal equilibrium before completely evaporating. Such a realistic environment validates the Euclidean method as well as the thin wall approximation, despite not being in Hartle-Hawking equilibrium. In Chapter 5, we are interested in the effect of higher curvature gravitational terms on instantons in general. The Euclidean method extracts the impact from gravitational fields very well. Therefore, it is appropriate to study the impacts from extra dimensions as well as the additional Gauss-Bonnet term.

Chapter 4

False vacuum decay with primordial black holes

This chapter is based on the article *Primordial Black Holes Are True Vacuum Nurseries* published in Physics Letters B [87], in collaboration with Louis Hamaide, Lucien Heurtier and Andrew Cheek.

4.1 Introduction

In the case of a black hole-seeded phase transition, one of the key comparisons is with the rate of evaporation of the black hole. In this chapter, we apply the seeded false vacuum decay to primordial black holes (PBHs) and compare the decay rate with Hawking evaporation. It has been demonstrated in [79–82] that the probability of tunnelling can be drastically increased by a light PBH when it is evaporating or near the end of their life. Page showed in [88] that a black hole can radiate energy and lose mass at a rate proportional to $1/M^3$. Any PBHs lighter than 4.5×10^{14}g at formation would have evaporated completely long before the onset of Big Bang Nucleosynthesis (BBN). Due to the significantly high evaporation rate for light PBHs, it is important to ensure that the seeded decay occurs before the PBH completely evaporates.

The previous results are obtained by using the so-called Hartle-Hawking vacuum — in which PBHs are in thermal equilibrium with their surrounding plasma [89]. However, light PBHs can be extremely hot for seeded tunnelling to be relevant with temperature given by $T_H = (8\pi GM)^{-1}$, which would have a substantial impact on the local environment. This can lead to controversy: PBHs rarely equilibrate with their surroundings and several authors pointed out that the Unruh vacuum [90] — in which PBHs evaporate in an empty Universe — should be used instead, largely mitigating the aforementioned result [79–82]. Moreover, thermal corrections were argued to increase the energy of true vacuum bubbles for PBHs lighter than $\mathcal{O}(10^3)$g, effectively rescuing the electroweak-vacuum stability [91]. To address the problem, we propose that PBHs neither live in a vacuum nor are in thermal equilibrium with their surroundings in reality. They deposit energy locally into the thermal plasma via Hawking radiation, forming hot spots around them [92, 93]. Here we provide a new avenue to calculate decay rates around PBHs, building on the results derived in [79–82, 94], to show that the presence of such hot spots does indeed seed the formation of true vacuum bubbles, circumventing the aforementioned criticisms.

4.2 Bubble action

We start this section by considering a homogeneous scalar field configuration ϕ living in a metastable minimum of its potential $V(\phi)$. The decay rate of this configuration is determined in curved spacetime by a saddle point "bounce" solution of the Euclidean action. Around a Schwarzschild black hole living in a background plasma with arbitrary constant temperature, one can write the Euclidean action of a time-independent scalar field bubble configuration as in [79]

$$I[T] = \beta \int dx^3 \, \sqrt{g} \left(-\frac{R}{16\pi G} + \frac{1}{2} \partial_\mu \phi \partial^\mu \phi + V(\phi) \right). \tag{4.1}$$

in which g is the determinant of the metric — assumed to be time-independent as well — and $\beta = 1/T$ denotes the Euclidean time periodicity. At first sight, because β appears in this expression as an overall factor, it is tempting to conclude that a low plasma temperature would lead to a large bubble action, hence suppressing the FVD rate $\Gamma \sim e^{-I_\text{b}[T]}$ exponentially.

However, one should note that there are two pieces missing in (4.1) [79]. First, the gravitational background action should be subtracted to extract the actual energy of the bubble, which is the change in action when nucleating the bubble. Second, if the temperature entering the Euclidean action's periodicity differs from the black hole's Hawking temperature, the system features a conical deficit at the horizon that needs to be accounted for in the calculation. We present a method for calculating the conical deficit contribution using a mathematical regularization process in Appendix B. We summarize this by using the temperature profile interpolating over a scale ϵ between a constant temperature $T(r) = T$ for $r - r_H \gg \epsilon$, and $T(r_H) = T_H$ at the horizon, one can show that the Ricci contribution to the action is of order

$$I[T] \supset -\frac{\beta_H - \beta}{\beta}\frac{\mathcal{A}}{4G} + O(\epsilon)\,, \tag{4.2}$$

in the $\epsilon \to 0$ limit. In this equation $\mathcal{A}$ stands for the black hole's area and $\beta_H = 1/T_H$.

After summing up all the contributions, in the $\epsilon \to 0$ limit, the β-dependency of the total Euclidean action exactly cancels, leading to the seminal result of (3.68). Here we rewrite it as

$$I_{\mathrm{b}}[T] = \frac{\mathcal{A}_+}{4G} - \frac{\mathcal{A}_-}{4G} = I_{\mathrm{b}}[T_H]\,, \tag{4.3}$$

The bounce action only depends on the area of the black hole horizon before and after bubble formation. This property was then generalised beyond the thin-wall approximation, and in the presence of matter [80]. Despite its remarkable generality, this result was only used in the Hartle-Hawking vacuum where PBHs are in thermal equilibrium with temperature $T = T_H$ to derive constraints on PBHs using the electroweak vacuum stability.

In what follows, we will show that in a realistic cosmological set-up, PBHs live in a plasma with a temperature lower than their Hawking temperature, but also that the mathematical smoothing used to derive (4.2) actually corresponds to a physical situation.

4.3 Thermal profile around PBHs

Throughout cosmic history, PBHs are surrounded by two main sources of energy: (*i*) the Hawking radiation, made of particles with energy $E \sim T_H$, and (*ii*) the ambient plasma, populated with particles of energy $E \sim T$. Studies considering the Hartle-Hawking vacuum assume that $T = T_H$ and both energy sources are in perfect equilibrium. Instead, studies working with the Unruh vacuum only consider the Hawking radiation, effectively working in the limit where $T \to 0$.

As a matter of fact, both pictures are incomplete. When PBHs form, the Universe's temperature may be much larger than their Hawking temperature. However, the end of PBH evaporation typically takes place when the Universe is much colder than the initial PBH Hawking temperature. Nevertheless, a big piece is missing in this discussion: in the intermediate period, the quanta that form Hawking radiation unavoidably interact with the surrounding plasma, heating up the surrounding plasma locally. This energy deposition leads to an inhomogeneous temperature profile forming around PBHs that persists long after they have completely evaporated, and can differ by orders of magnitude from the average temperature in the Universe.

This temperature profile evolution was explored in [92, 93]. Assuming a universal coupling constant α to encode particle interactions between Hawking radiation and the plasma, in a recent study [93], it was demonstrated that for PBHs with masses

$$M \quad \gtrsim \quad M_\star\,, \quad \text{where } M_\star \equiv 0.8\text{g}\left(\frac{\alpha}{0.1}\right)^{-\frac{11}{3}}\,, \tag{4.4}$$

the formation of a hot spot is quicker than the black hole evaporation. PBHs are thus rapidly surrounded by an initial hot spot featuring a homogeneous temperature

$$T_{\text{plateau}} \quad \approx \quad 2\times 10^{-4} T_H \left(\frac{\alpha}{0.1}\right)^{\frac{8}{3}} \left(\frac{g_\star(T_H)}{g_\star(T_{\text{plateau}})}\right)^{\frac{2}{3}}\,, \tag{4.5}$$

over a distance

$$r_{\text{plateau}} \quad \approx \quad 7\times 10^{8}\, r_H \left(\frac{\alpha}{0.1}\right)^{-6} \left(\frac{g_\star(T_H)}{g_\star(T_{\text{plateau}})}\right)^{-1}\,, \tag{4.6}$$

where $g_\star(T)$ denotes the number of relativistic degrees of freedom at temperature T. The evaporation time

$$t_{\rm ev} \equiv \Gamma_{\rm ev}^{-1} \tag{4.7}$$

with

$$\Gamma_{\rm ev} \equiv |\dot{M}/M| \propto M^{-3} \tag{4.8}$$

can be calculated from e.g.[95, 96], this temperature is constant. On larger distances, diffusion dominates over energy deposition and the temperature decreases down to the Universe's temperature at infinity.

Later on, the PBH mass starts decreasing, its Hawking temperature increases, and so does the plateau temperature, while its radius decreases. After the critical point at $M = M_\star$, the plateau temperature then saturates at [93]

$$T_{\rm max} \approx 2 \times 10^9 {\rm GeV} \left(\frac{\alpha}{0.1}\right)^{\frac{19}{3}} \left(\frac{g_\star(T_{\rm max})}{106.75}\right)^{-\frac{4}{3}} \left(\frac{g_\star(T_H)}{106.75}\right)^{\frac{5}{6}}, \tag{4.9}$$

over a radius

$$r_{\rm max} = r_{\rm plateau} \Big|_{T_H = T_{\rm max}} \tag{4.10}$$

At this point, the black hole is not able to provide enough energy to reheat the hot spot further.

To obtain these results, [93] assumed that Hawking radiation particles deposited their energy at an average time

$$t_{\rm dep.} \equiv \Gamma(T)^{-1}, \qquad \Gamma(T) \sim \alpha^2 T \sqrt{\frac{T}{T_H}} \tag{4.11}$$

However, we argue the approximation cannot remain valid near the horizon. Indeed, even if the temperature within the hot spot was perfectly homogeneous, the energy deposition probability of Hawking radiation,

$$dP \sim \Gamma(T) e^{-(r-r_H)\Gamma(T)} dr, \tag{4.12}$$

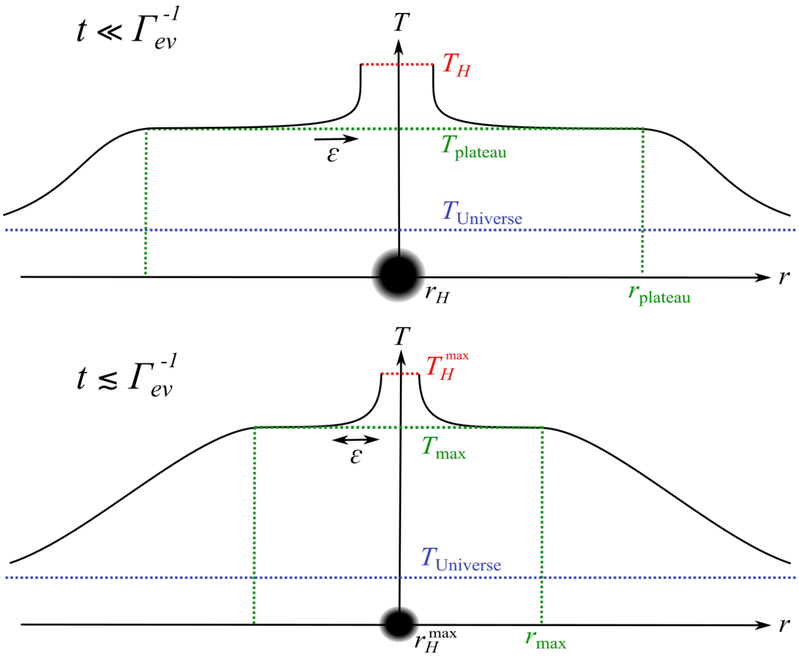

Fig. 4.1 Sketch of the temperature profile around PBHs throughout the evaporation process.

is a decreasing function of the radius. In addition, the Hawking radiation energy density also decreases like r^{-2}. Energy deposition is thus more efficient close to the horizon, leading to a local increase of the temperature. This increase also corresponds to an enhancement of $\Gamma(T)$. Therefore, the plasma temperature is likely to increase at the horizon, interpolating between the Hawking temperature and the hot spot temperature calculated on larger distances in (4.5) and (4.9). In Fig. 4.1, we sketch the qualitative temperature profile that must be present around PBHs at $t \ll \Gamma_{\text{ev}}^{-1}$, when the hot spot core temperature is T_{plateau} (upper panel), and at $t \lesssim \Gamma_{\text{ev}}^{-1}$, when the plateau temperature saturates at $T_{\max}$ (lower panel). Note that by enforcing the smooth behaviour of the plasma $T \to T_H$ as $t \to r_H$, we have introduced a physical realisation of the regularisation procedure used in [79] to evaluate the conical deficit contribution to the action in (4.2). In full generality, one would need to solve the heat equation around PBHs to obtain the exact temperature profile and to evaluate the smoothing size ε that is sent to zero to obtain (4.3). For simplicity, we assume here that the typical size of this smoothing is negligible as compared to the size of a true-vacuum bubble and leave a precise study of the profile geometry contribution for future work.

4.4 Bounce solution and nucleation rate

We consider a homogeneous scalar-field configuration ϕ_+ living in a metastable minimum of its potential where $V(\phi_+) = 0$ before tunnelling to the true vacuum, located at ϕ_-, for which $V(\phi_-) < 0$. Following [94], we parametrise the metric as

$$ds^2 = f_E(r)e^{2\delta(r)}d\tau^2 + \frac{dr^2}{f_E(r)} + r^2 d\Omega_2^2\,, \tag{4.13}$$

with

$$f_E(r) = 1 - \frac{2G\mu(r)}{r} \tag{4.14}$$

where $\mu(r)$ is the local mass parameter, and search for the classical solution $\phi(r)$ satisfying the equations of motion

$$\begin{aligned} f_E\phi'' + f_E'\phi' + \frac{2}{r}f_E\phi' + \delta' f_E\phi' - V'(\phi) = 0 \\ \mu' = 4\pi r^2\left(\frac{1}{2}f_E\phi'^2 + V\right) \\ \delta' = 4\pi G r\phi'^2 \end{aligned} \tag{4.15}$$

The boundary conditions at the horizon are

$$\begin{aligned} \mu(r_H) = \mu_-, \qquad \delta(r_H) = 0 \\ \phi'(r_H) = \frac{r_H V'(\phi_H)}{1 - 8\pi G r_H^2 V(\phi_H)}, \end{aligned} \tag{4.16}$$

and at $r \to \infty$ are

$$\lim_{r\to\infty}\phi(r) \to \phi_+\ ,\ M_+ \equiv \lim_{r\to\infty}\mu(r)\,. \tag{4.17}$$

Assuming that the energy of the bubble is entirely provided by the local mass variation inside the bubble, and the black hole mass at infinity, M_+, remains unchanged during the phase transition. In the near horizon limit, due to the presence of a negative cosmological constant $\Lambda_- \equiv V(\phi_-)$, the mass parameter $\mu_- \equiv \lim_{r\to r_H}\mu(r)$ slightly differs from the physical black hole mass inside the bubble, M_-, such that

$$r_H = 2G\mu_- = 2GM_- + \Lambda_- r_H^3/3 \tag{4.18}$$

With such a solution in hand, one can calculate the bounce action (4.1) numerically. Assuming a local thermal equilibrium around PBHs with a temperature profile $T(r)$ such that $\lim_{r\to r_H} T(r) = T_H$, the metric does not feature any conical singularity, but the contribution of the effective conical deficit at infinity is entirely contained in its contribution to the Ricci scalar. For simplicity, we will assume that the interpolation distance ε is small enough that the regularisation procedure described in Appendix B is sufficient, enabling us to use (4.3).

Despite the powerful generality of (4.3), the FVD rate calculation was always restricted to the Hartle-Hawking case [79–82, 94]. Using dimensional analysis to obtain the prefactor, this rate was obtained by writing [80–82],

$$\Gamma_{\text{FVD}}^{\text{HH}} \equiv (GM_+)^{-1}\left(\frac{I_{\text{b}}[T_H]}{2\pi}\right)^{1/2} \exp\left(-I_{\text{b}}[T_H]\right). \tag{4.19}$$

Because $(GM_+)^{-1} \sim T_H$, one can interpret this result as a thermal FVD rate evaluated at $T = T_H$ [97, 98]. By analogy, we propose to generalise this result to the case of a hot spot with temperature $T < T_H$ using instead

$$\Gamma_{\text{FVD}}(T) \quad \approx \quad T\left(\frac{I_{\text{b}}[T_H]}{2\pi}\right)^{1/2} \exp\left(-I_{\text{b}}[T_H]\right), \tag{4.20}$$

where we used (4.3) such that $I_{\text{b}}[T_H] = I_{\text{b}}[T]$ in this expression. Consequently, the suppression of the rate in the case where $T < T_H$ is only linear, as the hot spot temperature only appears in the overall prefactor. Before we use this result for phenomenological purposes, let us discuss what value of T is reasonable to use in (4.20): before they evaporate, PBHs with $M \gtrsim 0.8$g are surrounded by a plasma with temperature $T_{\text{plateau}} \approx 2\times 10^{-4} T_H$. This temperature remains constant throughout most of the PBH lifetime, enabling the use of the Euclidean formalism. Therefore, one can safely use T_{plateau} to calculate the nucleation rate. However, this choice is extremely conservative. Indeed, PBHs heavier than $M_\star$

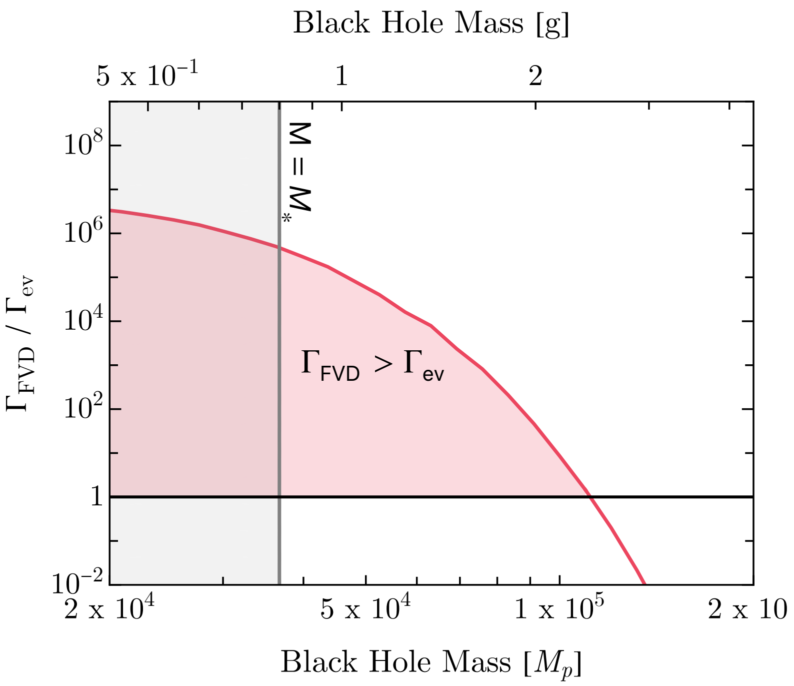

Fig. 4.2 Evolution of $\Gamma_{\rm FVD}/\Gamma_{\rm ev}$ with the PBH mass, using the initial plateau temperature $T_{\rm plateau}$ (red curve). In the grey-shaded area, $M < M_\star$, and in the red-shaded area, the ratio is larger than unity.

are expected to evaporate and reach a point where $M = M_\star$ and the hot spot temperature reaches $T_{\rm max}$. Then, $T_{\rm max} \geqslant T_{\rm plateau}$ and $I_b[T_H]|_{M=M_\star} \ll I_b[T_H]|_{M>M_\star}$, leading to a much larger FVD rate. A legitimate concern is whether the Euclidean formalism is reliable given that the PBH and its environment is dynamical. To ensure this, we restrict ourselves to cases where the characteristic timescales are much larger than the FVD, *i.e.* $\Gamma_{\rm FVD}/\Gamma_{\rm ev} \gg 1$.

4.5 The Electroweak Vacuum

Let us now apply our results to the case of the electroweak vacuum. To calculate $\Gamma_{\rm FVD}$, we parameterise the Higgs potential,

$$V(\phi) = \left[\lambda_* + b\left(\ln\frac{\phi}{M_p}\right)^2 + c\left(\ln\frac{\phi}{M_p}\right)^4\right]\phi^4/4\,, \tag{4.21}$$

where we determined the parameters $(\lambda_*, b, c) = (-3.2\times 10^{-3}, -1.497\times 10^{-6}, 5.42\times 10^{-8})$ using updated top-quark mass measurements from CMS [99] with the package PyR@te

3 [100, 101] to obtain the RG-improved Higgs potential at three loops. To this zero-temperature potential, we added one-loop thermal corrections, $\Delta V(\phi, T) = \kappa^2 T_{\text{plasma}}^2 \phi^2$, where $\kappa = 0.35$ following [91]. Given these parameters, the electroweak vacuum appears to be metastable, although its lifetime is much longer than the age of the Universe in the absence of PBHs [102–105]. In [94], the effect of PBHs on electroweak FVD was used to derive constraints on PBH production in the early universe. Here, we propose to use (4.20) to obtain more realistic results.

4.6 Primordial black hole bounds

In Fig. 4.2, we depict the evolution of $\Gamma_{\text{FVD}}/\Gamma_{\text{ev}}$ with different mass M. As one can see, $\Gamma_{\text{FVD}}/\Gamma_{\text{ev}} \gtrsim 1$ for $M_\star < M \lesssim 2\text{g}$. However, Γ_{FVD} is exponentially suppressed for larger masses. Remarkably, this ratio reaches $5 \times 10^5 \gg 1$ at $M = M_\star$. PBHs with large initial masses — for which $\Gamma_{\text{FVD}}(T_{\text{plateau}})/\Gamma_{\text{ev}} \ll 1$ — thus seed a much larger FVD rate once $M = M_\star$, and the FVD is a much faster process than the PBH evaporation at that point. For PBHs with initial masses $M < M_\star$, the hot spot does not have enough time to form in the first place [93]. However, PBHs with initial masses larger than $M_\star$, will eventually enter this region when they evaporate. Then, such PBHs do not have enough energy to reheat the hot spot, whose temperature remains constant at $T = T_{\text{max}}$ throughout the end of the evaporation. In this region, we thus fixed $T = T_{\text{max}}$ in the calculation.

In [91], the effects of thermal corrections were claimed to become sizeable for $M \lesssim 10^3\text{g}$. However, such effects only become relevant for $M \lesssim 0.1\text{g} < M_\star$ in our case and do not affect any of the conclusions. Indeed, because we consider the temperature $T_{\text{plateau}} \approx 10^{-4} T_{\text{H}}$, the effect of thermal corrections is shifted to lower masses by a factor $\mathcal{O}(10^{-4})$, in agreement with our results. Note also that the bubble profiles we obtain always have radii much smaller than r_{plateau} and r_{max}, validating the assumption of homogeneous plateau temperature that we have used throughout this work. We also checked that by subtracting to the action of (4.1) the background action and adding manually the conical deficit, we recover exactly the result of (4.3).

Assuming that the FVD rate calculation is valid over a time Δt, one can calculate the FVD probability around a single PBH as $P_{\rm FVD} \equiv 1 - e^{-\Gamma_{\rm FVD}\Delta t}$. Since the hot spot temperature remains constant at $T_{\rm plateau}$ during most of the PBH lifetime, one can use $\Delta t \sim \Gamma_{\rm ev}^{-1}$ in that case. In that case, $P_{\rm FVD}(M) = 1 - e^{-\Gamma_{\rm FVD}(T_{\rm plateau})/\Gamma_{\rm ev}}$. Depending on the ratio $\Gamma_{\rm FVD}/\Gamma_{\rm ev}$, this probability can vary over orders of magnitude. Once the black hole starts evaporating and eventually reaches $M = M_\star$, then $\Gamma_{\rm FVD}/\Gamma_{\rm ev} \approx 5 \times 10^5$. This ensures that $P_{\rm FVD} \approx 1$ as long as one considers time scales $\Delta t \lesssim 10^{-6} \times \Gamma_{\rm ev}^{-1}$. Over such a short time, the PBH mass variation is negligible, and the Euclidean formalism still holds.

Given these decay probabilities, we may now look at the ensuing bounds on the share of the earlier universe energy which collapsed into PBHs $\beta_{\rm PBH} = \rho_{\rm PBH}/\rho_{\rm tot}$. At the earliest, PBHs formed when an overdensity of size comparable to that of a Hubble patch collapsed gravitationally. Assuming the Universe to be radiation-dominated then, $\rho_{\rm tot} = \rho_{\rm rad}$, and one can calculate the Universe's temperature at formation to be

$$T_f = \left(\frac{\gamma}{4\pi} \sqrt{\frac{45}{\pi g_\star(T_f)}} \frac{M_p^3}{M} \right)^{1/2} , \tag{4.22}$$

and obtain the value of the density fraction at formation

$$\beta_{\rm PBH} = \frac{4}{3} \frac{M N_{\rm PBH} H_0^3}{s_0 T_f} \approx 2 \times 10^{-80} N_{\rm PBH} \left(\frac{M}{M_\star} \right)^{3/2} , \tag{4.23}$$

where $\gamma = (1/\sqrt{3})^3$ characterizes the gravitational collapse [106, 107], $N_{\rm PBH}$ is the total number of PBHs that, if stable, would be contained in a Hubble patch of size H_0^{-1}, $s_0 \approx 2 \times 10^{-38} {\rm GeV}^3$ is the entropy density today, and $H_0 \approx 70$ km^{-1}s^{-1}Mpc^{-1} is the Hubble constant.

Demanding that the electroweak vacuum has never decayed in our Hubble patch at 95% confidence level is equivalent to requesting that $N_{\rm PBH} P_d < 2.7$, or, when $P_d \approx 1$, that

$$\beta_{\rm PBH} \lesssim 5 \times 10^{-80} \left(\frac{M}{M_\star} \right)^{3/2} . \tag{4.24}$$

In Fig. 4.3, we depict the corresponding constraints when using $T_{\rm plateau}$ and $T_{\rm max}$ for the hot spot temperature. Note that for $M_\star < M < 88$g (4g), the temperature $T_{\rm plateau}$ ($T_{\rm max}$) is

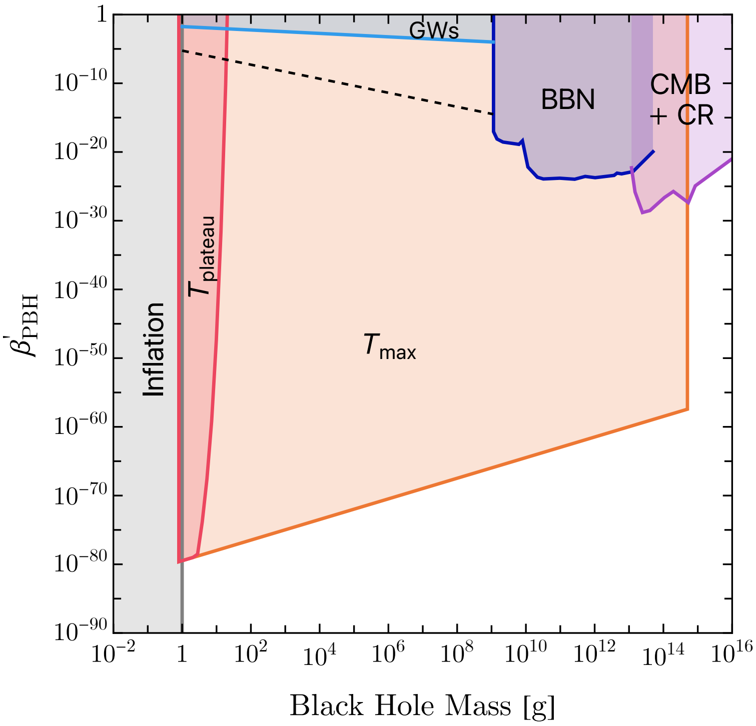

Fig. 4.3 Constraints on the primodal black hole energy fraction at formation, $\beta'_{\rm PBH} \equiv \gamma^{1/2}(g_\star(T_f)/106.75)^{-1/4}\beta_{\rm PBH}$. The orange(red)-shaded region corresponds to constraints derived with $T = T_{\rm max}$ ($T_{\rm plateau}$).

smaller than the plasma temperature at evaporation

$$T_{\rm ev} \equiv \left(\frac{90}{8\pi^3 g_\star(t_{\rm ev})}\right)^{1/4} \sqrt{\Gamma_{\rm ev} M_p}\,. \tag{4.25}$$

In this case, we slightly modified the result of (4.20), by substituting the prefactor T by $\max\{T, T_{\rm ev}\}$. In the regime where such constraints are relevant, we checked that $\Gamma_{\rm FVD}/\Gamma_{\rm ev} \gg 1$, guaranteeing the validity of the Euclidean formalism, and that thermal corrections arising at $T_{\rm ev}$ rather than $T_{\rm plateau}$ or $T_{\rm max}$ still remain subdominant. For comparison, we indicate other constraints from inflation, BBN, Cosmic Microwave Background (CMB) distortion and γ-rays [108].

4.7 Summary

In this work, we discussed the effect of primordial black holes on the stability of the electroweak vacuum in the early Universe. We employed the results that small black holes can trigger Higgs vacuum decay, as we showed in Chapter 3. We responded to the controversy of whether black holes can seed vacuum decay, in which, a series of papers [91, 109–114] have argued that the thermal loop fluctuations could correct the Higgs potential to be stabilized, and computation method – the Euclidean formalism – is not valid.

We showed in our calculation that a hot spot with a temperature higher than the Universe but colder than Hawking temperature is found to surround the PBH. The fact that PBH lives within an equilibrium thermal plasma heated by its Hawking radiation validates the methodology of Euclidean formalism. Also, we compared the ratio of the decay rate and evaporation rate and found that the false vacuum decay occurred earlier than it evaporated totally. We concluded that light PBHs, which have evaporated before today and with an initial mass $M_i > 0.8g$, will trigger vacuum decay.

We then refer to the conclusion that if the electroweak vacuum remains metastable given current and future experimental measurements, such limits exclude any scenario predicting a large abundance of evaporating PBHs in cosmology [115–146] and exclude entirely the possibility that PBHs dominate the Universe before evaporating (above the dotted line in Fig. 4.3). Such constraints are crucial for our understanding of the early Universe dynamics and provide a new perspective on the PBHs in cosmic evolution.

Such PBH scenario should be confirmed by cosmological data, our results may indicate that new physics is required to stabilise the electroweak vacuum throughout cosmic history. Finally, we emphasize that the findings presented in this chapter can be applied to any first-order phase transition taking place in cosmology, which is important in studying the structure and evolution of the early Universe.

Chapter 5

Seeded Vacuum Decay with Gauss-Bonnet

This chapter is based on the paper *Seeded vacuum decay with Gauss-Bonnet* published in Journal of High Energy Physics [147] and the paper *Testing Higher Derivative Gravity through Tunnelling* published in Particles [148], in collaboration with Ruth Gregory.

5.1 Introduction

In this chapter, we investigate false vacuum decay catalysed by black holes under the influence of the Gauss-Bonnet term by studying both bubble nucleation and Hawking-Moss types of phase transition in arbitrary dimensions ($D \geq 4$). The equations of motion of "bounce" solutions in which bubbles nucleate around arbitrary dimensional black holes are obtained in the thin wall approximation, and the instanton action is computed[1].

Theories of modified gravity are developed to address some of the issues that exist in GR, as well as provide a new arena for testing classical gravity in strong gravitational fields. Among these alternatives to GR, higher curvature theories have a uniquely privileged position as they require no extra fundamental fields and can be motivated within a quantum gravity setting. Under the corrections of higher curvature terms, the behaviour of the gravitational field at low energies is almost indistinguishable from what is predicted by GR,

---

[1] Although the thin wall approximation is an idealised description of bubble nucleated vacuum decay, it will suffice for the exploration of the impact of the GB term.

while the difference can be appreciable when considering strong gravity scenarios. As such, it is of particular interest as a means of testing how higher curvature terms alter gravitational phenomena through tunnelling. To establish the foundation for exploring vacuum decay with GB, we begin with a brief overview of the Lovelock gravity [44, 45, 149]

$$S_{lovelock} = \int d^D x \sqrt{g} \sum_i c_i \mathcal{L}_i \,, \tag{5.1}$$

with

$$\mathcal{L}_i = \frac{1}{2^i} \delta^{\mu_1 \dots \mu_{2i}}_{\nu_1 \dots \nu_{2i}} \mathcal{R}^{\nu_1 \nu_2}_{\mu_1 \mu_2} \dots \mathcal{R}^{\nu_{2i-1} \nu_{2i}}_{\mu_{2i-1} \mu_{2i}} \tag{5.2}$$

where the subscript i runs from 0 to $D/2$, c_i are a set of arbitrary constants, $\mathcal{R}^{\mu}_{\nu\rho\sigma}$ are the components of the Riemann tensor, and δ^{μ}_{ν} is the Kronecker delta. The Lagrangian is a scalar built from the metric $g_{\mu\nu}$ and curvature tensor $\mathcal{R}_{\mu\nu\rho\sigma}$. For the first and second-order derivatives, we can write

$$\begin{aligned} \mathcal{L}_1 &= \mathcal{R} \\ \mathcal{L}_2 &= \mathcal{R}^2 - 4\mathcal{R}^2_{\mu\nu} + \mathcal{R}^2_{\mu\nu\rho\sigma} = \mathcal{L}_{GB}, \end{aligned} \tag{5.3}$$

corresponding to the usual Einstein-Hilbert and the Guass-Bonnet term [150–152] respectively. Among the theories containing higher-order corrections, the GB term gives the lowest order of Lovelock contribution and has been better explored.

Einstein-Gauss-Bonnet gravity was first introduced by Lanczos [150] and later generalized by Lovelock [44, 45]. The EGB action is given by adding the GB term to the Einstein-Hilbert Lagrangian [153]

$$S_{EGB} = -\frac{1}{16\pi G} \int_{\mathcal{M}} d^D x \sqrt{g} \left(\mathcal{R} - 2\Lambda + \alpha \mathcal{L}_{GB} \right) \tag{5.4}$$

where α is a coefficient with dimension (length)^2 associated with the GB term (5.3).

The GB scalar is a topological invariant in four dimensions, which cannot give any non-trivial gravitational dynamics. Therefore, the effective theory with a contribution from the GB term only exists in higher dimensions. It may seem strange to consider a correction that does not alter the dynamics of a system, however, when computing the probability of decay, it is the *action* of a process that is relevant, and the GB term can alter the action of a solution, potentially affecting the tunnelling amplitude.

We note that there is a recent novel extension of EGB gravity in four dimensions, known as 4DEGB gravity [154], in which Glavan and Lin have proposed to rescale the coupling constant α by a factor of $1/(D-4)$ and then take the limit $D \to 4$. However, there are certain shortcomings in the validity of this method. For example, this process requires the specification of the geometry to have extra dimensions before taking the reduction to 4D, and it also suffers from a lack of well-defined action and explicit symmetries [155–157]. To address the ambiguities, a new regularisation method introduced a counterterm to cancel the divergence in the action, retaining the desired corrections in four dimensions without the problematic dimensional reduction [158]. Another regularization procedure can be obtained by performing the Kaluza-Klein reduction [159], in which the authors interpreted the 4DEGB theory as a special case within the broader context of Horndeski theories. Both methods ultimately relate this theory to scalar-tensor theories and have been a more widely accepted way of capturing the essence of the GB term in four dimensions (for a detailed discussion, see the review [160]). Those reinterpretations imply that the 4DEGB theory can be more consistently understood within the framework of Horndeski gravity rather than a novel extension of Einstein's General Relativity. However, our research focuses on extracting the impacts of the GB term in general dimensions by comparing it to the corresponding results in Einstein gravity. Hence, we are not interested in the new solution and restrict our investigation of EGB gravity in four-dimensional spacetime to the original theory.

The black hole solutions in the higher dimensional spacetime exhibit richer and more complex structures [161–163], effectively expanding our understanding of black holes beyond GR. The general spherically symmetric vacuum solution is derived in [153, 161],

$$ds^2 = -f(r)dt^2 + f^{-1}(r)dr^2 + r^2 d\Omega_{D-2}^2 \tag{5.5}$$

where $d\Omega^2_{D-2}$ gives the metric of the unit S^{D-2} and we take the 'Einstein' branch solution [163–165]:

$$f(r) = 1 + \frac{r^2}{2\tilde{\alpha}}\left(1 - \sqrt{1 + \frac{8\tilde{\alpha}\Lambda}{(D-1)(D-2)} + \frac{4\tilde{\alpha}\mu}{r^{D-1}}}\right) \tag{5.6}$$

with $\tilde{\alpha} = (D-3)(D-4)\alpha$, and μ related to the mass through the standard Myers-Perry formula [161]:

$$\mu = \frac{16\pi GM}{(D-2)\mathcal{A}_{D-2}} \tag{5.7}$$

with $\mathcal{A}_{D-2}$ being the area of a unit $(D-2)-$sphere. Note that as $\tilde{\alpha} \to 0$, we recover the Schwarzschild solution. Note that the coupling constant is usually considered as a positive value, because: 1) if $\alpha < 0$, there are régimes of parameter space where the argument of the root in (5.6) becomes negative, hence the solution is unphysical. 2) From the perspective of black hole thermodynamics, the positive α avoids the thermodynamic quantities becoming unphysical [163], such as negative entropy that violates the second law. 3) In string theory, α is related to the physical length scale of the string worldsheet action or the inverse string tension, which has to be positive [152]. While what follows is independent of the sign of α, we will focus on $\alpha > 0$ for the following discussion.

5.2 Bubble-nucleated decay

We first briefly review the procedure for finding the instanton, noting how the GB term impacts the argument in general and deriving the action in the presence of the GB term. Gauss-Bonnet instantons with $O(D)-$symmetry were explored in [166] in the context of stability of the different branches of the EGB vacua, here we are looking for solutions with a black hole, hence $O(D-1)$ symmetry.

A bubble separating false vacuum from true vacuum is expected to have SO(3) symmetry, and a generalisation of the Birkhoff theorem in the presence of branes [83] shows that the general bulk solution is Schwarzschild (A/dS) with the bubble surrounding the black hole. This theorem was also demonstrated for GB gravity in [167–169], with the general brane junction conditions derived in [170]. Following the steps we have introduced in Chapter 3, we seek a Euclidean bubble solution $R(\lambda)$ separating two black hole spacetimes with exterior mass M_+ and false vacuum energy Λ_+, and an interior mass M_-, and true vacuum energy Λ_-. The regions exterior and interior to the wall are given by (We Wick rotate (5.5) by using $t = -i\tau$)

$$ds_\pm^2 = f_\pm d\tau_\pm^2 + f_\pm^{-1} dr^2 + r^2 d\Omega_{D-2}^2, \tag{5.8}$$

where

$$f_\pm = 1 + \frac{r^2}{2\tilde{\alpha}} \left(1 - \sqrt{1 + \frac{8\tilde{\alpha}\Lambda_\pm}{(D-1)(D-2)} + \frac{4\tilde{\alpha}\mu_\pm}{r^{D-1}}} \right), \tag{5.9}$$

with the boundary $R(\lambda)$ being given by the generalisation of the Israel prescription to EGB gravity as we now describe.

The full action of the composite system is $I = I_{bulk} + I_{brane}$, where

$$\begin{aligned} I_{bulk} = -\frac{1}{16\pi G} \bigg(\int_{\mathcal{M}_+} d^D x \sqrt{g_+} \left[\mathcal{R}_+ - 2\Lambda_+ + \alpha \mathcal{L}_{GB}^+ \right] \\ + \int_{\mathcal{M}_-} d^D x \sqrt{g_-} \left[\mathcal{R}_- - 2\Lambda_- + \alpha \mathcal{L}_{GB}^- \right] \bigg) \end{aligned} \tag{5.10}$$

represents the contribution from the spacetime away from the wall, and

$$I_{brane} = \int_{\mathcal{W}} d^{D-1} x \sqrt{h} \left(\sigma + \frac{1}{8\pi G} \left(\Delta K - 2\alpha \left[2\mathcal{G}_{ab} \Delta K^{ab} - \Delta \mathcal{J} \right] \right) \right) \tag{5.11}$$

represents the net contribution from the wall, including both the wall tension σ, and the geometrical Gibbons-Hawking terms from the boundary submanifolds on each side: $\partial\mathcal{M}_+ = \partial\mathcal{M}_- = \mathcal{W}$. Here, $K_{\pm ab}$ is the extrinsic curvature of the wall as determined from the local embedding into $\mathcal{M}_\pm$, $\mathcal{G}_{ab}$ is the local intrinsic Einstein tensor of the wall, and $\mathcal{J}$ is a cubic extrinsic tensor (see [170–173]) :

$$\mathcal{J}_{ab} = \frac{1}{3} \left(2KK_{ac}K^c_{\ b} + K_{cd}K^{cd}K_{ab} - 2K_{ac}K^{cd}K_{db} - K^2 K_{ab} \right). \tag{5.12}$$

5.2.1 The instanton solution

In order to find the instanton, we have to solve the equations of motion for the bubble wall, found by varying (5.10) and (5.11). As described in [170], the generalised Israel equations are:

$$\Delta K_{ab} - \Delta K h_{ab} + 2\alpha\left[3\Delta\mathcal{J}_{ab} - \Delta\mathcal{J} h_{ab} - 2\mathcal{P}_{acbd}\Delta K^{cd}\right] = 8\pi G\sigma h_{ab} \tag{5.13}$$

with

$$\mathcal{P}_{abcd} = \mathcal{R}_{abcd} + 2\mathcal{R}_{b[c}h_{d]a} - 2\mathcal{R}_{a[c}h_{d]b} + \mathcal{R}h_{a[c}h_{d]b} \tag{5.14}$$

the divergence free part of the intrinsic Riemann tensor.

Because of the SO(3) symmetry of the bubble, these rather complex relations simplify a little; we write the bubble wall as $R(\lambda)$, where λ is the proper time of an observer comoving with the wall:

$$f_\pm(R)\dot{\tau}_\pm^2 + \frac{\dot{R}^2}{f_\pm(R)} = 1, \tag{5.15}$$

and choosing a normal always pointing towards increasing R for $\dot{\tau}_\pm > 0$,

$$n_\pm = \left(-\dot{R}d\tau_\pm + \dot{\tau}_\pm dr_\pm\right), \tag{5.16}$$

gives, after some algebra, the junction condition as

$$(f_+\dot{\tau}_+ - f_-\dot{\tau}_-)\left[1 + \frac{2\tilde{\alpha}}{R^2} - \frac{4\tilde{\alpha}}{3}\frac{\dot{R}^2}{R^2}\right] - \frac{2\tilde{\alpha}}{3R^2}\left(f_+^2\dot{\tau}_+ - f_-^2\dot{\tau}_-\right) = -\frac{8\pi G\sigma R}{(D-2)}, \tag{5.17}$$

where σ is the surface tension of the wall. Substituting $f_\pm\dot{\tau}_\pm = \sqrt{f_\pm - \dot{R}^2}$ from (5.15) leads to a rather lengthy cubic Friedmann-like equation for $X = (1-\dot{R}^2)/R^2$,

$$\begin{aligned} 0 = {} & \tilde{\alpha}^2 X^3 + \tilde{\alpha}X^2\left(\frac{3}{2} - \frac{(S_+^2 - S_-^2)^2}{256\tilde{\alpha}\bar{\sigma}^2}\right) \\ & + \frac{X}{4}\left(3 - \frac{3(S_+^2 + S_-^2)}{8} - \frac{(S_+^2 - S_-^2)(3S_+^2 - 3S_-^2 + S_+^3 - S_-^3)}{192\tilde{\alpha}\bar{\sigma}^2}\right) \\ & + \frac{(8 - 3S_+^2 - 3S_-^2 - S_+^3 - S_-^3)}{64\tilde{\alpha}} - \frac{(3S_+^2 - 3S_-^2 + S_+^3 - S_-^3)^2}{9216\tilde{\alpha}^2\bar{\sigma}^2} - \frac{9\bar{\sigma}^2}{16} \end{aligned} \tag{5.18}$$

where $\bar{\sigma} = 2\pi G\sigma/(D-2)$ economises on notation, and

$$S_\pm = \sqrt{1 + \frac{8\tilde{\alpha}\Lambda_\pm}{(D-1)(D-2)} + \frac{4\tilde{\alpha}\mu_\pm}{r^{D-1}}} = \sqrt{1 + \frac{4\tilde{\alpha}}{r^2}(1 - f_{\pm E})} \tag{5.19}$$

represents the geometry on each side of the wall and is related to the standard Einstein potential $f_E = 1 - \mu/r^{D-3} - 2\Lambda r^2/(D-1)(D-2)$. Note that $S \simeq 1 + O(\tilde{\alpha})$, so as $\tilde{\alpha} \to 0$, (5.18) reduces to

$$\begin{gathered}\frac{9}{16}\left[X - \bar{\sigma}^2 - \frac{(1-\bar{f}_E)}{R^2} - \frac{(\Delta f_E)^2}{16\bar{\sigma}^2 R^4}\right] = 0 \Rightarrow \\ \frac{\dot{R}^2}{R^2} = \frac{\bar{f}_E}{R^2} - \frac{(\Delta f_E)^2}{16R^4\bar{\sigma}^2} - \bar{\sigma}^2 + \frac{\tilde{\alpha}}{3R^4}\left\{3(\bar{f}_E - 1)^2 + \frac{(\Delta f_E)^2}{4} + 12R^2\bar{\sigma}^2(1-\bar{f}_E) + 8R^4\bar{\sigma}^4\right\}.\end{gathered} \tag{5.20}$$

Here, $\bar{f}_E \equiv (f_{E-} + f_{E+})/2$ and $\Delta f \equiv f_{E+} - f_{E-}$. We can define the effective scale of R in terms of parameters γ_e and a

$$\bar{\sigma}_e^2 = \bar{\sigma}^2(1 - 8\tilde{\alpha}\bar{\sigma}^2/3)\ , \quad \frac{1}{\ell_e^2} = \frac{2\Delta\Lambda(1-4\tilde{\alpha}\bar{\sigma}^2)}{(D-1)(D-2)}\ , \quad \gamma_e = \frac{4\bar{\sigma}_e\ell_e^2}{1+4\bar{\sigma}_e^2\ell_e^2}\ , \tag{5.21}$$

and

$$a^2 = 1 + \frac{2\Lambda_-\gamma_e^2}{(D-1)(D-2)}\left[1 - 4\tilde{\alpha}\bar{\sigma}^2 - \frac{2\Lambda_+\tilde{\alpha}}{(D-1)(D-2)}\right] \tag{5.22}$$

Now defining $\hat{R} = aR/\gamma_e$ and $\hat{\lambda} = a\lambda/\gamma_e$, the equation of motion (5.20) takes the form

$$\left(\frac{d\hat{R}}{d\hat{\lambda}}\right)^2 = 1 - \left(\hat{R} + \frac{\hat{C}}{\hat{R}^{D-2}}\right)^2 - \frac{\hat{B} - 2\hat{C}}{\hat{R}^{D-3}} \tag{5.23}$$

where

$$\begin{aligned}\hat{B} &= \left(\frac{a}{\gamma_e}\right)^{D-3}\left[\bar{\mu}\left(1 - 4\tilde{\alpha}\bar{\sigma}^2 - \frac{4\bar{\Lambda}\tilde{\alpha}}{(D-1)(D-2)}\right) + \frac{\Delta\mu}{8\bar{\sigma}_e^2\ell_e^2}\right] \\ \hat{C} &= \left(\frac{a}{\gamma_e}\right)^{D-2}\left[\frac{(\Delta\mu)(1-4\tilde{\alpha}\bar{\sigma}^2)}{4\bar{\sigma}_e} - 2\tilde{\alpha}\frac{\mu_+\mu_-\bar{\sigma}_e}{\Delta\mu}\right]\end{aligned} \tag{5.24}$$

We conclude this format is the same as for the Einstein case, although the coefficients are corrected by $\tilde{\alpha}$, thus the principle for solving the instanton equations is the same.

Since $\tilde{\alpha} = 0$ for $D = 4$, we see that the EGB equations of motion for the wall indeed reduce to the Einstein equations, as expected for a physical system. Therefore, in 4D, the motion of the wall is as the Einstein case described in [79, 80]: for a given seed mass M_+, there are a range of bubble solutions with remnant masses M_-, however, we expect a unique lowest action solution with specific mass M_- that we identify as the instanton with a remnant black hole of mass M_-.

5.2.2 Computing the instanton action

In order to identify the lowest action solution (bearing in mind that even in 4D, the GB term could contribute to the action), we must now compute the bulk and wall contributions to the action, then subtract the background action of the initial state.

The background seed action

We start by computing the action for the background solution of mass M_+, and bare vacuum energy $\propto \Lambda_+$; this is simply a matter of computing the bulk term (5.10), bearing in mind two key points. The first is that if we are in vacuum or AdS spacetime ($\Lambda_+ \leq 0$), then we must truncate our bulk integral at some finite radius that we choose to label r_c. For a positive cosmological constant, r_c will be the upper limit of integration at the cosmological horizon. The second point is that we must perform the integration at *arbitrary* Euclidean time periodicity β, hence at an event horizon, there will, in general, be a conical deficit[2], thus we must generalise the argument of [79] to include the GB term.

Computing the integrand of (5.4) for the metric (5.5) we see that, on-shell, the bulk integrand is a total derivative:

$$\sqrt{g}\left[\mathcal{R} - 2\Lambda + \alpha\mathcal{L}_{GB}\right] = -\left\{ r^{D-4} f' \left[r^2 + \frac{2(D-2)\tilde{\alpha}}{(D-4)}(1-f) \right] \right\}' . \tag{5.25}$$

Giving a contribution of $I_c - I_h$, where

$$I_c = \frac{\beta \mathcal{A}_{D-2}}{16\pi G} r_c^{D-4} f'(r_c) \left(r_c^2 + \frac{2(D-2)\tilde{\alpha}}{(D-4)}(1 - f(r_c)) \right) \tag{5.26}$$

at the upper r_c limit and at the black hole horizon

$$I_h = \frac{\beta \mathcal{A}_{D-2}}{16\pi G} \times \frac{4\pi}{\beta_h} r_h^{D-2} \left(1 + \frac{2(D-2)\tilde{\alpha}}{(D-4) r_h^2} \right) = \frac{\beta}{\beta_h} S_{BH} \tag{5.27}$$

---

[2] Although the presence of a conical deficit can be disconcerting, the singularity is mild, and can be resolved by a process analogous to the discussion of the Dirac delta-distribution (as described in the appendix of [79]). As discussed in [174], the horizon is a fixed point of the isometry of the metric – a "bolt" – which has codimension 2, hence is not a boundary of the spacetime in the strict sense.

the contribution is proportional to the entropy. Note we have replaced the derivative of f at the horizon with $f'(r_h) = 4\pi/\beta_h$, an expression involving the critical horizon periodicity β_h for which there is no conical singularity at the horizon.

We now complete the computation by taking into account possible conical defects at a horizon. Following the approach of Appendix B, we note that a conical deficit metric has the local form $d\rho^2 + \lambda^2\rho^2 d\theta^2$, where $\lambda \neq 1$ and the periodicity of θ is 2π. The deficit angle for this metric is $\delta = 2\pi(1-\lambda)$. We write the black hole metric locally at the horizon as

$$ds^2 = A^2(\rho)d\tau^2 + d\rho^2 + C^2(\rho)d\Omega^2_{D-2} \tag{5.28}$$

where $\rho^2 = 4(r-r_h)/f'(r_h)$, and $A'(0) = 2\pi/\beta_h$. Comparing this with the canonical form above ($\theta = 2\pi\tau/\beta$), we see that $\lambda = \beta/\beta_h$, hence the conical deficit is

$$\delta = 2\pi\frac{\beta_h - \beta}{\beta_h}. \tag{5.29}$$

To compute the contribution of the conical deficit to the action, we split our bulk integral into an integral from a proper distance ε from the horizon, and smooth out the cone inside ε, by having A smoothly interpolate between being regular at the origin, $A'(0) = 2\pi/\beta$, and having the black hole geometry value $A(\varepsilon) = 2\pi/\beta_h$ at $\rho = \varepsilon$. We then take the limit $\varepsilon \to 0$ to obtain the action with the conical singularity.

Computing the terms in the EGB Lagrangian for the metric (5.28):

$$\begin{aligned}\mathcal{R} &= -2\frac{A''}{A} - 2(D-2)\left(\frac{A'C'}{AC} - \frac{C''}{C}\right) + (D-2)(D-3)\frac{(1-C'^2)}{C^2}\\ \alpha\mathcal{L}_{GB} &= -4(D-2)\tilde{\alpha}\left[\frac{(1-C'^2)}{(D-4)C^2}\frac{A''}{A} + \frac{(1-C'^2)}{C^2}\left(\frac{A'C'}{AC} + \frac{C''}{C}\right)\right.\\ &\qquad\left. - (D-5)\frac{(1-C'^2)^2}{4C^4}\right]\end{aligned} \tag{5.30}$$

and using $C = r_h + O(\rho^2)$, shows that near the horizon

$$AC^{D-2}\left[\mathcal{R} - 2\Lambda + \alpha\mathcal{L}_{GB}\right] \sim -2\left(A'\left[C^{D-2} + \frac{2\tilde{\alpha}(D-2)}{(D-4)}C^{D-4}\right]\right)' + O(\rho) \tag{5.31}$$

hence

$$\begin{aligned}\int_0^{\varepsilon} d\rho A C^{D-2}\left[\mathcal{R}-2\Lambda+\alpha\mathcal{L}_{GB}\right] &= -2r_h^{D-2}\left(1+\frac{2(D-2)\tilde{\alpha}}{(D-4)r_h^2}\right)\left[A'(\varepsilon)-A'(0)\right]+O(\varepsilon^2)\\ &= -2\left(\frac{4GS_{BH}}{\mathcal{A}_{D-2}}\right)\frac{2\pi(\beta-\beta_h)}{\beta\beta_h} \end{aligned} \tag{5.32}$$

Thus the full contribution to the bulk action including the conical deficit is

$$\begin{aligned}-\int d^Dx\sqrt{g}\frac{\mathcal{L}_{EGB}}{16\pi G} &= -\lim_{\varepsilon\to 0}\frac{\beta\mathcal{A}_{D-2}}{16\pi G}\left[\int_0^{\varepsilon} AC^{D-2}\mathcal{L}_{EGB}d\rho+\int_{r_h+O(\varepsilon^2)}^{r_c} r^{D-2}\mathcal{L}_{EGB}dr\right]\\ &= \frac{(\beta-\beta_h)}{\beta_h}S_{BH}-\frac{\beta}{\beta_h}S_{BH}+I_c=I_c-S_{BH}\end{aligned} \tag{5.33}$$

The large r contribution from r_c is treated differently depending on whether $\Lambda > 0$ or not. For $\Lambda > 0$, we have a cosmological horizon, and must therefore take into account any conical deficit as described above. This procedure follows through in much the same way as for the black hole horizon, and (noting that $I_c < 0$ for the cosmological horizon) for a de Sitter seed we obtain

$$I_{seed} = -S_{CH} - S_{BH} \tag{5.34}$$

thus, just as for Einstein gravity, the action of a black hole in de Sitter space for EGB gravity is the sum of the entropies of the horizons.

If however we are in asymptotically flat or AdS spacetime =($\Lambda < 0$ or $\Lambda = 0$), we place a cut-off boundary at r_c, and compute the action at that cut-off. Strictly, this means we have to also compute a Gibbons-Hawking boundary term for the artificial boundary r_c, as well as perform a background subtraction to obtain a finite answer. However, in computing the action of the instanton, we calculate the action of the bubble geometry and subtract the action of the seed geometry; noting that the bubble and seed geometries are identical outside the bubble wall, both the contribution from the bulk integral I_c (5.26) as well as the Gibbons-Hawking term and any background subtractions will be the same. Thus we do not need to explicitly compute these large r terms and simply note that both seed and bubble geometries have an identical contribution at the large r cut-off, which we label I_C:

$$I_{seed} = I_C - S_{BH}(M_+, \Lambda_+) \tag{5.35}$$

The bubble geometry

For the bubble geometry, the main difference from the previous subsection is that we have the bubble wall at $R(\lambda)$. If R varies with λ, then the periodicity of the solution is set by the periodicity of R. The previous subsection demonstrates how to compute the bulk action, which is now composed of two parts, the interior and exterior of the bubble. Using these results, we see that the bulk contribution to the bubble action, (5.10), reduces to the boundary terms at r_h and r_c, together with a contribution evaluated at the wall:

$$\begin{aligned} I_{bulk,\mathcal{W}} = -\frac{\mathcal{A}_{D-2}}{16\pi G}\int d\lambda R^{D-4}\Big[& f'_+\dot{\tau}_+\left(R^2+\frac{2(D-2)\tilde{\alpha}}{(D-4)}(1-f_+)\right) \\ & -f'_-\dot{\tau}_-\left(R^2+(1-f_-)\right)\Big]. \end{aligned} \tag{5.36}$$

Turning to the wall integral (5.11), the trace of the Israel equations

$$(D-1)8\pi G\sigma = -(D-2)\Delta K + \frac{2\tilde{\alpha}}{(D-3)}\left[\mathcal{G}_{ab}\Delta K^{ab} - \Delta\mathcal{J}\right] \tag{5.37}$$

gives the wall integral as

$$I_{\mathcal{W}} = \frac{\mathcal{A}_{D-2}}{8\pi G}\int d\lambda \frac{R^{D-2}}{(D-1)}\left(\Delta K - \frac{6\tilde{\alpha}}{(D-3)(D-4)}\left[2\mathcal{G}_{ab}\Delta K^{ab} - \Delta\mathcal{J}\right]\right). \tag{5.38}$$

It then proves useful to define

$$K_0 = K_{\lambda\lambda} = \frac{f'-2\ddot{R}}{2f\dot{\tau}}\,, \qquad K_1 = \frac{f\dot{\tau}}{R}\,, \qquad p_0 = \frac{(1-\dot{R}^2)}{2R^2}\,, \qquad p_1 = \frac{\ddot{R}}{R} \tag{5.39}$$

here, K_1 is the angular part of the extrinsic curvature, and p_0, p_1 appear in the intrinsic Einstein tensor. The Israel conditions then give the following relation between the timelike and spacelike extrinsic curvature differentials:

$$\Delta K_1 = \Delta K_0 + 2\tilde{\alpha}\left[2p_0\Delta K_0 - 2p_1\Delta K_1 - \Delta(K_0K_1^2) + \Delta K_1^3 - 6p_0\Delta K_0\right]. \tag{5.40}$$

Using these relations, after some algebra we find the wall integral can be reduced to

$$\begin{aligned} I_{\mathcal{W}} &= \frac{\mathcal{A}_{D-2}}{8\pi G}\int d\lambda R^{D-2}\left[\Delta K_0 + \frac{2(D-2)\tilde{\alpha}}{(D-4)}\left(2p_0\Delta K_0 - 2p_1\Delta K_1 - \Delta(K_0K_1^2)\right)\right] \\ &= \frac{\mathcal{A}_{D-2}}{8\pi G}\int d\lambda R^{D-2}\Delta\left[K_0\left(1+\frac{2(D-2)\tilde{\alpha}(1-f)}{(D-4)R^2}\right) - \frac{4(D-2)\tilde{\alpha}}{(D-4)}\frac{\ddot{R}}{R}K_1\right]. \end{aligned} \tag{5.41}$$

Noting that

$$\frac{f'\dot{\tau}}{2} = \dot{\tau}\left(f\dot{\tau}K_0 + \ddot{R}\right) = \left(1-\frac{\dot{R}^2}{f}\right)K_0 + \dot{\tau}\ddot{R}, \tag{5.42}$$

we find that the combined bulk-term and wall integrals give

$$\begin{aligned} I_{wall} =& \frac{\mathcal{A}_{D-2}}{8\pi G}\int d\lambda R^{D-2}\Delta\left[-\frac{4(D-2)\tilde{\alpha}}{(D-4)}\frac{\ddot{R}}{R}K_1\right. \\ &\left.+\left(\frac{\dot{R}^2}{f}K_0 - \dot{\tau}\ddot{R}\right)\left(1+\frac{2(D-2)\tilde{\alpha}(1-f)}{(D-4)R^2}\right)\right]. \end{aligned} \tag{5.43}$$

Putting together, we see that the action of the bubble geometry is

$$I_{bubble} = I_{wall} + I_C - S_{BH}(M_-) \tag{5.44}$$

hence the action for the tunnelling instanton is

$$I_{\mathcal{B}} = I_{bubble} - I_{seed} = S_{BH}(M_+) - S_{BH}(M_-) + I_{wall}. \tag{5.45}$$

Therefore, we have shown that the amplitude for vacuum decay including the higher derivative GB term in arbitrary dimensions has the same form as the decay rate computed for vacuum decay in Einstein gravity in 4D. While we leave the numerical evaluation of this action for arbitrary M_+ and M_- for future study, we note that the contribution from the wall integral vanishes for static instantons, which are the relevant instantons for Higgs vacuum decay [81, 82].

The central result of this section is therefore that, as with Einstein gravity, the probability of decay seeded by a black hole in EGB gravity is simply the difference in entropy of the seed and remnant black holes:

$$\mathcal{P} \sim \exp\left[-(S_{seed} - S_{remnant})/\hbar\right] \tag{5.46}$$

5.3 The Hawking-Moss Instanton

In the previous section, we derived the bounce action as the difference in entropies between the cosmological and event horizons. However, as we mention in Chapter 3, there is another decay channel of an up-tunnelling transition – the Hawking Moss transition.

To see the impact of the GB term on the BHHM transition, we first change the notation in (5.8) and (5.9) of "$f_\pm$" to "$f_{F/T}$" to correspond to the labellings of the false vacuum (F) and the top of the potential (T). These will be characterised by mass parameters $\mu_{F/T}$, and vacuum parameters $\ell_{F/T}$, where $\ell^2 = (D-1)(D-2)/2\Lambda$. The tunnelling rate is dominated by the Boltzmann factor, as shown in (3.69). From (5.46), we see that the change in action is the difference in the entropies, justifying the interpretation of the HM probability as a Boltzmann suppression

$$B_{FV\to Top} = I_T - I_F = [S_{CH} + S_{BH}]_F - [S_{CH} + S_{BH}]_T. \tag{5.47}$$

Thus, the form of the BHHM action is the same as for Einstein gravity, however the entropies in the expressions are now determined by the EGB formula [163]:

$$S_i = \frac{\mathcal{A}_{D-2}}{4G} r_i^{D-2} \left(1 + \frac{2(D-2)\tilde{\alpha}}{(D-4)r_i^2}\right) \tag{5.48}$$

where the subscript i corresponds to the black hole or cosmological event horizon radius, which in general is also modified by the GB term.

The likelihood of the BHHM instanton is obviously dependent on the details of the seed black hole and the dimension of the spacetime, but some general trends can be noted. For example, when a black hole is introduced, the total entropy drops (though note the exception we will discuss for 5D presently), thus for a given seed mass the BHHM transition will always prefer to jump to a pure de Sitter configuration, as this will maximise the negative contribution to the action. Similarly, introducing a seed black hole will also lower the action, since the overall entropy in the false vacuum will drop. Thus, just as with Einstein gravity, we expect that introducing seed black holes will also catalyse the HM transition.

There is a limit however to how far we can drop the action, and this is determined by the *Cosmological Area Principle* [86], that the area of the cosmological horizon must never increase:

$$S_c|_T \leq S_c|_F \tag{5.49}$$

As we saturate this bound, the HM action becomes the difference in entropy of the seed and remnant black holes. Thus, we get broadly the same picture as for the Einstein case, where the preferred instanton (the one with the lowest action) is a jump to a pure vacuum solution at the higher vacuum energy (i.e. no remnant black hole) for lower seed masses. As the seed mass increases, we hit the Cosmological Area Bound and the transition is to a black hole geometry with the "top" vacuum energy (see Figs. 5.1, 5.2).

Therefore, broadly speaking the picture for the BHHM decay process looks qualitatively very similar for the EGB case as for the pure Einstein case across arbitrary dimensions with one interesting exception. Solving $f(r_h) = 0$ for the black hole horizon at r_h yields the following expression for the mass:

$$M = \frac{(D-2)\mathcal{A}_{D-2}}{16\pi G}\mu = \frac{(D-2)\mathcal{A}_{D-2} r_h^{D-5}}{16\pi G}\left(\tilde{\alpha} + r_h^2 - \frac{r_h^4}{\ell^2}\right). \tag{5.50}$$

For $D = 5$, we see that while smaller black hole horizons correspond to lower black hole masses, it is not possible for $M \to 0$ while maintaining a horizon. Indeed, inspecting the expression for $f(r)$ at the origin for $D = 5$ yields $f(0) = 1 - \sqrt{\mu/\tilde{\alpha}}$, which becomes positive as μ, hence M, becomes sufficiently small: $GM < 3\pi\alpha/4$, indicating the loss of a horizon. This is consistent with numerical studies of collapse [175, 176], which find that black holes will not form dynamically if the total mass-energy content of the spacetime is below a critical value in both asymptotically flat and asymptotically AdS spacetime. This *mass gap* was also noted in [177] in an exploration of black hole formation during gravitational collapse, and differences in thermodynamic phenomenology and gravitational collapse with GB corrections between five and higher dimensions were noted in [178, 179]. Thus, the picture of the HM transition will be distinctive in 5 dimensions. We, therefore, present results for $D = 5$ separately and present the HM results for $D = 6$ as representative of higher dimensions.

- 5D HM

Taking $f(r_h, r_c) = 0$ and $D = 5$ in (5.6) (noting $\tilde{\alpha} = 2\alpha$ in 5D) the black hole and cosmological event horizons can be obtained in a simple form:

$$r_h = \left(\frac{\ell^2}{2} - \sqrt{2\alpha\ell^2 + \frac{\ell^4}{4} - \frac{8GM\ell^2}{3\pi}}\right)^{\frac{1}{2}}, \quad r_c = \left(\frac{\ell^2}{2} + \sqrt{2\alpha\ell^2 + \frac{\ell^4}{4} - \frac{8GM\ell^2}{3\pi}}\right)^{\frac{1}{2}} \tag{5.51}$$

Recall that $M_{crit} = 3G\pi\alpha/4$, is the critical minimum mass that allows for an event horizon to exist, and the Nariai mass, M_N, where the black hole and cosmological horizons merge [180, 181] gives a maximum:

$$GM_N = \frac{3\pi}{32}\left(\ell^2 + 8\alpha\right). \tag{5.52}$$

Any solution with a mass parameter larger than M_N will not have the correct signature, hence is considered unphysical, thus all EGB *black hole* solutions in $5D$ must satisfy $M_{crit} \leq M \leq M_N$. Solutions with $M < M_{crit}$ have no event horizon, but an examination of the geometry near $r = 0$ shows that there is a solid angular deficit at the origin, which can be regularised by a similar method to the conical deficit regularisation, which allows one to integrate the Euclidean action, resulting in no additional contribution. The space of massive particle solutions in 5D EGB can therefore be thought of as analogous to AdS solutions in 3D Einstein gravity, where there is a finite range of masses for which the particle is a conical deficit, above which the solution becomes a BTZ black hole [182, 183].

We depict the constraints on the black hole mass parameter in Fig. 5.1 by plotting the ratio of the BHHM instanton action to the pure HM instanton action, B/B_{HM}, as a function of the seed black hole mass, M_F/M_N. Here, B_{HM} denotes the pure HM instanton without seed or remnant black holes, which only depends on the scale parameters of the initial and final states. The blue solid lines represent different remnant black hole masses, ranging from $0.2M_N$ to M_N in increments of $0.2M_N$ from lower to higher, while the cyan line on the bottom represents a transition with no remnant black hole. The black line shows the lowest mass when a black hole horizon can exist. As with the Einstein case, the BHHM action increases with the remnant mass, indicating larger remnant black holes slow down the transition. Two vertical dashed lines denote the lower and upper bounds of the seed mass for a black hole, which are constrained by mass gap and Nariai limits respectively. The red curve shows the limiting constraint of the cosmological area conjecture. In all cases, the Nariai limit is an upper bound on the seed mass.

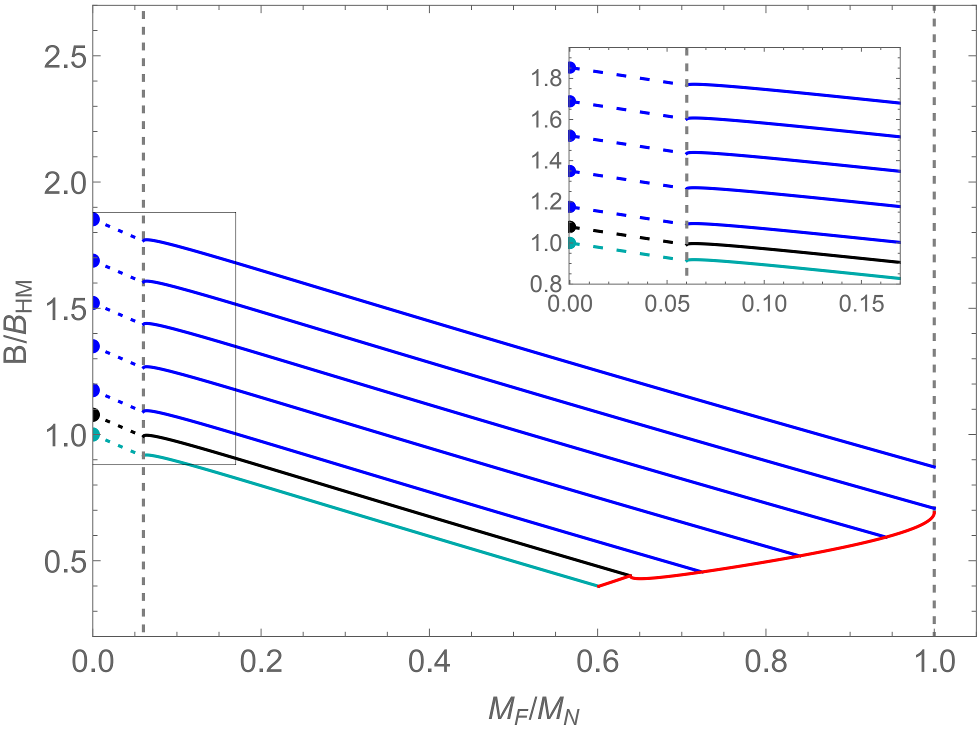

Fig. 5.1 The ratios of tunnelling components B/B_{HM} change with the seed black hole mass in 5D spacetime, M_F/M_N, for fixed values of $\ell_F = 5$, $\ell_T = 4.5$, and $\alpha = 0.2$ where the relative mass gap is $M_C \approx 0.06M_N$. The blue solid lines represent remnant black hole masses ranging from lower to higher as “$0.2M_N$, $0.4M_N$, $0.6M_N$, $0.8M_N$, M_N", respectively; while the black solid line represents a remnant critical mass M_{crit}. The vertical dashed lines indicate the lower and upper bounds of the seed black hole mass. The red curve corresponds to the cosmological equal area limit. The cyan line represents a transition to a final de Sitter state without a remnant black hole, while the dots on the left axis show the transitions from pure de Sitter to remnant masses. The dashed lines on the left part of the graph, and the inset, represent a seed mass below the mass gap.

On the left hand side of Fig. 5.1, the dashed lines indicate the region where the seed mass is smaller than M_{crit}, hence there is no black hole horizon. There is still a mass at the origin however, and the cosmological horizon area is reduced as a result of the seed mass parameter, and linearly approaches the pure de Sitter area as $M \to 0$. Note that as M increases from M_{crit}, there is a small uptick in the action, reflected in the detail of the inset. This is due to the dependence of the entropies on $\Delta M = M - M_{crit}$. The black hole horizon entropy $S_{BH} \propto \sqrt{\Delta M}$, whereas $S_{CH} \sim S_{DS} - O(\Delta M)$, thus the overall entropy of the seed actually (temporarily) *increases* as a result of adding mass to the system. Meanwhile, at the lower part of the plot along the red equal area line, the same phenomenon occurs, only this time causing a small downtick as the action of the remnant increases as the mass creeps above M_{crit}.

- 6D HM

Following the same procedure, Fig. 5.2 displays the ratio B/B_{HM} as a function of seed black hole mass, M_F, for different remnant black hole masses, M_T, in $6D$. Unlike in $5D$ there is no mass gap, and only the Nariai limit sets an upper bound on the size of black holes. As before, the cosmological area conjecture gives a cut-off on the allowed parameter space.

In Fig. 5.2, we see a plot qualitatively the same as for the Einstein BHHM transitions: the action decreases as the seed mass increases, with the jump to a pure de Sitter spacetime at the top of the potential shown in cyan. The cosmological area conjecture provides a cutoff at larger seed masses, shown in red, where the transition now leaves a remnant black hole. The generic BHHM transition with both seed and remnant is shown in blue, where the remnant mass along a blue line is constant. The solid dots at the left depict the transition from pure de Sitter spacetime to a spacetime with a remnant black hole, especially, the cyan dot is the original HM transition.

5.4 Higher dimensions

In higher dimensions, the GB parameter will modify the wall trajectory, as well as the action, so in order to extract the impact of the GB correction, we will explore how the critical static bubble is impacted by the GB term. The critical static bubble is the instanton with the lowest action for a given wall tension σ. It connects the modified CDL branch,

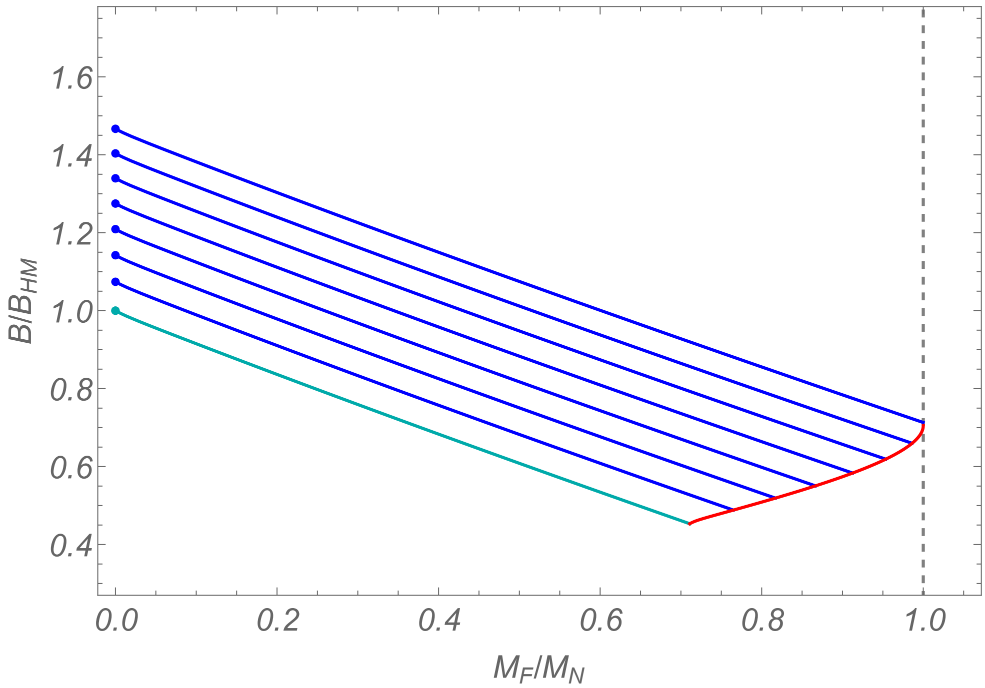

Fig. 5.2 The ratios of tunnelling exponents B/B_{HM} as a function of seed mass in 6D spacetime, M_F/M_N, shown for parameter values $\ell_F = 5, \ell_T = 4.5$ and $\alpha = 0.2$. The dashed vertical line marks the Nariai limit for the seed mass. Blue solid lines represent different remnant black hole masses, ranging from $0.1M_N$ to $0.7M_N$ with steps of $0.1M_N$ from lower to higher. The red curve gives the equal horizon area constraint. The cyan line represents a transition from a seed black hole to pure de Sitter spacetime. The dots represent a transition from pure de Sitter spacetime to a spacetime with a remnant black hole.

which represents the preferred instanton at very low seed masses where the interior of the bubble has no black hole to the static branch, where there is both a seed and remnant black hole; the critical instanton is, therefore, static, but has no remnant, and the seed mass is fully determined by the vacuum energies and wall tension.

For simplicity, we will explore tunnelling from a positive vacuum energy with seed black hole to the Minkowski vacuum. Therefore, $\Delta\mu = \mu_+ = 2\bar{\mu}$, and $\Delta\Lambda = \Lambda_+ = 2\bar{\Lambda}$. Thus, $a = 1$, and the parameters in (5.24) simplify to

$$\hat{B} = \frac{\mu_+(1-4\tilde{\alpha}\bar{\sigma}^{-2})}{2\bar{\sigma}_e\gamma_e^{D-2}} = 2\hat{C} \tag{5.53}$$

thus the static instanton constraints read

$$\begin{aligned} 1 &= \left(\hat{R} + \frac{\hat{C}}{\hat{R}^{D-2}}\right)^2 \\ 0 &= 2\left(\hat{R} + \frac{\hat{C}}{\hat{R}^{D-2}}\right)\left(1 - (D-2)\frac{\hat{C}}{\hat{R}^{D-1}}\right) \end{aligned} \tag{5.54}$$

identical in form to the Einstein case. These are solved by

$$\hat{C} = \frac{(D-2)^{D-2}}{(D-1)^{D-1}} \quad ; \qquad \hat{R} = \frac{(D-2)}{(D-1)} \tag{5.55}$$

hence

$$\mu_{crit} = \frac{4\bar{\sigma}_e \gamma_e^{D-2}}{(1-4\tilde{\alpha}\bar{\sigma}^2)} \frac{(D-2)^{D-2}}{(D-1)^{D-1}} \tag{5.56}$$

from which one can see that the critical instanton seed mass increases with $\tilde{\alpha}$ by expanding the expressions for the effective parameters $\bar{\sigma}_e, \gamma_e$:

$$\frac{\delta\mu_{crit}}{\mu_0} = \frac{8}{3}\tilde{\alpha}\bar{\sigma}^2 \left[1 + (D-2)(1-2\bar{\sigma}\gamma_0)\right] \tag{5.57}$$

where the subscript ‘0’ indicates the values of the various functions at $\tilde{\alpha} = 0$, and μ_0 is the critical mass at $\tilde{\alpha} = 0$:

$$\mu_0 = \frac{(4\bar{\sigma}\ell_0)^{D-1}\ell_0^{D-3}}{(1+4\bar{\sigma}^2\ell_0^2)^{D-2}} \frac{(D-2)^{D-2}}{(D-1)^{D-1}} \tag{5.58}$$

However, the instanton action is determined by the entropy of the seed mass, which in turn is determined by the horizon radius, which actually *decreases* as $\tilde{\alpha}$ is switched on. Thus the actual incremental change in the action is a combination of these effects, and further complicated by the nature of the polynomial determining the horizon in the various dimensions. Computing the incremental change in the horizon radius and critical mass, we arrive at an expression for the entropy shift at small $\tilde{\alpha} \lesssim \mu_0^{2/(D-3)}$:

$$\frac{\delta S}{S_0} = \frac{(D-2)\tilde{\alpha}}{r_0^3 f_E'(r_0)} \left(\frac{2r_0 f_E'(r_0)}{(D-4)} + \frac{8\mu_0\bar{\sigma}^2}{3r_0^{D-5}} \left[1 + (D-2)(1-2\bar{\sigma}\gamma_0)\right] - 1 \right) \tag{5.59}$$

The shift in entropy is proportional to $\tilde{\alpha}$ as expected; the other key dependence is on $\bar{\sigma}\ell_0$, which in turn feeds into μ_0. As discussed in [80], $2\bar{\sigma}\gamma_0 < 1$, hence the critical mass becomes very strongly damped for low $\bar{\sigma}\ell$ at large D, hence the range of $\tilde{\alpha}$ for which (5.59) is relevant becomes small. This is reflected in the range for $\tilde{\alpha}\ell_0^2$ in Fig. 5.3 and Fig. 5.4

Exploring the entropy change (5.59) for various D shows that the shift in entropy with $\tilde{\alpha}$ is positive. Thus, the GB term lowers the tunnelling amplitude for positive α. The picture for $5D$ is more nuanced however. In 5D, the horizon radius can be simply found as

$$r_h = \frac{\ell_0}{\sqrt{2}}\left(1 - \sqrt{1 + \frac{4(\tilde{\alpha}-\mu)}{\ell_0^2}}\right)^{1/2} \tag{5.60}$$

Clearly, $r_h \to 0$ as $\mu \to \tilde{\alpha}$, i.e. at finite values of μ_{crit} hence $\bar{\sigma}$, and there is no horizon for $\mu < \tilde{\alpha}$. This corresponds to the interesting "mass gap" in the 5DGB black hole, as we introduced before. Spacetimes with $\mu < \tilde{\alpha}$, i.e. mass below $3\pi\alpha/4G$, do not have a horizon but instead have a solid angle deficit as $r \to 0$. This makes 5D crucially different from higher dimensions, in that while the entropy of the seed does initially increase with $\tilde{\alpha}$, for low $\bar{\sigma}\ell_0$ we see that the entropy function (calculated exactly, rather than using (5.59)) turns over and decreases, eventually dropping to zero as this mass limit is hit. We therefore expect that the semi-classical approximation should not be valid for small seed black holes.

In Fig. 5.3 and Fig. 5.4, we show the variation in entropy of the seed black hole (which directly translates into the instanton action) as $\tilde{\alpha}$ is switched on for both 5 and 6 dimensions. Although the generic picture is that the entropy increases as $\tilde{\alpha}$ increases, the one exception is for $D = 5$ and smaller $\bar{\sigma}$. As discussed above, caution should be used in pushing to too low $\bar{\sigma}$.

5.5 Four dimensions

Having derived results for vacuum decay with higher derivative gravity in general dimensions, we now restrict to $D = 4$ to explore whether there is an impact from the modification of the action – we have already confirmed that the bubble solutions are identical to Einstein gravity as expected in Sec. 5.2, therefore it only remains to compute the effect of the GB term on the action.

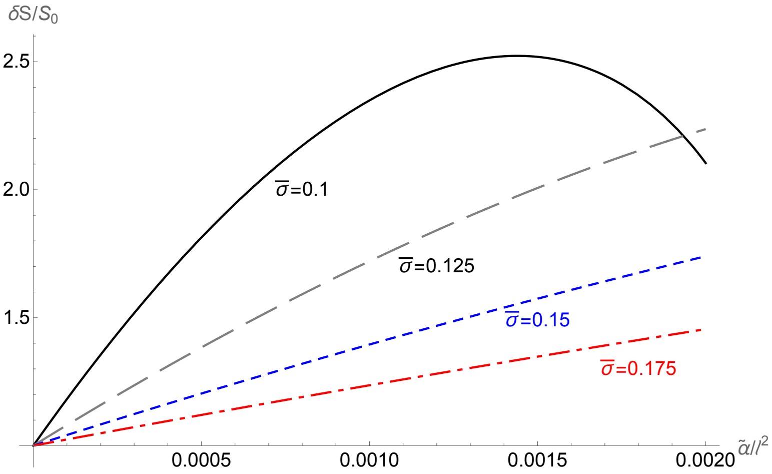

Fig. 5.3 The shift in entropy of the critical instanton in 5D as a function of $\tilde{\alpha}/\ell^2$ for the given bubble wall tensions indicated, $\bar{\sigma} = 0.1, 0.125, 0.15, 0.175$, respectively.

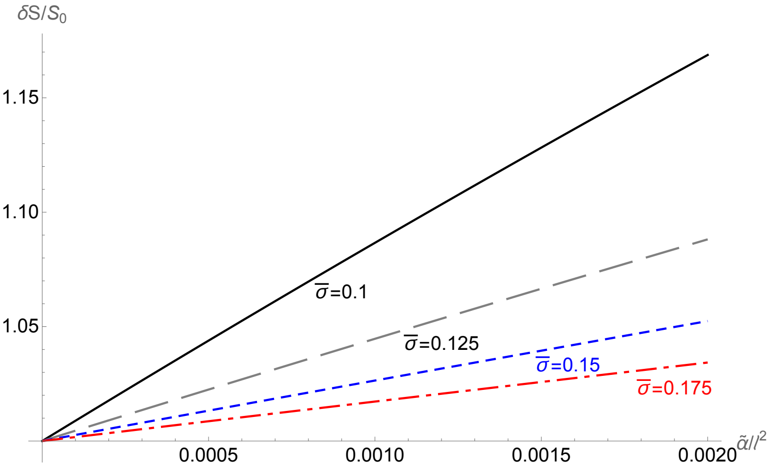

Fig. 5.4 The shift in entropy of the critical instanton in 6D as a function of $\tilde{\alpha}/\ell^2$ for the given bubble wall tensions indicated, $\bar{\sigma} = 0.1, 0.125, 0.15, 0.175$, respectively.

5.5.1 Bubble nucleated vacuum transitions

Recall that the general instanton is (Euclidean) time-dependent and has both seed and remnant black holes with action given by (5.45) and the equation of motion:

$$\begin{aligned}\dot{R}^2 &= 1 - \left(\bar{\sigma}^2 + \frac{\bar{\Lambda}}{3} + \frac{(\Delta\Lambda)^2}{144\bar{\sigma}^2}\right)R^2 - \frac{2G}{R}\left(\bar{M} + \frac{\Delta M \Delta\Lambda}{24\bar{\sigma}^2}\right) - \frac{(G\Delta M)^2}{4\bar{\sigma}^2 R^4} \\ &= f_\pm - \left(\omega_\pm R + \frac{\Delta M}{2\bar{\sigma} R^2}\right)^2 = F(R)\end{aligned} \tag{5.61}$$

where

$$\omega_{\pm} = \frac{\Delta\Lambda}{12\bar{\sigma}} \mp \bar{\sigma} \tag{5.62}$$

and $f_{\pm} = 1 - 2M_{\pm}/r - \Lambda_{\pm} r^2/3$ is the Schwarzschild potential.

First, note that it is not possible to nucleate a bubble with a remnant black hole unless there is a seed. To see this, note that (5.61) implies that

$$f_+ \dot{\tau}_+ = \omega_+ R + \frac{\Delta M}{2\bar{\sigma} R^2} \geq 0 \tag{5.63}$$

If we have no black hole seed, then $f_+ = 1 - \Lambda_+ r^2/3$, and $\Delta M = -M_-$. The equation of motion, $\dot{R}^2 = F(R)$, must have two zeros of $F(R)$ (unless the solution is static, $F(R) \equiv 0$). However,

$$F'(R) = f'_+ - 2\left(\omega_+ R + \tfrac{\Delta M}{2\bar{\sigma} R^2}\right)\left(\omega_+ - \tfrac{\Delta M}{\bar{\sigma} R^3}\right) = -\tfrac{2\Lambda R}{3} - 2(f_+ \dot{\tau}_+)\left(\omega_+ + \tfrac{M_-}{\bar{\sigma} R^3}\right) < 0 \tag{5.64}$$

hence $F(R)$ is a monotonically decreasing function of R and cannot have two zeros. We therefore conclude that vacuum decay by bubble nucleation either is a CDL bubble, or is seeded decay with an initial seed black hole, which will nucleate a bubble that may, or may not, have a remnant black hole.

Turning to the computation of the action for the bubble, there are two parts: the difference in black hole entropies, and the contribution from the bubble wall, which is not obviously vanishing. Dealing with this latter term, the α dependent part of the contribution is $I_{wall,\alpha} = I^+_{\mathcal{W},\alpha} - I^-_{\mathcal{W},\alpha}$, where

$$I^{\pm}_{\mathcal{W},\alpha} = \frac{2\alpha}{G} \int d\lambda \left[\left(K_0^{\pm} - \frac{f'_{\pm} \dot{\tau}_{\pm}}{2} \right)(1 - f) - 2R\ddot{R} K_1^{\pm} \right] \tag{5.65}$$

Here, $K_{0,1}$ were defined in (5.39), and for the wall trajectory (5.61) are

$$K_0^{(\pm)} = \omega_{\pm} - \frac{\Delta M}{\bar{\sigma} R^3} \quad , \qquad K_1^{(\pm)} = \omega_{\pm} + \frac{\Delta M}{2\bar{\sigma} R^3} \tag{5.66}$$

we therefore see that the α contribution to the wall action is:

$$\begin{aligned} I^{\pm}_{\mathcal{W},\alpha} &= \frac{2\alpha}{G}\int d\lambda \left[\left(K_0^{\pm} - \frac{f'_{\pm}\dot{\tau}_{\pm}}{2} \right)(1-f) - 2R\ddot{R}K_1^{\pm} \right] \\ &= \frac{2\alpha}{G}\int d\lambda \left[\frac{K_0^{\pm}\dot{R}^2 - R\ddot{R}K_1^{\pm}}{f_{\pm}} - K_0^{\pm}\dot{R}^2 - R\ddot{R}K_1^{\pm} \right] \\ &= \frac{2\alpha}{G}\int d\lambda \left[\frac{\dot{R}^2}{f_{\pm}}\frac{d}{d\lambda}\left(\frac{\omega_{\pm}R}{\dot{R}} + \frac{\Delta M}{2\bar{\sigma}\dot{R}R^2} \right) - \omega_{\pm}\frac{d(R\dot{R})}{d\lambda} + \frac{\Delta M}{2\bar{\sigma}R^3}(2\dot{R}^2 - R\ddot{R}) \right] \end{aligned} \tag{5.67}$$

But now we note that the middle term vanishes due to the periodicity of R, the final term is the same on each side of the wall which will therefore cancel. Turning to the first term, this can be rewritten using the equation of motion for the wall:

$$\frac{\omega_{\pm}R}{\dot{R}} + \frac{\Delta M}{2\bar{\sigma}\dot{R}R^2} = \frac{\sqrt{f_{\pm} - \dot{R}^2}}{\dot{R}} = \mathrm{sign}(\dot{R})\sqrt{\frac{f_{\pm}}{\dot{R}^2} - 1} \tag{5.68}$$

thus the first part of the integral in (5.67) becomes:

$$\int \mathrm{sign}(\dot{R})\frac{\dot{R}^2}{f_{\pm}}\frac{d}{d\lambda}\left(\sqrt{\frac{f_{\pm}}{\dot{R}^2} - 1} \right) d\lambda = \int \mathrm{sign}(\dot{R})\arctan\left(\sqrt{\frac{f_{\pm}}{\dot{R}^2} - 1} \right) d\lambda \tag{5.69}$$

due to the periodicity of the solution $R(\lambda)$, the arctan function is symmetric around the turning points of the solution, whereas $\dot{R}$ changes sign, thus this integral vanishes and there is no α dependent contribution from the wall.

Examining the contribution of the entropies to the action reveals the presence of an $\alpha-$dependent, but constant, contribution from each black hole horizon in (5.45). The entropy term, S_{BH} is

$$S_{BH} = \frac{\pi r_+^2}{G}\left(1 + \frac{4\alpha}{r_+^2} \right). \tag{5.70}$$

From the perspective of black hole thermodynamics, this constant shift is irrelevant [184], but for our action, it is potentially important. If we have both a seed and remnant black hole, these constant terms will cancel, but if we have a seed black hole that is wiped out by bubble nucleation, then there will be a residual α term in action.

We therefore arrive at the result that the bubble action in 4D is identical to the Einstein action if there is either *both* a seed and remnant black hole or *neither* a seed nor remnant black hole. However, if we have a seed black hole and no remnant, then the GB term leaves an imprint on the action:

$$I_{\mathcal{B},NR} = \frac{\pi r_+^2}{G} + \frac{4\pi\alpha}{G} + I_{wall} \tag{5.71}$$

Thus, for bubble nucleated decay, the GB term either has no impact or actually suppresses tunnelling ($I_{\mathcal{B}}$ is increased for positive α), in the case that the decay removes the black hole altogether. This is perhaps not surprising, once one considers the fact that the GB term is a topological invariant in 4D, thus it should only impact on topology changing transitions. Perhaps more surprising is that the GB term inhibits topology changing decay.

5.5.2 Hawking-Moss Tunnelling

Armed with the results of the previous subsection, we can now easily deduce how the GB term impacts 4D HM transitions. If there is no topology change, there is no change in the action: i.e. for the pure HM instanton and for a transition with a seed black hole to a remnant black hole geometry, which corresponds to the (red) Cosmological Area Principle boundary. However, for the HM transitions that jump from a Schwarzschild de Sitter (SdS) spacetime to a pure de Sitter spacetime, there is an $\alpha-$dependent contribution that suppresses this topology changing transition. We have the bizarre situation that the universe preferentially jumps to an SdS solution with a vanishingly small mass – this will have the same topology as the initial SdS state, but the tiny black hole will presumably instantaneously evaporate leaving effectively pure de Sitter at the top of the potential. Whether or not such a Planckian sized black hole should be included in a semi-classical description is a very good question! Finally, unlike the bubble nucleation, it is possible for a HM transition to occur from pure de Sitter false vacuum to an SdS spacetime at the top of the potential. For these (topology changing) configurations the action is now lowered by $\delta I \sim 4\alpha/G - 2\pi\ell M$ relative to the pure HM transition, thus again there is a preferred transition to a vanishingly small mass black hole universe.

5.6 Summary

We studied the impact of higher order terms in the gravitational action, focusing on the Gauss-Bonnet invariant to maintain well-posedness of the equations of motion. We considered both first order, tunnelling, vacuum decay transitions as well as Hawking-Moss jumps. For bubble nucleation, we derived the general equations of motion for a bubble, including the GB term in arbitrary dimension, and found that the general result of [79], that larger black holes catalysed a static instanton with the action determined by the entropy difference between the seed and remnant black hole remains true with the GB term, and in all dimensions. The HM transitions were algebraically easier to explore, with results qualitatively similar to the Einstein process.

In 4D, the fact that the GB term is a topological invariant means that it will not impact on instantons that have both seed and remnant black holes, however, when there is a transition from a seed black hole with no remnant, the GB term suppresses the transition (for positive α). For a situation with no seed black hole, only the HM transition can result in a geometry with a remnant black hole, and here the GB term enhances the decay, although the lack of continuity of the action as a function of black hole mass means that an arbitrarily small mass black hole would have the lowest action, likely taking the spacetime outside of the semi-classical regime. The special case of 5D, with its mass gap for $\alpha > 0$, led to some interesting additional features in the transition amplitudes, and this case may merit further examination.

In general, what we have learned is that Lovelock terms appear to give a very similar picture to the black hole catalysed decay as the Einstein case, albeit with greatly more convoluted algebra!

Chapter 6

Scattering by dirty black holes

The other work in this thesis explores the quantum effects of black holes from a different aspect, specifically the scattering and absorption of black holes. In essence, black holes can act like media that affect the scattering of waves with a non-constant index of refraction, in which the curvature of spacetime not only changes the boundary conditions but also enters the equations describing the propagation of the various wave fields. We are interested in the scattering problems involving dirty black holes in this chapter. We use natural units ($c = G = \hbar = 1$) in this chapter.

This chapter is based on the article *Regge pole description of scattering by dirty black holes* published in Physical Review D [185], in collaboration with Theo Torres, Mohamed Ould El Hadj and Ruth Gregory.

6.1 Introduction

The absorption/scattering problem in geometric optics is a very appealing natural phenomenon. Sunlight is reflected and refracted by water droplets, creating rainbows and glories[1] in the sky at a particular angle. Physically, it is a complex phenomenon involving various aspects of scattering. Similar phenomena have been observed in numerous physical systems, such as atoms, molecules, and nuclei. In addition, physicists and cosmol-

---

[1] Rainbow and glory are optical phenomena caused by the interaction of light with water droplets. Rainbow arises from the refraction and reflection of light, resulting in a semicircular arc in the sky. Glory occurs when light is scattered nearly in the backward direction, resembling a concentric rainbow halo around the shadow of the observer's head.

ogists have a broad interest in investigating its counterpart with massive objects. Among these massive objects, a particular interest was put on the absorption and scattering of planar waves that impinge upon black holes in vacuum [186]. The topic has become more popular in recent years as it shares features with phenomenological observations, like the scattering of light by black holes that may form a shadow, that resulted in the first pictures of black holes [13]. The absorption/scattering problem has been extensively investigated in many black hole scenarios, such as isolated Schwarzschild [187, 188], Reissner-Nordström [189, 190], and Kerr black holes [191]. We extend the study to black holes with surrounding matter, known as a *dirty black hole*, as introduced in Chapter 2.4.2.

Studies of black holes surrounded by matter have focused on two directions: i) the environmental impact on the inspirals of compact objects [52, 192, 193] and ii) the ringdown emission [194–196]. The consensus on the latter was that while the resonance spectrum of black holes surrounded with extra structures could be widely different from that of isolated black holes, the modifications were somehow irrelevant for practical considerations and could not be seen. Interestingly, this conclusion is being revisited with the recent identification and characterisation of the so-called quasinormal mode (QNM) spectral instability [197, 198].

In the present study, we consider the particular simple model where a DBH is surrounded by a spherical thin-shell. Surprisingly and despite the many prospects offered by gravitational wave astronomy, the QNM of DBHs has received very limited attention. Generic properties of the QNM spectrum were discussed in [199, 200] and the concrete case of a DBH was considered by Leung et al. [201, 202]. In their study, Leung et al. adopted a perturbative approach which allowed for an analytical investigation but restricted their conclusion to DBH spacetimes where the shell had a limited impact. Similar DBH configurations (that is, with the shell having a limited impact on the scattering) were investigated recently and the impact of the shell on both the absorption and scattering cross section were computed [203, 204].

These recent studies, as well as the need for concrete resonance calculations beyond the perturbative regime are the main motivations for this study. There are two main goals of this paper: First, to investigate wave scattering by DBHs beyond the perturbative cases found in the literature. We therefore consider physical DBH configurations where the shell has a substantial effect on the scattering of waves, leaving an imprint on measurable quantities. Second, to compute the spectrum of resonances of DBHs from the Regge pole (RP) paradigm. RPs and the associated complex angular momentum (CAM) technique are the counterparts to QNMs. While QNMs have a real angular momentum and a complex frequency, the RPs have a real frequency and a complex angular momentum. This paradigm allows for a different interpretation of resonances in a system. The RP and CAM approaches have shed new light on many different domains of physics involving resonant scattering theory, notably in quantum mechanics, electromagnetism, optics, nuclear physics, seismology and high-energy physics (see, for example, [205–216] and references therein), and have been successfully extended to black hole physics [217–223]. As an illustration of the power of the CAM approach, we note that it provides a unifying framework describing the glory and orbiting effects of black hole scattering [222, 223].

6.2 Dirty Black Hole spacetime

We review the derivation of the DBH spacetime and show that the static configurations are fully characterized by the mass of the thin shell and its equation of state in this section. We first briefly review the Israel formalism [68] applied to our case where there are two distinct Schwarzschild geometries:

$$ds^2 = f_\pm(r)dt_\pm^2 - \frac{dr^2}{f_\pm(r)} - r^2 d\Omega^2 \tag{6.1}$$

where $d\Omega^2 = d\theta^2 + \sin^2\theta d\phi^2$ is the line element on a unit sphere, $f_\pm(r) = 1 - 2M_\pm/r$ is the Schwarzschild potential for each side of the shell, and we have already applied the knowledge that the shell is at a given radius $r = R_s(\tau)$, which implies that the angular and radial coordinates are the same on each side. At this point, we are not assuming the wall is static, hence there is a different local time coordinate on each side of the shell, which has, in general, a time dependent trajectory given by $(t_\pm(\tau), R_s(\tau))$ with τ the proper time on the shell: $f_\pm \dot{t}_\pm^2 - \dot{R}_s^2/f_\pm = 1$.

The Israel junction conditions are

$$\Delta K_{ab} - \Delta K h_{ab} = 8\pi S_{ab} = E u_a u_b - P(h_{ab} - u_a u_b) \tag{6.2}$$

where $h_{ab} = g_{ab} + n_a n_b$ is the induced metric on the shell (with $n^a_\pm = (\dot{R}_s, \dot{t}_\pm)$ an outward pointing unit normal on each side of the shell), $\Delta K_{ab} = K^+_{ab} - K^-_{ab}$ is the jump in extrinsic curvature across the shell, and $S_{ab} = \int_-^+ T_{ab}$ is the energy momentum of the wall, here assumed to take a perfect fluid form.

Inputting the form of the geometry into the Israel equations results in two independent "cosmological" equations

$$\begin{aligned} \dot{R}_s^2 + 1 &= (4\pi E)^2 R_s^2 + \frac{(M_+ + M_-)}{R_s} + \frac{(M_+ - M_-)^2}{(8\pi E)^2 R_s^4}, \\ \dot{E} + 2\frac{\dot{R}_s}{R_s} x(E + P) &= 0. \end{aligned} \tag{6.3}$$

A static shell requires both $\dot{R}_s$ and $\ddot{R}_s$ to be zero, which places constraints between the values of the mass and shell energy-momentum. As is conventional, we assume an equation of state for the shell

$$P = wE\,, \qquad \Rightarrow \qquad E = \frac{\rho_0}{4\pi R_s^{2(1+w)}} \tag{6.4}$$

which then gives

$$\begin{aligned} M_\mp &= \frac{4w(1+2w)R_s - (1+4w)^2 M_\pm}{f_\pm(R_s)(1+4w)^2}, \\ \rho_0^2 &= \frac{4R_s^{4w}(2wR_s - (1+4w)M_\pm)^2}{f_\pm(R_s)(1+4w)^2}. \end{aligned} \tag{6.5}$$

For a given equation of state, the minimum value of R_s is when the shell has vanishing energy (and $M_+ = M_-$ trivially)

$$R_{s,min} = \frac{(1+4w)}{2w} M_\pm. \tag{6.6}$$

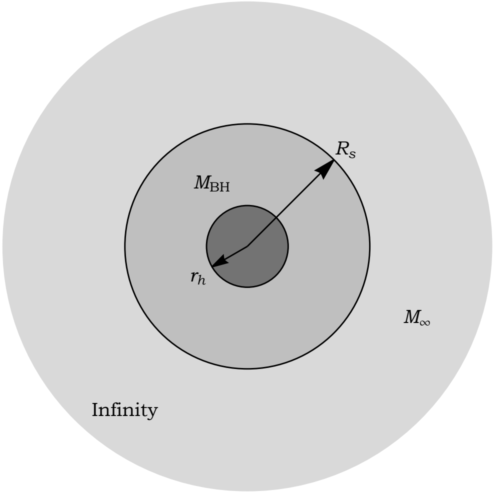

Fig. 6.1 Schematic diagram of a black hole surrounded by a thin shell (the thickness of the shell is ignored) located at $r = R_s$.

As R_s increases, the shell gradually contributes more mass to the spacetime, leading to a larger disparity between M_+ and M_-. (If $R_s < R_{s,min}$, $M_+ < M_-$, and the energy of the shell is negative.)

An important feature of a black hole spacetime of relevance to QNM's and RP's is the *light ring*, or the unstable null circular geodesic orbit at $r = 3M$. We now see three different possibilities for the shell location depending on where it is situated with respect to the light-rings of the interior and exterior Schwarzschild masses ($3M_\pm$).

(i) $R_s < 3M_-$: If $w > 1/2$, i.e. the equation of state is stiffer than radiation, then (6.6) shows that it is possible for the shell to lie 'inside' the light-ring of the black hole. Since the local Schwarzschild mass is M_+ outside the shell, this means that the $3M_-$ light-ring no longer exists, and the spacetime will have only one light-ring at $r = 3M_+$. Conversely, if $w \le 1/2$, then (6.6) shows that the shell can never lie inside the inner light-ring.

(ii) $3M_- \le R_s \le 3M_+$: This configuration, where the shell lies between the light-rings, is possible for equations of state with $w \in (\frac{\sqrt{3}-1}{4}, 1]$, and the spacetime will have both light-rings present.

(iii) $R_s > 3M_+$: If the shell lies outside the light-ring of the exterior geometry, then again there is only one light-ring in the spacetime, although it is now *inside* the shell at $3M_-$. Demanding positivity of $R_s - 3M_+$ for $R_s \ge R_{s,min}$ shows that this requires the equation of state parameter $w < 1/2$.

Having derived all the possible configurations of the shell, we conclude this section by altering our notation slightly to align with that of Macedo et al. [203], in which a global coordinate system (t, r, θ, ϕ) is used:

$$ds^2 = A(r)dt^2 - B(r)^{-1}dr^2 - r^2 d\Omega^2. \tag{6.7}$$

Note, we did not begin with this global system as it is not possible to define a global time coordinate unless the shell is static, and we wanted to derive all possible consistent static configurations commensurate with physical equations of state. Replacing $M_- = M_{\text{BH}}$ and $M_+ = M_\infty$, these metric functions are:

$$\begin{aligned} A(r) &= \begin{cases} \alpha(1 - 2M_{\text{BH}}/r), & r < R_s \\ 1 - 2M_\infty/r, & r > R_s, \end{cases} \\ B(r) &= \begin{cases} 1 - 2M_{\text{BH}}/r, & r < R_s \\ 1 - 2M_\infty/r, & r > R_s, \end{cases} \end{aligned} \tag{6.8}$$

where α is inserted to ensure the induced metric on the shell is well defined from each side

$$\alpha = \frac{R_s - 2M_\infty}{R_s - 2M_{\text{BH}}}, \tag{6.9}$$

and B contains a jump at the shell to represent the discontinuity in the extrinsic curvature. A cartoon of the spacetime geometry is given in Fig. 6.1.

6.3 Geodesic motion on a dirty black hole spacetime

DBH spacetimes can exhibit critical effects of geometrical optics. We will see later that this rich geodesic structure can be used to understand features in the scattering of waves. The important notion emerging from the geodesic motion relevant to the study of resonances is the *light-ring* or *photon sphere*. It corresponds to a local maximum and an unstable equilibrium point of the effective geodesic potential and offers an intuitive link to QNMs [224]. It is, therefore, natural to ask about the structure of the light-rings in DBH spacetimes. We note that the link between QNMs and light-rings is however not exact [225] and a simple geodesic analysis is not always sufficient to characterise the resonances of a system, as we will see later.

Geodesic motion on static DBH spacetimes has been studied in, e.g., [203], hence we simply note the key steps of the calculation. The Lagrangian of a stream of particles propagating along null geodesics in DBH spacetime is

$$\mathcal{L} = \frac{1}{2}\left(-A(r)\dot{t}^2 + \frac{1}{B(r)}\dot{r}^2 + r^2\dot{\phi}^2\right) \equiv 0 \tag{6.10}$$

in which the overdot indicates a derivative with respect to the affine parameter of the curve. By a judicious choice of affine parameter, the equation of motion of a null geodesic takes the form

$$\dot{r}^2 + B(r)\left(\frac{L^2}{r^2} - \frac{1}{A(r)}\right) = \dot{r}^2 + U_{\text{eff}}(r) = 0 \tag{6.11}$$

where without loss of generality, the geodesic is taken to lie in the equatorial plane, A and B were given in (6.8), and $L = \partial\mathcal{L}/\partial\dot{\phi} = r^2\dot{\phi}$ is a conserved (not necessarily integer) quantity along the geodesic related to the angular momentum (the affine parameter is chosen so that $E = -\partial\mathcal{L}/\partial\dot{t} = A\dot{t} = 1$).

The discontinuity of B across the shell means this potential is also discontinuous, however the interpretation of the level of the potential as a “kinetic” energy remains, and we can use the graph of $U_{\text{eff}}(r)$ to not only interpret geodesic motion, but also to infer more general scattering phenomena. The main feature of the potential, resulting from the discontinuity, is the possible existence of two local maxima.

A further interesting feature of these geometries is the possibility of geodesics that remain trapped between the light-rings. While these obviously will not be visible from far away, we might expect the existence of these resonant trajectories to correspond to some imprint in the scattering cross sections. Indeed, even for the case of a single light-ring, when that is located inside the shell, we see the sharp discontinuity in the potential at the shell location gives rise to a sharp “dip” in the potential (see Fig. 6.2). While this dip results in a change of direction for the light ray, it does not ‘trap’ the (classical) geodesic,

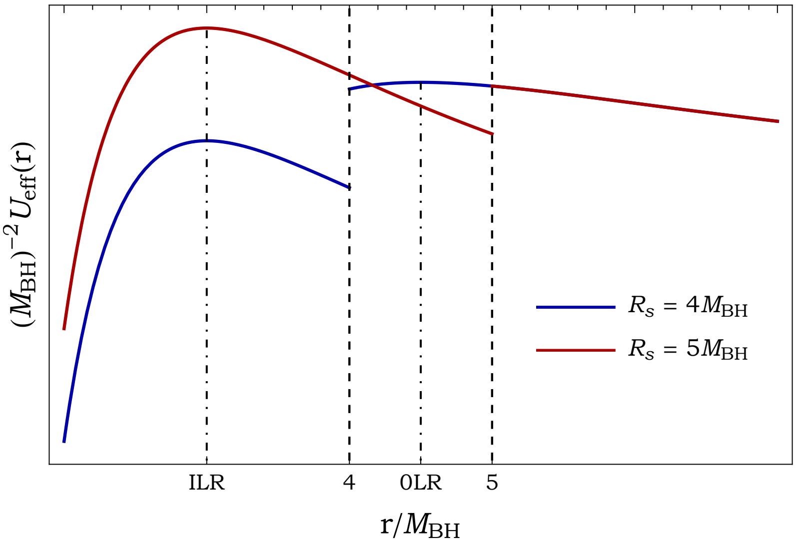

Fig. 6.2 Illustration of the geodesic potential for the two configurations of DBH studied later on with $M = 1.5M_{\rm BH}$ and $R_S = 4M_{\rm BH}$ (blue curve) or $R_S = 5M_{\rm BH}$ (red curve). In the latter case, the shell is located outside of the outer light-ring (OLR) and therefore only exhibits a single light-ring structure. The former has the shell between the OLR and inner light-ring (ILR) and exhibits the two light-rings structure. (Features of the potential have been exaggerated to better illustrate the structure.)

however a quantum mechanical system would display an effect. The scattering of scalar waves of the dirty black hole might therefore be expected to detect this dip.

As we will see in section 6.5, the properties of the local maxima of the geodesic potential can be seen in the resonance spectrum leading to two separated branches. We also identify a third branch related precisely to the dip referred to above - indicative of quasibound states trapped between the light-ring and the shell.

Before turning our attention to the spectrum of resonances of DBH, we first anticipate the effects expected to be present in the scattering based on the geodesic structure presented above. The link between geodesic motion and scattering effect is best seen through the deflection angle which we now discuss.

6.3.1 Deflection angle and classical scattering

The deflection angle is an important geometrical quantity that allows us to analyze in the classical limit the differential scattering cross section. In the case of DBH, the classical scattering cross section for null geodesics can be defined as [15] (see also [226])

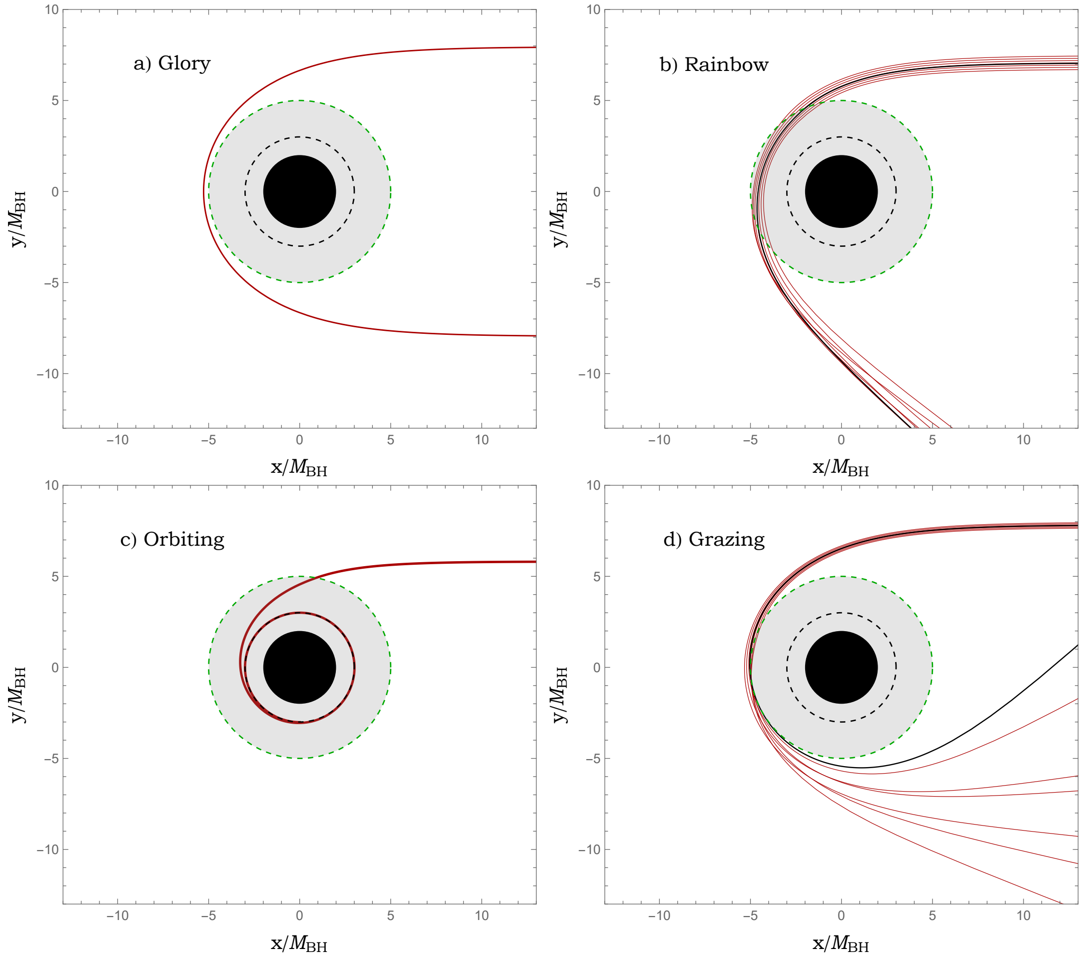

Fig. 6.3 Illustration of the various critical effects in a dirty black hole spacetime. Here we have chosen the configuration where the shell lies outside the light-ring of the exterior geometry, i.e., $R_S = 5M_{\rm BH}$ and $M_\infty = 1.5M_{\rm BH}$. In all pictures, the black disc represents the inner black hole with mass $M_{\rm BH}$, the dashed green circle represents the location of the shell at $r = R_S$ and the dashed black circle depicts the inner light-ring at $r = 3M_{\rm BH}$. a) The picture depicts glory scattering. In this case, the defection angle function $\Theta(b)$ passes smoothly through π, i.e., geodesics are scattered in the backward direction. b) The picture illustrates rainbow scattering. In this case, a congruence of geodesics centred around the rainbow impact parameter $b = b_r$ is presented (solid red curves). The rainbow ray (black solid curve) defines an extremal angle, called the rainbow angle, beyond which rays cannot be deflected locally. c) The picture depicts the orbiting phenomenon. In this case, the deflection angle is divergent for a critical impact parameter $b = b_c$ and a particle orbits indefinitely at $r = 3M_{\rm BH}$ around the light-ring. d) The picture represents grazing rays. A congruence of rays centred around the grazing impact parameter $b = b_{R_s}$ is shown (solid red curves). The grazing ray (solid black curve) sets the boundary of the so-called edge region.

$$\frac{d\sigma}{d\Omega} = \frac{b}{\sin(\theta)} \frac{1}{\left|\frac{d\Theta_{\text{geo}}(b)}{db}\right|} \tag{6.12}$$

and the geodesic deflection angle is given by

$$\Theta_{\text{geo}}(b) = 2\int_0^{u_0} du \left[B(u)\frac{1-A(u)b^2u^2}{A(u)b^2}\right]^{-1/2} - \pi, \tag{6.13}$$

where $u = 1/r$ and $u_0 = 1/r_0$ with r_0 being a turning point.

In (6.12) and (6.13), the geodesic deflection angle is related to the scattering angle θ by

$$\Theta(b) + 2n\pi = \pm\theta \tag{6.14}$$

with $n \in \mathbb{N}$ such that θ remains in “its interval of definition”, i.e. $[0,\pi]$ and b is the impact parameter of the scattered null geodesic.

There are four main scattering effects, each associated with a specific property of the deflection angle that we briefly review for the reader before qualitatively describing the scattering of waves in DBH spacetimes. They can be cast into two classes: the divergent class or the interference class.

The divergent class: glories and rainbows

- *The glory*: If the deflection function passes smoothly through 0 or π, i.e. if geodesics are scattered in the forward or backward direction, then the semi-classical cross section contributions from these geodesics will diverge. Expanding the deflection function around the glory point to linear order, one can cure this singularity and obtain a semi-classical expression for the glory in terms of Bessel functions [227]. The typical behaviour associated with the glory is therefore an increase of the scattering amplitude in the forward or backward direction. The glory effect is well known in black hole physics and also appears in these DBH spacetimes. Fig. 6.3 a) shows one backscattered ray contributing to the glory effect in the case of a DBH studied in the following.

- *Rainbow scattering*: From (6.12), we can see that $d\sigma/d\Omega$ can diverge for $\theta \neq 0$ or π if $d\Theta_{geo}/db = 0$. An impact parameter b_r, for which the deflection function is stationary defines an extremal angle, called the rainbow angle θ_r. For $b \sim b_r$, no rays can be deflected beyond θ_r. This will result in interferences on one side of the rainbow angle (known as the illuminated side) and to exponential decay on the other (known as the dark side). Similarly to the glory, one can expand the deflection function to second order in the vicinity of the rainbow point to obtain a semi-classical description built on the Airy function. The typical behaviour of rainbow scattering is an enhanced amplitude near the rainbow angle with oscillations on one side of the rainbow and exponential decay on the other side. This effect was shown to appear in astrophysical settings [228] as well as in gravitational analogues [229]. Fig. 6.3 b) shows rainbow rays in the case of a DBH studied in the following.

The interference class: orbiting and grazing

- *Orbiting*: Orbiting belongs to the interference class of critical effects and is associated with a critical impact parameter b_c for which the deflection angle diverges $\lim_{b \to b_c} \Theta_{geo} = \infty$. This implies that geodesics with an impact parameter close to b_c can be deflected with arbitrary angles. In other words, they orbit around the scatterer. This divergence also implies that there will be infinitely many geodesics deflected at any angles, causing interference at arbitrary angles. Orbiting is well known in black hole physics and is associated with the existence of the light-ring previously mentioned [230]. Fig. 6.3 c) shows the orbiting of geodesics in a DBH spacetime. Since orbiting allows geodesics to be deflected to arbitrary angles, it is naturally linked to the glory effect. Indeed it was shown, using the CAM approach, that the two effects can be incorporated in a unified semi-classical formula built around the properties of surface waves propagating on the light-ring [223].

- *Grazing*: Grazing is another critical effect belonging to the interference class. Grazing (also known as edge effects) appears when the scatterer exhibits a discontinuity [231, 232]. The discontinuity of the scatterer will lead to a singular point in the deflection function which defines an extremal angle beyond which rays cannot be deflected. This is similar to the rainbow effect with the main difference being the fact that the deflection function is not stationary at the grazing angle. Therefore, grazing will lead to interferences but does

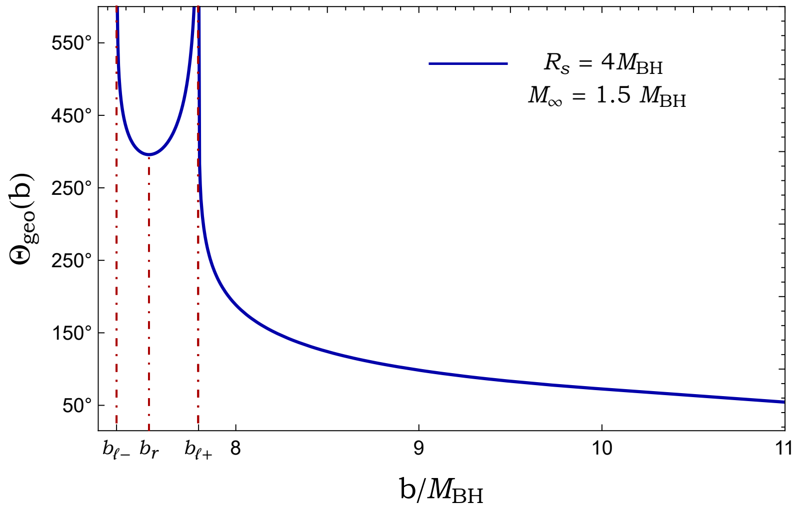

Fig. 6.4 Deflection angle as a function of the impact parameter obtained from (6.13). Here we assume $M_\infty = 1.5 M_{\rm BH}$, and the shell position $R_s = 4M_{\rm BH}$. The deflection angle diverges at both critical parameters $b_{\ell_-} = 3\sqrt{3}M_{\rm BH}/\sqrt{\alpha}$ and $b_{\ell_+} = 3\sqrt{3}M_\infty$ associated with a light-ring at $r_{\ell_-} = 3M_{\rm BH}$ and $r_{\ell_+} = 3M_\infty$ respectively. There is also a stationary point in the deflection angle, i.e. $\Theta'_{\rm geo}(b_r) = 0$, leading to the rainbow effect.

not necessarily imply an increase in the scattering amplitude as was the case in rainbow scattering. Fig. 6.3 d) shows grazing rays in a DBH spacetime studied in the following.

6.3.2 Critical effects in DBH spacetimes

Equipped with the terminology and intuition from the semi-classical description of critical effects, we now turn our attention to scattering in DBH spacetimes.

As we noted in the previous section, there are three main geometric cases classified by the location of the shell relative to the light-ring radii of the inner and outer masses.

Case 1: $R_S < 3M_{\rm BH}$**.** In this case, the shell is located inside the inner light-ring and therefore cannot be probed by geodesics escaping to infinity. From the point of view of geodesics, this case is therefore similar to the one of an isolated black hole.

Case 2: $3M_{\rm BH} < R_S < 3M_\infty$**.** If the shell lies between the light-rings, then there is the possibility for geodesics to probe each light-ring separately. Each light-ring is associated with a divergence of the deflection angle, leading to orbiting. In the case where both light-rings are accessible to geodesics, we expect two such divergences to be present, associated with orbiting around the inner and outer light-rings. Hence we further anticipate that there exists a value of $b_{\ell_-} < b < b_{\ell_+}$ such that the deflection angle is extremal. This

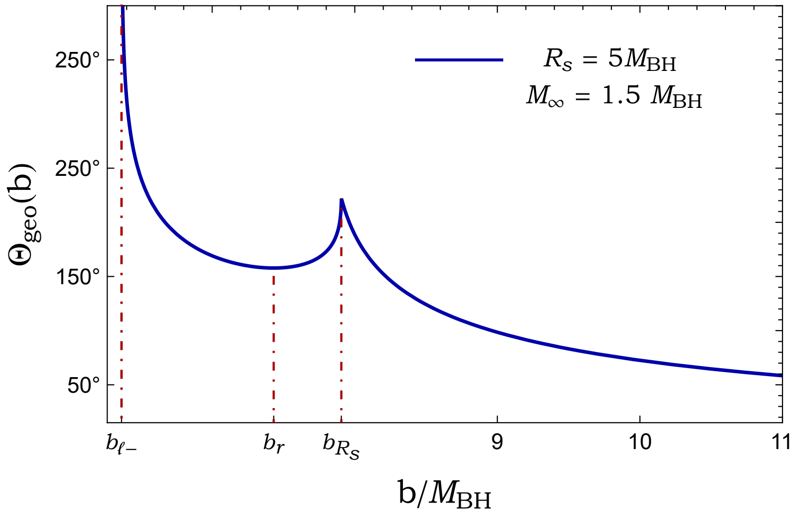

Fig. 6.5 Deflection angle as a function of the impact parameter obtained from (6.13). Here we assume $M_\infty = 1.5M_{\rm BH}$, and the shell position $R_s = 5M_{\rm BH}$. The deflection angle diverges at a critical parameter $b_{\ell_-} = 3\sqrt{3}M_{\rm BH}/\sqrt{\alpha}$ associated with a light-ring at $r_{\ell_-} = 3M_{\rm BH}$. There is also a stationary point in the deflection angle, i.e. $\Theta'_{\rm geo}(b_r) = 0$, leading to the rainbow effect. A local maximum occurring at $b = b_{R_s} = \sqrt{R_S^3/(R_S - 2M_\infty)}$ is also present, leading to grazing. A congruence of geodesics in this specific DBH configuration is represented in Fig. 6.6.

implies the presence of a fold caustic and leads to rainbow scattering [15]. The deflection angle revealing these critical effects is represented in Fig. 6.4 for the configuration where the shell is located between the two light-rings. In this configuration, and for the choice of parameters $R_S = 4M_{\rm BH}$ and $M_\infty = 1.5M_{\rm BH}$, the rainbow angle $\theta_r \approx 35.8°$ and is associated with the impact parameter b_r. The presence of rainbow scattering in DBH spacetimes was noted in [204] but its characteristic amplification was not clearly observed in their simulation due to the specific choice of DBH configurations.

Case 3: $R_S > 3M_\infty$. If the shell lies outside $3M_\infty$, a single light-ring is present in the geometry, which is now located *inside* the shell. In this case, the orbiting effect is qualitatively the same as for an isolated black hole and is associated with the critical impact parameter $b = 3\sqrt{3}M_{\rm BH}/\sqrt{\alpha}$. In this configuration, a second local maximum of the potential is present. Contrary to the previous case, this maximum is not associated with the second light-ring but rather to the presence of the shell (see Fig. 6.2). Since this second local maximum is not an (unstable) equilibrium point, it will not be associated with a divergence of the deflection angle but rather with a singular point (i.e. the deflection

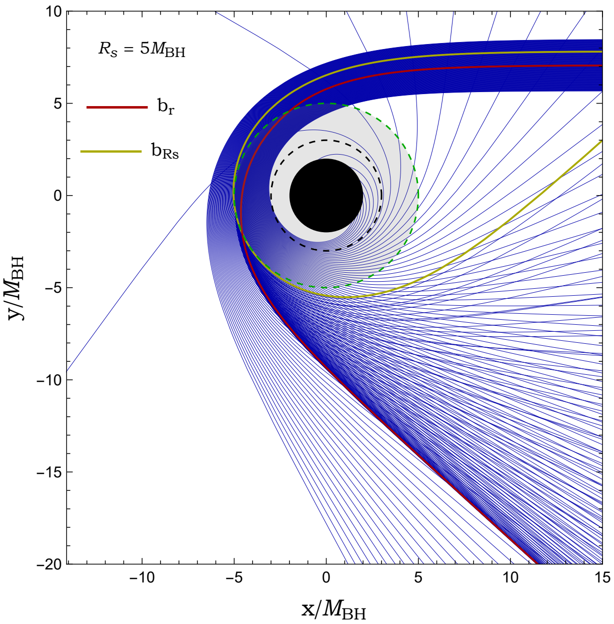

Fig. 6.6 Null geodesics scattered by a DBH. In this case, we assume $M_\infty = 1.5M_{\rm BH}$ and $R_s = 5M_{\rm BH}$ and the incident geodesics are equally spaced. The impact parameter varies between $0.95b_c < b < 1.35b_c$ with a fixed step size $\Delta b = 0.04b_c$. The red solid line is the rainbow ray and has an impact parameter ($b = b_r = 1.1677b_c$) and, we can see a high concentration of rays in this direction leading to the characteristic amplification of the rainbow effect. The olive curve represents the grazing ray.

function is not differentiable). It is important to note that the singular point occurring at $b = b_{R_S} = \sqrt{R_S^3/(R_S - 2M_\infty)}$ is a local maximum of the deflection angle, but does not satisfy the condition $d\Theta_{geo}/db = 0$, which implies that it is *not* associated to rainbow scattering as stated in [204]. Instead, this singular point will lead to grazing as discussed previously. Similar to the previous case, there is an impact parameter associated to rainbow scattering between the orbiting impact parameter and the grazing one. In this configuration, and for the choice of parameters $R_S = 5M_{\rm BH}$ and $M_\infty = 1.5M_{\rm BH}$, the rainbow angle $\theta_r \approx 157.8°$. Fig. 6.5 depicts the deflection function of such a configuration and Fig. 6.6 depicts a congruence of geodesics in this DBH set-up. The red and dark green rays in Fig. 6.6 represent the rainbow and grazing ray respectively and are both associated with an extremal angle. Note the qualitative difference between the rainbow and grazing ray which resides in the concentration of geodesics around each critical trajectory.

6.4 Waves on a dirty black hole spacetime

We consider a scalar field, $\Phi(x)$, propagating on the DBH spacetime, governed by the Klein-Gordon equation

$$\Box\Phi \equiv \frac{1}{\sqrt{-g}}\partial_\mu\left(\sqrt{-g}g^{\mu\nu}\partial_\nu\Phi\right) = 0 \tag{6.15}$$

where $g^{\mu\nu}$ is the inverse metric and g is the metric determinant. Performing a standard separation of variables,

$$\Phi = \frac{1}{r}\sum_{\omega\ell m}\phi_{\omega\ell}(r)Y_{\ell m}(\theta,\phi)e^{-i\omega t}, \tag{6.16}$$

leads to a radial equation of the form

$$\left[\frac{d^2}{dr_*^2} + \omega^2 - V_\ell(r)\right]\phi_{\omega\ell} = 0, \tag{6.17}$$

where $V_\ell(r)$ is the effective potential which is given by

$$V_\ell(r) = A(r)\Big[\frac{\ell(\ell+1)}{r^2} + \frac{2}{r^3}\left(M_{\text{BH}}\Theta(R_s - r) + M_\infty\Theta(r - R_s)\right)\Big] \tag{6.18}$$

with Θ being the Heaviside step function, and r_* denotes the *tortoise coordinate* defined by

$$\frac{dr_*}{dr} = \frac{1}{\sqrt{A(r)B(r)}}, \tag{6.19}$$

viz.

$$r_*(r) = \begin{cases} \frac{1}{\sqrt{\alpha}}\left[r + M_{\text{BH}}\ln\left(\frac{r}{M_{\text{BH}}} - 1\right)\right] + \kappa & M_{\text{BH}}<r\leq R_s, \\ r + 2M_\infty\ln\left(\frac{r}{2M_\infty} - 1\right) & r>R_s, \end{cases} \tag{6.20}$$

where the constant κ is fixed so that $r_*(r)$ is continuous.

In the following, we introduce the modes $\phi^{\text{in}}_{\omega\ell}$ which are solutions of (6.17) and are defined by their behaviour at the horizon $r = 2M_{\text{BH}}$ (i.e., for $r_* \to -\infty$) and at spatial infinity

$r \to +\infty$ (i.e., for $r_* \to +\infty$):

$$\phi^{\text{in}}_{\omega\ell}(r_*) \sim \begin{cases} e^{-i\omega r_*} & (r_* \to -\infty), \\ A^{(-)}_\ell(\omega) e^{-i\omega r_*} + A^{(+)}_\ell(\omega) e^{+i\omega r_*} & (r_* \to +\infty). \end{cases} \tag{6.21}$$

Here, the coefficients $A^{(-)}_\ell(\omega)$ and $A^{(+)}_\ell(\omega)$ appearing in (6.21) are complex amplitudes and allow us to define the scattering S-matrix elements,

$$S_\ell(\omega) = e^{i(\ell+1)\pi} \frac{A^{(+)}_\ell(\omega)}{A^{(-)}_\ell(\omega)}. \tag{6.22}$$

It should be noted that, due to the choice of coordinates (keeping r as the areal radius on both sides of the shell) the transverse metric is discontinuous at the shell meaning that we have to also place a boundary condition on the eigenfunctions $\phi_{\omega\ell}$ at the shell [203]:

$$\left[\sqrt{B(R_s)} \Big(R_s \phi'_{\omega\ell}(R_s) - \phi_{\omega\ell}(R_s) \Big) \right]_+ = \left[\sqrt{B(R_s)} \Big(R_s \phi'_{\omega\ell}(R_s) - \phi_{\omega\ell}(R_s) \Big) \right]_- \tag{6.23}$$

6.5 Resonances of the dirty black holes

6.5.1 Quasinormal modes and Regge poles

Resonant modes are characteristic solutions of the wave equation, (6.17), satisfying purely ingoing/outgoing boundary conditions at the horizon/infinity. Their spectrum is the set of zeros of the scattering matrix $S_\ell(\omega)$ (6.22), i.e., a simple pole of $A^{(-)}_\ell(\omega)$. It can be seen as a set of frequencies $\omega_{\ell n}$ in the complex-ω plane at which the scattering matrix $S_\ell(\omega)$ has a simple pole for $\ell \in \mathbb{N}$ and $\omega_{\ell n} \in \mathbb{C}$ (the so-called *quasinormal mode spectrum*), or a set of angular momenta $\lambda_n(\omega) \equiv \ell_n + 1/2$ in the complex-λ plane at which the scattering matrix has a simple pole for $\omega \in \mathbb{R}$ and $\lambda_n(\omega) \in \mathbb{C}$ (the so-called *Regge pole spectrum*). Here $n = 1, 2, 3, \ldots$ labels the different elements of the spectrum and is referred to as the overtone number.

The quasinormal mode spectrum of DBHs has been investigated for configurations where $M_\infty - M_{\text{BH}} \ll 1$ using perturbative techniques [201, 202]. We shall now consider, for the first time, the Regge poles of generic DBHs.

6.5.2 Numerical method

To compute the QNM/Regge pole spectrum of dirty black holes, we follow the method of Ould El Hadj et al. [233] who calculated the Regge pole spectrum of scalar and gravitational waves (in the axial sector) for a gravitating compact body. Their method is an extension of the original continued fraction method developed originally by Leaver [234, 235].

The method involves writing the solution to the wave equation (6.17) as a power series around a point b located outside the shell,

$$\phi_{\omega,l}(r) = e^{i\omega r_*(r)} \sum_{n=0}^{+\infty} a_n \left(1 - \frac{b}{r}\right)^n , \tag{6.24}$$

where the coefficients a_n obey a four-term recurrence relation:

$$\alpha_n a_{n+1} + \beta_n a_n + \gamma_n a_{n-1} + \delta_n a_{n-2} = 0, \quad \forall n \geq 2, \tag{6.25}$$

where

$$\alpha_n = n(n+1)\left(1 - \frac{2M_\infty}{b}\right), \tag{6.26a}$$

$$\beta_n = n\left[\left(\frac{6M_\infty}{b} - 2\right)n + 2ib\omega\right], \tag{6.26b}$$

$$\gamma_n = \left(1 - \frac{6M_\infty}{b}\right)n(n-1) - \frac{2M_\infty}{b} - \ell(\ell+1), \tag{6.26c}$$

$$\delta_n = \left(\frac{2M_\infty}{b}\right)(n-1)^2 . \tag{6.26d}$$

The initialisation coefficients, a_0 and a_1, are found directly from (6.24),

$$a_0 = e^{-i\omega r_*(b)} \phi_{\omega_\ell}(b), \tag{6.27}$$

$$a_1 = b e^{-i\omega r_*(b)} \left(\frac{d}{dr} \phi_{\omega_\ell}(r)\Big|_{r=b} - \frac{i\omega b}{b - 2M_\infty} \phi_{\omega_\ell}(b) \right). \tag{6.28}$$

In practise, the coefficients a_0 and a_1 are found numerically by integrating (6.17) from the horizon up to $r = b > R_s$.

In order to apply Leaver's method, we first perform a Gaussian elimination step in order to reduce the 4-term recurrence relation to a 3-term recurrence relation:

$$\hat{\alpha}_n a_{n+1} + \hat{\beta}_n a_n + \hat{\gamma}_n a_{n-1} = 0, \tag{6.29}$$

where we have defined the new coefficients for $n \geq 2$:

$$\hat{\alpha}_n = \alpha_n, \tag{6.30a}$$

$$\hat{\beta}_n = \beta_n - \hat{\alpha}_{n-1} \frac{\delta_n}{\hat{\gamma}_{n-1}}, \text{ and} \tag{6.30b}$$

$$\hat{\gamma}_n = \gamma_n - \hat{\beta}_{n-1} \frac{\delta_n}{\hat{\gamma}_{n-1}}. \tag{6.30c}$$

The series expansion (6.24) is convergent outside the shell provided that a_n is a minimal solution to the recurrence relation and $b/2 < R_s < b$ [236]. The existence of a minimal solution implies that the following continued fraction holds:

$$\frac{a_1}{a_0} = \frac{-\hat{\gamma}_1}{\hat{\beta}_1 -} \frac{\hat{\gamma}_2 \hat{\alpha}_1}{\hat{\beta}_2 -} \frac{\hat{\gamma}_3 \hat{\alpha}_2}{\hat{\beta}_3 -} \dots \tag{6.31}$$

The above relation (or any of its inversions) is the equation, written in the standard form of continued fractions, we are solving in order to find the RP/QNM spectrum. In practise, we fix ω (equivalently ℓ), and define a function $f(\ell \in \mathbb{C})$ (equivalently $f(\omega \in \mathbb{C})$), which gives the difference between the left-hand side and right-hand side of the condition (6.31). We then find the zeros of the function f starting from an initial guess.

An alternative method to the continued fraction expression is to use the Hill determinant [237], where one looks for the zeros of the following determinant

$$D = \begin{vmatrix} \beta_0 & \alpha_0 & 0 & 0 & 0 & \dots & \dots & \dots \\ \gamma_1 & \beta_1 & \alpha_1 & 0 & 0 & \dots & \dots & \dots \\ \delta_2 & \gamma_2 & \beta_2 & \alpha_2 & 0 & \dots & \dots & \dots \\ \vdots & \ddots & \ddots & \ddots & \ddots & \ddots & \dots & \dots \\ \vdots & \vdots & \delta_{n-1} & \gamma_{n-1} & \beta_{n-1} & \alpha_{n-1} & \ddots & \dots \\ \vdots & \vdots & \vdots & \delta_n & \gamma_n & \beta_n & \alpha_n & \ddots \\ \vdots & \vdots & \vdots & \vdots & \ddots & \ddots & \ddots & \ddots \end{vmatrix} = 0. \tag{6.32}$$

By assuming D_n

$$D_n = \beta_n D_{n-1} - \gamma_n \alpha_{n-1} D_{n-2} + \delta_n \alpha_{n-1} \alpha_{n-2} D_{n-3}, \tag{6.33}$$

to be the determinant of the $n \times n$ submatrix of D with the initial conditions

$$\begin{aligned} D_0 &= \beta_0, \\ D_1 &= \beta_1 \beta_0 - \gamma_1 \alpha_0, \\ D_2 &= \beta_0(\beta_1\beta_2 - \alpha_1\gamma_2) - \alpha_0(\alpha_1\delta_2 - \gamma_1\beta_2). \end{aligned} \tag{6.34}$$

the Regge poles (QNM frequencies) are found by solving numerically the roots λ_n (ω_n) of D_n.

We note that in order to confirm our results, we have used both methods and they give the same results, up to the numerical precision.

6.5.3 Results: The Regge pole spectrum

In order to check the robustness of our numerical code, we first compute the QNM spectrum for a configuration of DBH considered by Leung et al. [201, 202], i.e., for $M_\infty = 1.02 M_{\text{BH}}$, $R_s = 2{,}52 M_{\text{BH}}$ and assuming $M_{\text{BH}} = 1/2$.

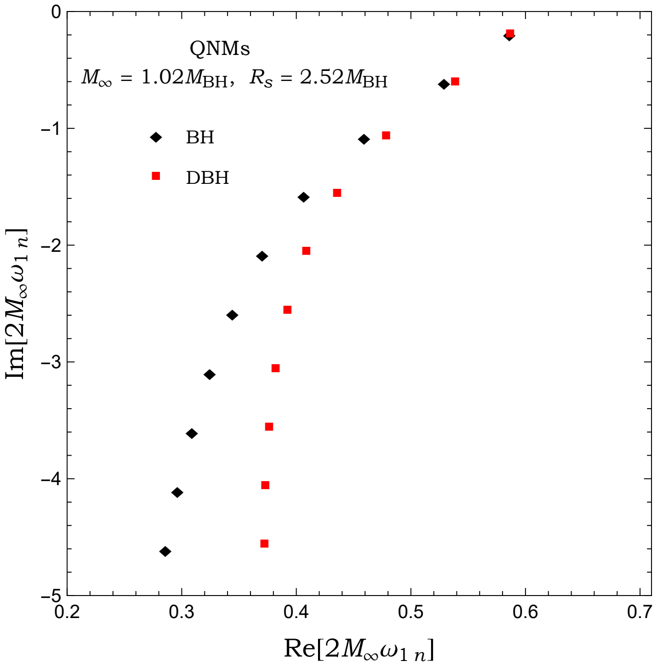

Fig. 6.7 The ($\ell = 1, n = 1, \ldots, 10$) quasinormal modes of the scalar field. We assume $2M_{\rm BH} = 1$.

In Fig. 6.7, we show the QNM spectrum corresponding to the DBH configuration studied by Leung et al. for ($\ell = 1, n = 1, \ldots, 10$). We see that it agrees with Fig. 4 of [202]. The data for quasinormal frequencies $\omega_{\ell n}$ is listed in Table 6.1.

In Figs 6.8, 6.9 and 6.10, we present the numerical results for the Regge pole spectrum of DBH's in two configurations: (i) a DBH where the shell is located between the inner and outer light-rings ($3M_{\rm BH} < R_s < 3M_\infty$), so that both light-rings are present in the geometry, and (ii) a DBH where the shell is located outside the outer light-ring ($R_s > 3M_\infty$), so that only a single light-ring is present in the geometry, but this is *inside* the shell. The Regge poles for each configuration are presented for various frequencies.

Fig. 6.8 shows the Regge pole spectrum for the first configuration with parameters $M_\infty = 1.5M_{\rm BH}$ and $R_s = 4M_{\rm BH}$ for two different frequencies $2M_\infty\omega = 3$ and 6. For both frequencies, the Regge pole spectrum exhibits two branches, represented in blue and red. For low overtones, the two branches merge, with the distinction becoming clear at higher overtones. Note that the splitting occurs for smaller values of n as one increases the frequency. We can identify the origin of both branches as coming from the existence of two light-rings if $3M_{\rm BH} < R_S < 3M_\infty$ or from the inner-ring and the shell if $R_S > 3M_\infty$.

Table 6.1 A sample of the first quasinormal frequencies $\omega_{\ell n}$ of the scalar field. The radius of the thin shell is $R_s = 2.52M_{\rm BH}$ and the ADM mass is $M_\infty = 1.02M_{BH}$. We assume $2M_{\rm BH} = 1/2$.

ℓ	n	$2M_\infty\omega_{\ell n}$
1	1	$0.586628 - 0.190512i$
	2	$0.538645 - 0.601030i$
	3	$0.478474 - 1.064024i$
	4	$0.435656 - 1.555056i$
	5	$0.408698 - 2.055042i$
	6	$0.392365 - 2.556656i$
	7	$0.381985 - 3.058495i$
	8	$0.376255 - 3.559562i$
	9	$0.372953 - 4.060316i$
	10	$0.372266 - 4.560224i$

This can be seen from the low overtone origin of the branches. Indeed for the fundamental modes, their Regge poles can be estimated from the critical impact parameters $b_c = b_{\ell_\pm}$ or $b_c = b_{R_S}$, i.e., $\mathrm{Re}(\lambda_n(\omega)) \sim \omega b_c$ [238] with $b_{\ell_+} = 3\sqrt{3}M_\infty$, $b_{\ell_-} = 3\sqrt{3}M_{\rm BH}/\sqrt{\alpha}$ and $b_{R_S} = \sqrt{R_S^3/(R_S - 2M_\infty)}$. For example, for the configuration with $M_\infty = 1.5M_{\rm BH}$, $R_S = 5M_{\rm BH}$ and $2M_\infty\omega = 32$, and we find that the real part of the fundamental Regge pole associated with the inner photon sphere and the shell are approximately 66.88 and 84.33 respectively which agree remarkably well with the numerical values presented in Table 6.3.

Fig. 6.9 shows the spectrum of the Regge pole also for the first configuration with the same parameters but for two different high frequencies $2M_\infty\omega = 16$ and 32. We can see that the structure of the spectrum remains the same, however for very high frequencies (lower panel), we can see the emergence of a new branch (purple triangles) between the two branches associated with the inner and outer light-rings.

Fig. 6.10 shows the Regge pole spectrum for $2M_\infty\omega = 16$ and 32 and this for the second configuration ($R_s > 3M_\infty$) with parameters $M_\infty = 1.5M_{\rm BH}$ and $R_s = 5M_{\rm BH}$. The structure remains the same for both frequencies but the number of poles in the middle branch has increased with frequency.

The Regge poles fall into three distinct classes. We can see that they are relatively similar to the Regge pole spectrum studied in the case of compact objects (see [233]).

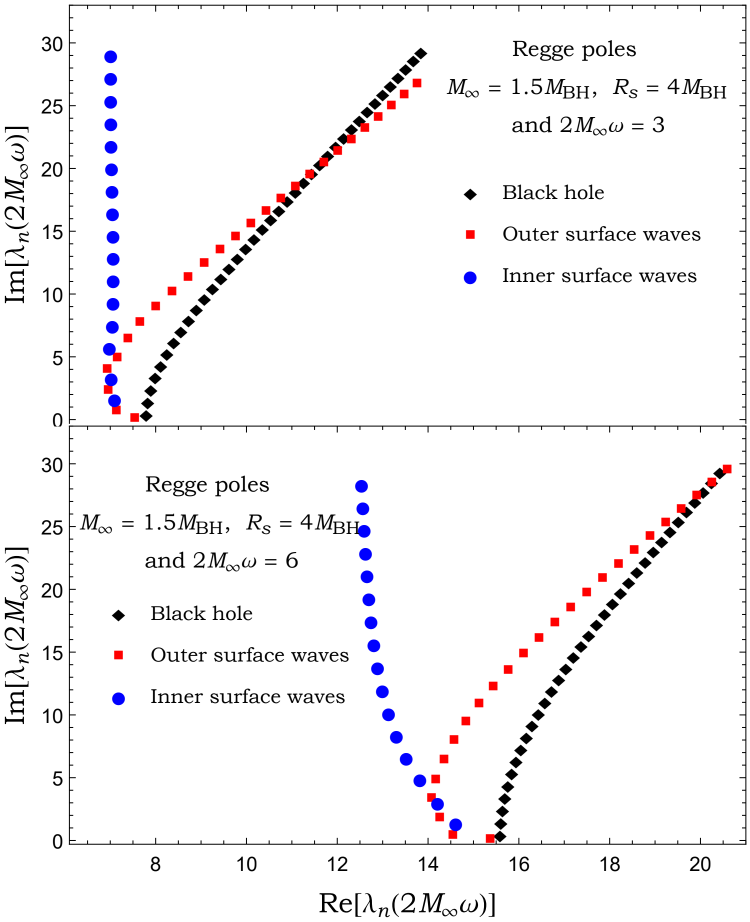

Fig. 6.8 The Regge poles $\lambda_n(\omega)$ for the scalar field in a DBH spacetime with parameters $M_\infty = 1.5M_{\rm BH}$, $R_S = 4M_{\rm BH}$ and for frequencies $2M_\infty\omega = 3$ (upper panel) and $2M_\infty\omega = 6$ (lower panel). (We take $2M_{\rm BH} = 1$ to produce these plots). In both panels, the blue circle and red square branches correspond to the outer and inner surface waves for the DBH spacetime while the black diamond branch is the one for an isolated black hole of mass $M_{\rm BH}$.

Therefore, we will adopt the terminology already introduced by these authors (see, also, Nussenzveig [239] for the origin of this terminology). We have thus :

1. *Broad resonances*: poles with a relatively constant imaginary part which is therefore parallel to the real axis with an approximately uniform spacing. They are sensitive to the position of the shell and to its internal structure ($r < R_s$), i.e., its matter content.

2. *Inner surface waves*: strongly damped modes and their behaviour are also entirely determined by the geometry of the object. The lowest modes can be associated with waves propagating on the light-ring $r_{\ell_-} = 3M_{\rm BH}$, i.e., with the impact parameter $b_{\ell_-} = 3\sqrt{3}M_{BH}/\sqrt{\alpha}$.

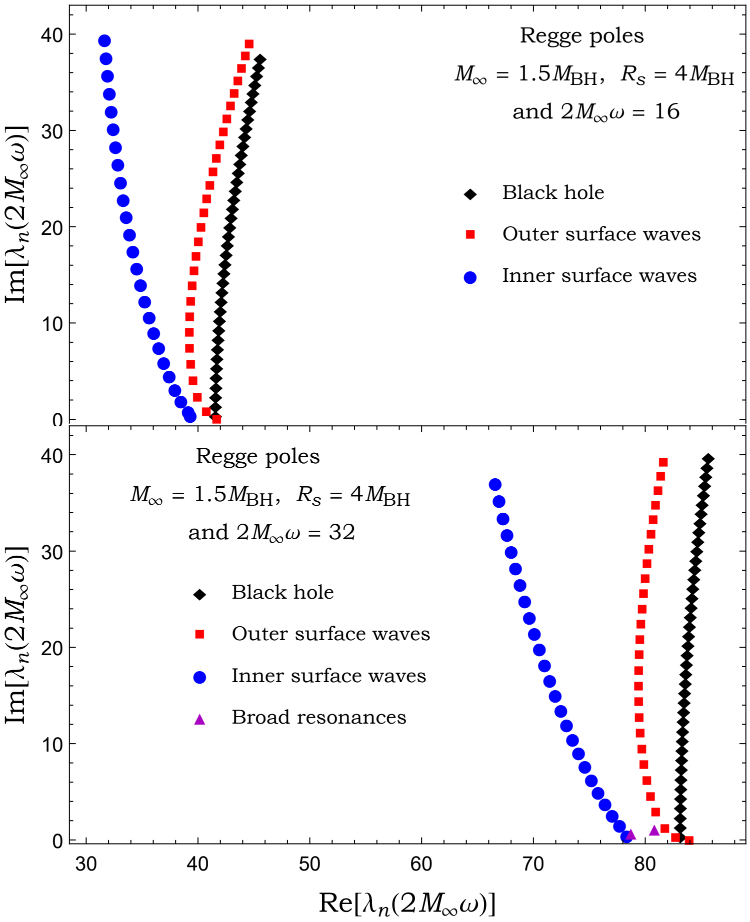

Fig. 6.9 The Regge poles $\lambda_n(\omega)$ for the scalar field in the DBH spacetime with parameters $M_\infty = 1.5M_{\rm BH}$ and $R_s = 4M_{\rm BH}$ at frequencies $2M_\infty\omega = 16$ (upper panel) and $2M_\infty\omega = 32$ (lower panel). We assume $2M_{\rm BH} = 1$. In both panels, the blue circle and red square branches correspond to the outer and inner surface waves for the DBH spacetime while the black diamond branch is the one for an isolated black hole. The purple triangles in the lower panel depict the third branch of broad resonances.

3. *Outer surface waves*: modes that depend essentially on the geometry of the object. They are highly damped and the lowest modes can be associated with:

   (i) the *surface waves* propagating on the outer light ring $r_{\ell_+} = 3M_\infty$, i.e. with the impact parameter $b_{\ell_+} = 3\sqrt{3}M_\infty$ for the configuration where the shell is located between the two light-rings ($3M_{\rm BH} < R_s < 3M_\infty$).

   (ii) the *creeping modes* propagating along the shell surface at $r = R_s$, with impact parameter $b_{R_S} = \sqrt{\frac{R_s^3}{R_s - 2M_\infty}}$ for the configuration where the shell is outside $3M_\infty$. They are generated by the edge rays (or grazing rays) in the edge region.

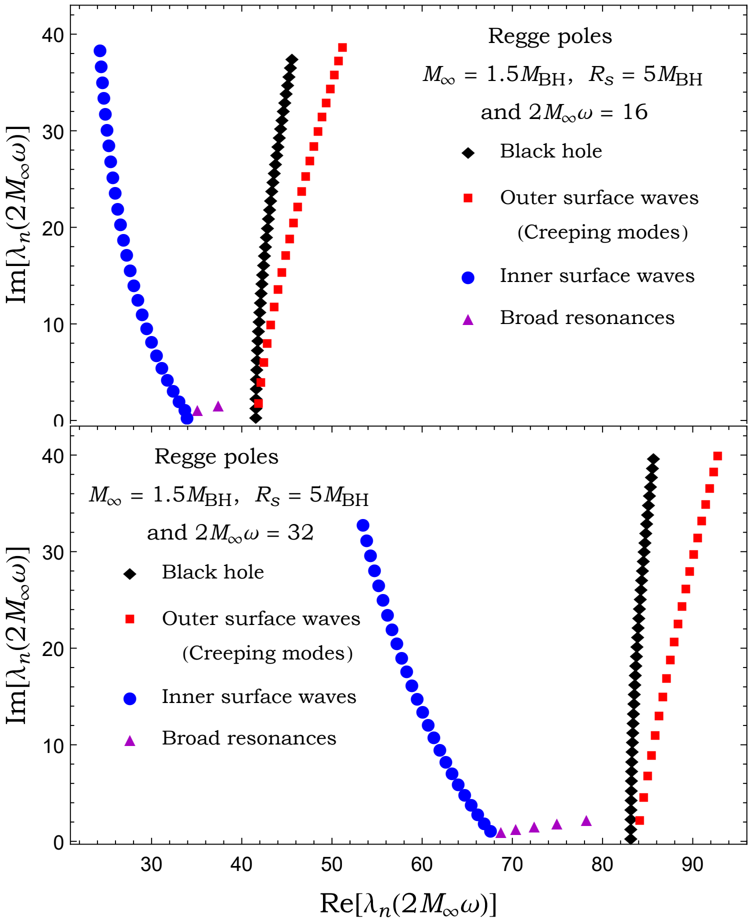

Fig. 6.10 The Regge poles $\lambda_n(\omega)$ for the scalar field in the DBH spacetime with parameters $M_\infty = 1.5M_{\rm BH}$ and $R_s = 5M_{\rm BH}$ at frequencies $2M_\infty\omega = 16$ (upper panel) and $2M_\infty\omega = 32$ (lower panel). We assume $2M_{\rm BH} = 1$. In both panels, the blue circle and red square branches correspond to the outer (creeping modes) and inner surface waves for the DBH spacetime while the black diamond branch is the one for an isolated black hole. The purple triangles depict the third branch of broad resonances. As the frequency increases the surface wave branches move away and more broad resonances appear in between them.

In Figs 6.8, 6.9 and 6.10 the outer surface waves (surface waves and/or creeping modes), broad resonances and inner surface waves are shown as red squares, purple triangles, and blue circles, respectively. The black diamonds represent the Regge poles of the isolated Schwarzschild black hole of mass $M_{\rm BH}$.

The lowest Regge poles are listed in (i) Table 6.2 for DBH with parameters $M_\infty = 1.5M_{\rm BH}$ and $R_s = 4M_{\rm BH}$ and for $2M_\infty\omega = 3$, 6, 16 and 32, and (ii) Table 6.3 for DBH with parameters $M_\infty = 1.5M_{\rm BH}$ and $R_s = 5M_{\rm BH}$ and for $2M_\infty\omega = 16$ and 32.

Table 6.2 The lowest Regge poles $\lambda_n(\omega)$ for the scalar field. The radius of the thin shell is $R_s = 4M_{BH}$ and the ADM mass is $M_\infty = 1.5M_{BH}$.

$2M_\infty\omega$	n	$\lambda_n^{(\text{O-S-W})^1}(\omega)$	$\lambda_n^{(\text{I-S-W})^2}(\omega)$	$\lambda_n^{(\text{B-R})^3}(\omega)$
3	1	$7.539449+0.223849i$	$7.095909+1.687068i$	/
	2	$7.134677+0.790874i$	$7.022852+3.3708566i$	/
	3	$6.956727+2.438228i$	$6.980154+5.790685i$	/
	4	$6.934368+4.114637i$	$7.049810+7.549115i$	/
	5	$7.154584+5.016518i$	$7.063185+9.371734i$	/
	6	$7.390189+6.5269387i$	$7.066195+11.160583i$	/
	7	$7.652774+7.865429i$	$7.067851+12.940759i$	/
	8	$8.001365+9.087813i$	$7.062229+14.719719i$	/
	9	$8.362859+10.289717i$	$7.051567+16.502463i$	/
	10	$8.715833+11.441810i$	$7.039533+18.290428i$	/
6	1	$15.370841+0.179585i$	$14.611707+1.414356i$	/
	2	$14.548787+0.528288i$	$14.209917+3.071463i$	/
	3	$14.255707+1.927388i$	$13.820181+4.931434i$	/
	4	$14.075994+3.476095i$	$13.520911+6.640027i$	/
	5	$14.169925+4.925956i$	$13.303758+8.406231i$	/
	6	$14.352709+6.542016i$	$13.132015+10.207303i$	/
	7	$14.572460+8.082838i$	$12.995979+12.028643i$	/
	8	$14.832787+9.558134i$	$12.889802+13.859215i$	/
	9	$15.124109+10.975998i$	$12.808015+15.691713i$	/
	10	$15.437413+12.345040i$	$12.745238+17.521595i$	/
16	1	$41.670935+0.046352i$	$39.308955+0.526143i$	/
	2	$40.757178+0.815017i$	$39.123982+0.945890i$	/
	3	$39.944801+2.350849i$	$38.477482+2.002715i$	/
	4	$39.562328+4.058189i$	$37.936546+3.242729i$	/
	5	$39.354113+5.746829i$	$37.428640+4.601256i$	/
	6	$39.253632+7.417623i$	$36.946769+6.047137i$	/
	7	$39.231469+9.068162i$	$36.487997+7.562487i$	/
	8	$39.269947+10.696820i$	$36.051294+9.134979i$	/
	9	$39.357086+12.302735i$	$35.636215+10.755451i$	/
	10	$39.484150+13.885587i$	$35.242599+12.416733i$	/
32	1	$83.931483+0.001076i$	$78.343315+0.569228i$	$78.717561+0.863328i$
	2	$82.718881+0.302994i$	$77.708251+1.655406i$	$80.826502+1.279706i$
	3	$81.765639+1.257533i$	$77.049161+2.705208i$	/
	4	$80.934661+2.942484i$	$76.407917+3.858777i$	/
	5	$80.484718+4.574505i$	$75.788245+5.093969i$	/
	6	$80.144197+6.211451i$	$75.189451+6.395209i$	/
	7	$79.887645+7.854207i$	$74.609971+7.751822i$	/
	8	$79.697425+9.498636i$	$74.048266+9.156061i$	/
	9	$79.561618+11.141534i$	$73.503036+10.602050i$	/
	10	$79.471725+12.780560i$	$72.973244+12.085172i$	/

[1] O-S-W : Outer surface waves

[2] I-S-W : Inner surface waves

[3] B-R : Broad resonances

Table 6.3 The lowest Regge poles $\lambda_n(\omega)$ for the scalar field. The radius of the thin shell is $R_s = 5M_{BH}$ and the ADM mass is $M_\infty = 1.5M_{BH}$.

$2M_\infty\omega$	n	$\lambda_n^{\text{(O-S-W)}^1}(\omega)$	$\lambda_n^{\text{(I-S-W)}^2}(\omega)$	$\lambda_n^{\text{(B-R)}^3}(\omega)$
16	1	$41.860118 + 1.784810i$	$33.945579 + 0.477813i$	$35.086529 + 1.294345i$
	2	$42.120571 + 3.964122i$	$33.695542 + 1.278693i$	$37.393437 + 1.734247i$
	3	$42.451238 + 6.041693i$	$33.057993 + 2.190304i$	/
	4	$42.818104 + 8.030389i$	$32.399192 + 3.251233i$	/
	5	$43.205922 + 9.949368i$	$31.759081 + 4.409909i$	/
	6	$43.608414 + 11.811534i$	$31.143492 + 5.647996i$	/
	7	$44.022224 + 13.625389i$	$30.554809 + 6.952932i$	/
	8	$44.445123 + 15.396893i$	$29.994263 + 8.315144i$	/
	9	$44.875425 + 17.130499i$	$29.462624 + 9.726841i$	/
	10	$45.311767 + 18.829705i$	$28.960402 + 11.181362i$	/
32	1	$84.123387 + 2.204783i$	$67.582661 + 1.284484i$	$68.724166 + 1.194667i$
	2	$84.576124 + 4.572500i$	$66.893567 + 2.072605i$	$70.375698 + 1.488244i$
	3	$85.005575 + 6.802744i$	$66.166349 + 2.972146i$	$72.419573 + 1.755117i$
	4	$85.428874 + 8.940819i$	$65.438785 + 3.951276i$	$74.941664 + 2.039113i$
	5	$85.849013 + 11.011312i$	$64.718695 + 4.996764i$	$78.206962 + 2.394064i$
	6	$86.267934 + 13.029013i$	$64.009870 + 6.099179i$	/
	7	$86.687058 + 15.003322i$	$63.314252 + 7.251465i$	/
	8	$87.107350 + 16.940586i$	$62.632891 + 8.448162i$	/
	9	$87.529435 + 18.845339i$	$61.966385 + 9.684914i$	/
	10	$87.953689 + 20.720964i$	$61.315094 + 10.958141i$	/

[1] O-S-W : Outer surface waves (creeping modes)

[2] I-S-W : Inner surface waves

[3] B-R : Broad resonances

6.5.4 The WKB approximation

In order to gain insight into the physical origin of the broad resonances identified in Figs. 6.9 and 6.10, we now turn to the WKB approximation.

Propagation of WKB modes

We begin by constructing the WKB solution to (6.17) by assuming that solutions are rapidly oscillating functions with slowly varying amplitudes:

$$\phi_\ell(r_*) = A(r_*)e^{i\int p(r_*')dr_*'}. \tag{6.35}$$

Inserting this ansatz into the wave equation, and assuming that $|p'| \ll |p^2|$ and $|A'| \ll |pA|$, we get that

$$p(r_*)^2 + V(r_*) = 0, \quad A = a|p|^{-1/2}, \tag{6.36}$$

where a is a constant coefficient, $V = V_\ell - \omega^2$, and we suppress ω and ℓ indices for clarity. The first of the above equations is quadratic in p, thus it will admit two solutions that can be interpreted as waves travelling radially inward and outward. Taking into account contributions from both modes, we can write the following WKB solution to the wave equation:

$$\phi_\ell = |p|^{-1/2}\left(a^{in}e^{-i\int pdr_*} + a^{out}e^{i\int pdr_*}\right). \tag{6.37}$$

We see from the above expression that, in regions where the WKB approximation holds, the only change to the amplitudes of the modes comes from the variation of the function p. It is also clear that the WKB approximation breaks down at those points which satisfy $V(r_*) = 0$, since it implies that $p = 0$, leading to an infinite amplitude of the WKB modes. The points satisfying $V(r_*) = 0$, are called turning points and one can write a WKB solution on both sides of the turning points, with different coefficients (a^{in}, a^{out}) on each side. One then relates the WKB modal coefficients on each side of the turning points by applying connection formulae (see [240]). Between turning points, the WKB modes do not mix and their propagation between two points r_{*i} and r_{*j} is captured by the following propagation matrices:

$$\begin{pmatrix} a_i^{out} \\ a_i^{in} \end{pmatrix} = P_{ij} \begin{pmatrix} a_j^{out} \\ a_j^{in} \end{pmatrix}, \tag{6.38}$$

where

$$P_{ij} = \begin{pmatrix} e^{-iS_{ij}} & 0 \\ 0 & e^{iS_{ij}} \end{pmatrix} \quad \text{when} \quad p^2(r_{*i} < r_* < r_{*j}) > 0, \tag{6.39}$$

or

$$P_{ij} = \begin{pmatrix} 0 & e^{-S_{ij}} \\ e^{S_{ij}} & 0 \end{pmatrix} \quad \text{when} \quad p^2(r_{*i} < r_* < r_{*j}) < 0. \tag{6.40}$$

In the above formula, S_{ij} is the WKB action between the points r_{*i} and r_{*j} and is given by

$$S_{ij} = \int_{r_{*i}}^{r_{*j}} |p(r_*)| dr_*. \tag{6.41}$$

Combining the propagation matrix for modes below the potential barrier and the connection matrices across isolated turning points, we define the tunneling matrix, T_{12}, which connects WKB modes on the outside of two turning points r_{*_1} and r_{*_2}:

$$T_{12} = \begin{pmatrix} 1/\mathcal{T} & -\mathcal{R}/\mathcal{T}, \\ \mathcal{R}^*/\mathcal{T} & 1/\mathcal{T}^*. \end{pmatrix}, \tag{6.42}$$

where $\mathcal{R}$ and $\mathcal{T}$ are the local reflection and transmission coefficients across the potential barrier and are given by:

$$\mathcal{R} = -i\frac{1 - e^{-2S_{12}}/4}{1 + e^{-2S_{12}}/4} \tag{6.43}$$

$$\mathcal{T} = \frac{e^{-2S_{12}}}{1 + e^{-2S_{12}}/4} \tag{6.44}$$

WKB modes across the shell

In order to construct the full WKB solution across the entire radial range, we also need to connect WKB modes on both sides of the shell. Since we are only interested in the qualitative behaviour of the WKB modes in order to interpret the broad resonance, we assume here that the jump discontinuity in the potential is much smaller than the frequencies of the WKB modes, ω, and that this frequency does not vary significantly near the shell. Within this framework, we write the WKB solution for $r \sim R_s$ as:

$$\phi_{\omega,l}(r_*) = \begin{cases} a_L^{out} e^{i\omega r_*} + a_L^{in} e^{-i\omega r_*} \text{ for } r_* \leq R_s^*, \\ a_R^{out} e^{i\omega r_*} + a_R^{in} e^{-i\omega r_*} \text{ for } r_* \geq R_s^*. \end{cases} \tag{6.45}$$

From the junction condition at the shell given in (6.23), we can define the connection matrix, C, which connects the WKB modal coefficients on the left and right sides of the shell:

$$C = \begin{pmatrix} 1 & -e^{-2i\omega R_s} \frac{\Delta}{2i\omega} \\ e^{2i\omega R_s} \frac{\Delta}{2i\omega} & 1 \end{pmatrix}, \tag{6.46}$$

where $\Delta = \frac{\sqrt{AB_+} - \sqrt{AB_-}}{R_s}$. Note that Δ is not the discontinuity of the potential but rather the coefficient entering in the discontinuity of the field's derivative. From the connection matrix, we can also define a reflection coefficient across the shell:

$$\mathcal{R}_s = \frac{\Delta}{2i\omega}. \tag{6.47}$$

Note here that the reflection across the discontinuity is of order $O(\omega^{-1})$. This is due to the fact that the metric itself is discontinuous at the shell and is in contrast with the case of a compact object which usually has a continuous metric and for which the reflection coefficient at the surface of the object is at least of order $O(\omega^{-2})$ [241, 242].

WKB estimate of the broad resonances

We now have all the necessary quantities to relate the modal coefficient at $r_* \to -\infty$ to the one at $r_* \to +\infty$. This is done by combining the propagating, tunnelling and connection matrix as follows (see Fig. 6.11 for illustration):

$$\begin{pmatrix} a_{-\infty}^{out} \\ a_{-\infty}^{in} \end{pmatrix} = P_{-\infty 1} \times T_{12} \times P_{2R_s} \times C \times P_{R_s \infty} \begin{pmatrix} a_{\infty}^{out} \\ a_{\infty}^{in} \end{pmatrix}. \tag{6.48}$$

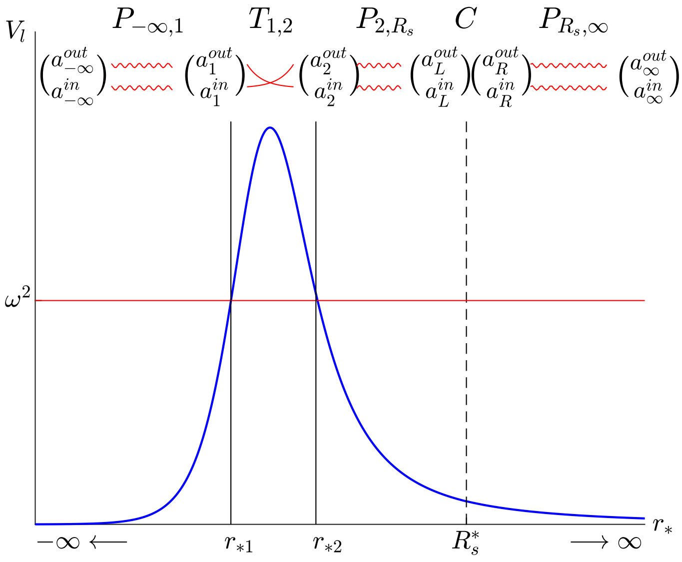

Fig. 6.11 Illustration of the connection formula (6.48) obtained by combining the propagating, tunnelling and connection matrix to relate the WKB modal coefficient across the turning points and the shell. The oscillating (growing/decaying) lines represent the propagation of WKB modes with real (imaginary) momenta p.

Solving the above system for outgoing boundary conditions, that is $a^{out}_{-\infty} = a^{in}_{\infty} = 0$, leads to the following condition:

$$e^{-2iS_{2R_s}-2i\omega R_s} = \mathcal{R}\mathcal{R}_s. \tag{6.49}$$

We now anticipate that broad resonances will be slowly damped and therefore the real part of their RPs will be much greater than their imaginary part. We write $\lambda = \lambda_R + i\Gamma$, with $\Gamma \ll \lambda_r$. The real and imaginary parts of the above condition give

$$\sin\left(S_{2R_S}(\lambda_R) + \omega R_s - \frac{\pi}{4}\right) = 0 \text{ and } \Gamma = \frac{\ln(|\mathcal{R}\mathcal{R}_s|)}{2\partial_\lambda S_{2Rs}\big|_{\lambda_R}}. \tag{6.50}$$

Hence the location of the shell sets the real part of the broad resonances part of the RP spectrum while its matter content sets their imaginary part. Contrary to the other branches of the RP spectrum, the above systems admit a finite number of solutions. In particular, we must have the turning points located between the outer light-ring and the shell, which limits the range of λ_R.

Solving the above condition numerically for the shell parameters of Fig. 6.9, we find that there are only two solutions, $\lambda^{(1)}_{\text{WKB}} = 35.6946 + 1.79675i$ and $\lambda^{(2)}_{\text{WKB}} = 38.2285 + 2.8487i$, which differ from the values found numerically by 2.2% and 3.7%, respectively.

6.6 Wave Scattering by a dirty black hole

In this section, we compute the differential scattering cross sections $d\sigma/d\Omega$ for plane monochromatic scalar waves impinging upon a DBH using the partial wave expansion, and we compare with the results constructed by CAM representations of these cross sections by means of the Sommerfeld-Watson transform and Cauchy theorem [206–208].

6.6.1 The differential scattering cross section: Partial waves expansion

The differential scattering cross section for a scalar field is given by [186]

$$\frac{d\sigma}{d\Omega} = |f(\omega,\theta)|^2 \tag{6.51}$$

where

$$f(\omega,\theta) = \frac{1}{2i\omega}\sum_{\ell=0}^{\infty}(2\ell+1)[S_\ell(\omega)-1]P_\ell(\cos\theta) \tag{6.52}$$

denotes the scattering amplitude. In (6.52), the functions $P_\ell(\cos\theta)$ are the Legendre polynomials [243] and the S-matrix elements $S_\ell(\omega)$ were given by (6.22).

6.6.2 CAM representation of the scattering amplitude

Following the steps in [222], we construct the CAM representation of $f(\theta)$ using a Sommerfeld-Watson transformation [207, 208, 206]

$$\sum_{\ell=0}^{+\infty}(-1)^\ell F(\ell) = \frac{i}{2}\int_C d\lambda\,\frac{F(\lambda-1/2)}{\cos(\pi\lambda)}, \tag{6.53}$$

where $F(\cdot)$ is any function without singularities on the real axis λ. By means of (6.53), we replace the discrete sum over the ordinary angular momentum ℓ in (6.52) with a contour integral in the complex λ plane (i.e., in the complex ℓ-plane with $\lambda = \ell + 1/2$). By noting that $P_\ell(\cos\theta) = (-1)^\ell P_\ell(-\cos\theta)$, we obtain

$$f(\omega,\theta) = \frac{1}{2\omega}\int_C d\lambda\,\frac{\lambda}{\cos(\pi\lambda)} \times [S_{\lambda-1/2}(\omega) - 1]\,P_{\lambda-1/2}(-\cos\theta). \tag{6.54}$$

It should be noted that, in (6.53) and (6.54), the integration contour encircles counterclockwise the positive real axis of the complex λ-plane, and $P_{\lambda-1/2}(z)$ denotes the analytic extension of the Legendre polynomials $P_\ell(z)$ which is defined in terms of hypergeometric functions by [243]

$$P_{\lambda-1/2}(z) = F[1/2-\lambda, 1/2+\lambda; 1; (1-z)/2]. \tag{6.55}$$

Here, $S_{\lambda-1/2}(\omega)$ is given by [see (6.22)]

$$S_{\lambda-1/2}(\omega) = e^{i(\lambda+1/2)\pi}\,\frac{A^{(+)}_{\lambda-1/2}(\omega)}{A^{(-)}_{\lambda-1/2}(\omega)} \tag{6.56}$$

and denotes “the” analytic extension of $S_\ell(\omega)$ where the complex amplitudes $A^{(\pm)}_{\lambda-1/2}(\omega)$ are defined from the analytic extension of the modes $\phi_{\omega\ell}$, i.e., from the function $\phi_{\omega,\lambda-1/2}$.

It is also important to recall that the Regge poles $\lambda_n(\omega)$ of $S_{\lambda-1/2}(\omega)$ lie in the first and third quadrants, symmetrically distributed with respect to the origin O, and are defined as the zeros of the coefficient $A^{(-)}_{\lambda-1/2}(\omega)$ [see (6.56)]

$$A^{(-)}_{\lambda_n(\omega)-1/2}(\omega) = 0, \tag{6.57}$$

with $n = 1, 2, 3, \ldots.$, and the associated residues at the poles $\lambda = \lambda_n(\omega)$ are defined by [see (6.56)]

$$r_n(\omega) = e^{i\pi[\lambda_n(\omega)+1/2]}\left[\frac{A^{(+)}_{\lambda-1/2}(\omega)}{\frac{d}{d\lambda}A^{(-)}_{\lambda-1/2}(\omega)}\right]_{\lambda=\lambda_n(\omega)}. \tag{6.58}$$

In order to collect the Regge pole contributions, we deform the contour C in (6.54) while using the Cauchy theorem to obtain

$$f(\omega,\theta) = f^{\mathrm{B}}(\omega,\theta) + f^{\mathrm{RP}}(\omega,\theta) \tag{6.59}$$

where

$$f^{\mathrm{B}}(\omega,\theta) = f^{\mathrm{B,Re}}(\omega,\theta) + f^{\mathrm{B,Im}}(\omega,\theta) \tag{6.60a}$$

is a background integral contribution with

$$f^{\mathrm{B,Re}}(\omega,\theta) = \frac{1}{\pi\omega}\int_{C_-} d\lambda\, \lambda S_{\lambda-1/2}(\omega) Q_{\lambda-1/2}(\cos\theta + i0) \tag{6.60b}$$

and

$$\begin{aligned} f^{\mathrm{B,Im}}(\omega,\theta) = {} & \frac{1}{2\omega}\Bigg(\int_{+i\infty}^{0} d\lambda\, \big[S_{\lambda-1/2}(\omega)P_{\lambda-1/2}(-\cos\theta) \\ - {} & S_{-\lambda-1/2}(\omega)e^{i\pi(\lambda+1/2)}P_{\lambda-1/2}(\cos\theta)\big]\frac{\lambda}{\cos(\pi\lambda)}\Bigg). \end{aligned} \tag{6.60c}$$

The second term in (6.59)

$$f^{\mathrm{RP}}(\omega,\theta) = -\frac{i\pi}{\omega}\sum_{n=1}^{+\infty}\frac{\lambda_n(\omega)r_n(\omega)}{\cos[\pi\lambda_n(\omega)]}\times P_{\lambda_n(\omega)-1/2}(-\cos\theta), \tag{6.61}$$

is a sum over the Regge poles lying in the first quadrant of the CAM plane. Of course, the CAM representation of the scattering amplitude $f(\omega,\theta)$ for the scalar field given by (6.59) and (6.60) is equivalent to the initial partial wave expansion (6.52). From this CAM representation, we extract the contribution $f^{\mathrm{RP}}(\omega,\theta)$ given by (6.61) which is only an approximation of $f(\omega,\theta)$, and which provides us with a corresponding approximation of the differential scattering cross section via (6.51).

6.6.3 Computational methods

In order to construct the scattering amplitude (6.52), and the Regge pole contribution (6.61), it is necessary first to obtain the function $\phi^{\mathrm{in}}_{\omega\ell}(r)$, the coefficients $A^{(\pm)}_{\ell}(\omega)$, and the

S-matrix elements $S_\ell(\omega)$ by solving (6.17) with conditions (6.21), and second to compute the Regge poles $\lambda_n(\omega)$ of (6.57) and the associated residues (6.58). To do this, we use the numerical methods of [222, 223] (see Secs. III B and IVA of these papers). It is important to note that, the scattering amplitude (6.52) suffers a lack of convergence due to the long range nature of the field propagating on the Schwarzschild spacetime (outside the thin shell) and to accelerate the convergence of this sum, we have used the method described in the Appendix of [222]. All numerical calculations were performed using *Mathematica*.

6.6.4 Numerical Results and comments: Scattering cross sections

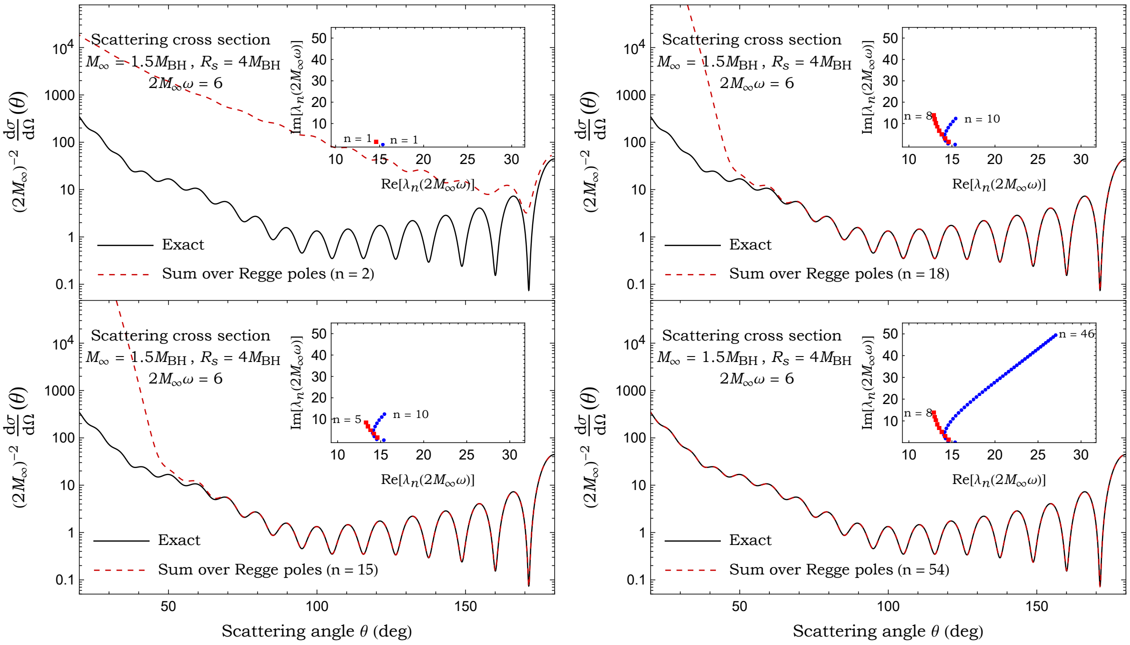

Fig. 6.12 The scalar cross section of DBH for $2M_\infty\omega = 6$, $R_s = 4M_{\rm BH}$ and $M_\infty = 1.5M_{\rm BH}$ and its Regge pole approximation. The plots show the effect of including successively more Regge poles.

We present in Figs 6.12, 6.13 and 6.14 various scattering cross sections constructed from the CAM approach, and compare with results obtained from the partial wave expansion method. As in section 6.5, we focus on two configurations of the DBH: (i) a DBH with $3M_{\rm BH} < R_s < 3M_\infty$, and (ii) DBH with $R_s > 3M_\infty$.

Fig. 6.12 shows the scattering cross section constructed from the CAM approach at $2M_\infty\omega = 6$ for a shell configuration with $M_\infty = 1.5M_{\rm BH}$ and $R_s = 4M_{\rm BH}$, i.e. for a DBH

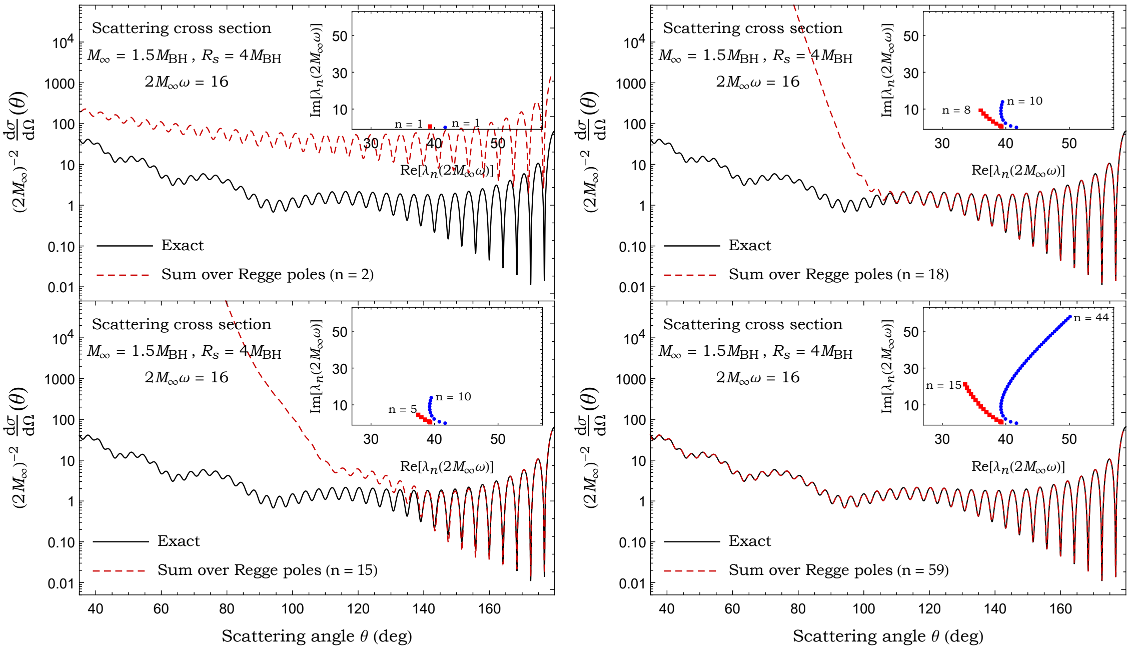

Fig. 6.13 The scalar cross section of DBH for $2M_\infty\omega = 16$, $R_s = 4M_{\rm BH}$ and $M_\infty = 1.5M_{\rm BH}$ and its Regge pole approximation. The plots show the effect of including successively more Regge poles.

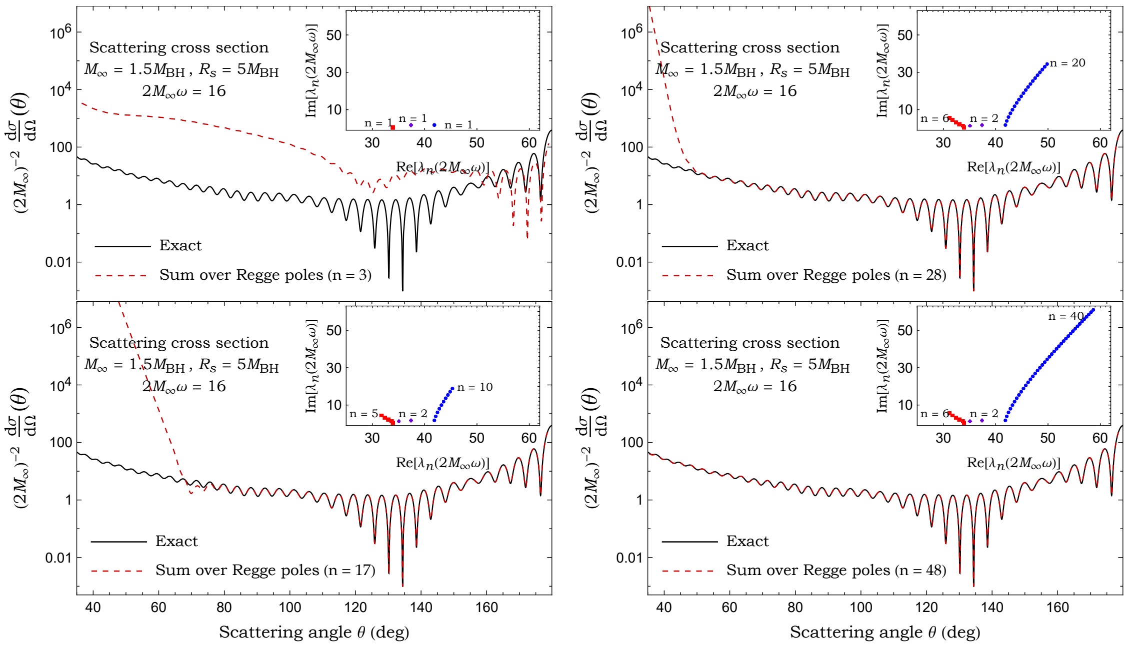

Fig. 6.14 The scalar cross section of DBH for $2M_\infty\omega = 16$, $R_s = 5M_{\rm BH}$ and $M_\infty = 1.5M_{\rm BH}$ and its Regge pole approximation. The plots show the effect of including successively more Regge poles.

configuration with $3M_{\text{BH}} < R_s < 3M_\infty$. We can see that it gets progressively closer to the scattering cross section constructed from partial wave expansion by including increasingly more Regge poles in the sum (6.61). Indeed, the sum over only the first two Regge poles in equation (6.61) does not reproduce the cross section, however, summing over 54 Regge poles, but without including the background integral, the agreement is perfect with that constructed from the partial wave expansion for $\theta \gtrsim 20°$. Fig. 6.13 illustrates, for the same

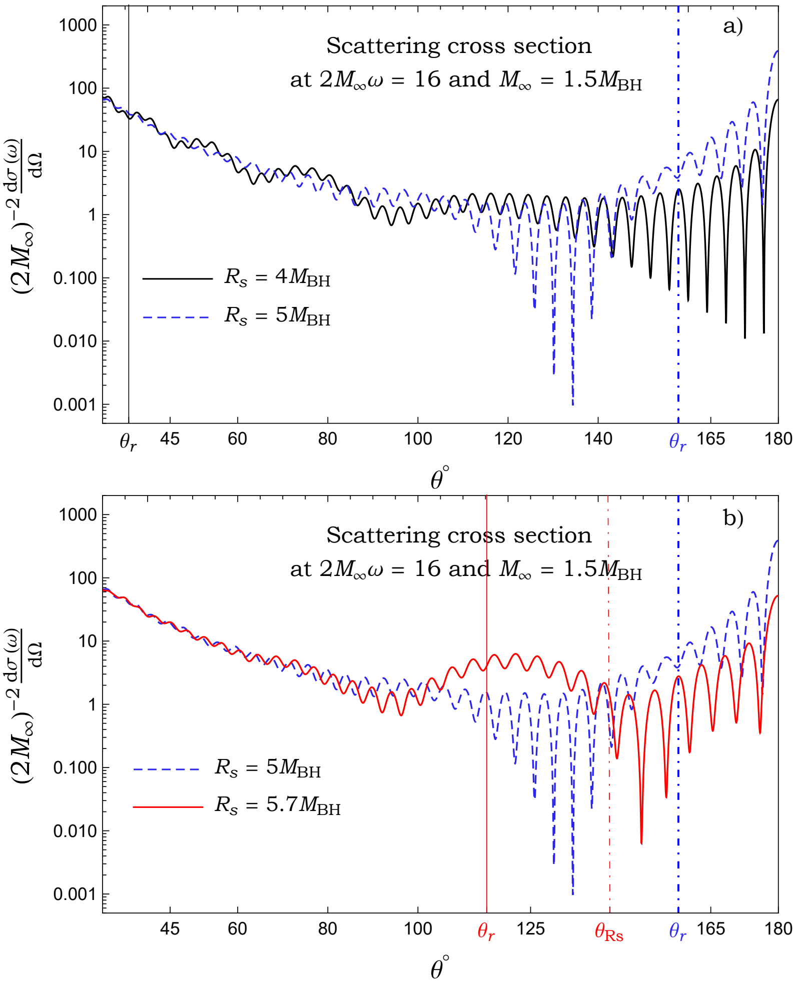

Fig. 6.15 The scalar cross section of DBH for $2M_\infty\omega = 16$, and $M_\infty = 1.5M_{\text{BH}}$. a) We compare $R_s = 5M_{\text{BH}}$ to $R_s = 4M_{\text{BH}}$. We can see that the scattering amplitude is enhanced by the rainbow effect for $R_s = 5M_{\text{BH}}$ at the rainbow angle $\theta_r \approx 157.8°$ (blue dotdashed line). b) We compare $R_s = 5M_{\text{BH}}$ to $R_s = 5.7M_{\text{BH}}$. We can see that the scattering amplitude is enhanced at $\theta_r \approx 115.3°$ (red line) for $R_s = 5M_{\text{BH}}$ and at $\theta_r \approx 157.8°$ (blue dotdashed line).

DBH configuration, the scattering cross section at high frequency $2M_\infty\omega = 16$. In this case, with just 18 Regge poles the glory and the orbiting oscillations are very well reproduced. With 59 Regge poles and without adding the background integral the result obtained from the CAM approach is again indistinguishable from partial wave expansion for $\theta \gtrsim 30^\circ$ on the plot.

Fig. 6.14 shows the scattering cross section for a DBH configuration with $R_s > 3M_\infty$ at $2M_\infty\omega = 16$. Here, we have the shell configuration with $M_\infty = 1.5M_{\text{BH}}$ and $R_s = 5M_{\text{BH}}$. In this case, to construct the result from CAM approach, we sum over three different branches and with 17 Regge poles the glory as well as the orbiting oscillations are captured. By including 48 Regge poles, but no background integral, the agreement is excellent with the partial wave expansion result for $\theta \gtrsim 30^\circ$.

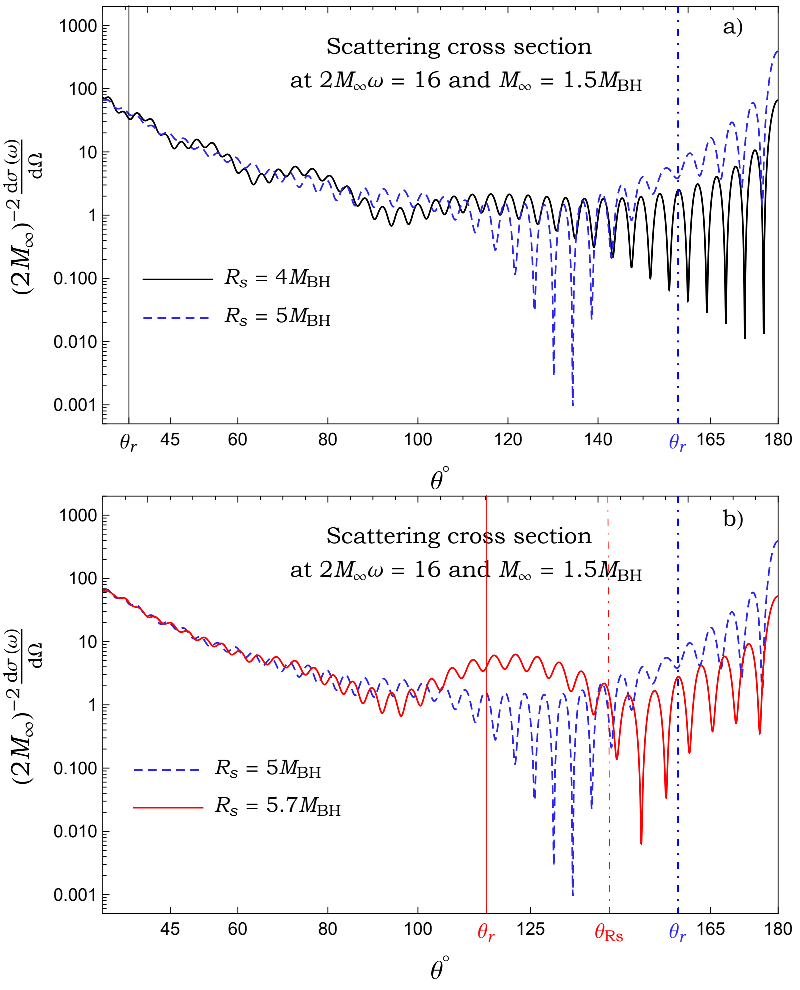

Fig. 6.16 The scalar cross section of DBH for $2M_\infty\omega = 16$, and $M_\infty = 1.5M_{\text{BH}}$. a) We compare $R_s = 5M_{\text{BH}}$ to $R_s = 4M_{\text{BH}}$. We can see that the scattering amplitude is enhanced by the rainbow effect for $R_s = 5M_{\text{BH}}$ at the rainbow angle $\theta_r \approx 157.8^\circ$ (blue dotdashed line). b) We compare $R_s = 5M_{\text{BH}}$ to $R_s = 5.7M_{\text{BH}}$. We can see that the scattering amplitude is enhanced at $\theta_r \approx 115.3^\circ$ (red line) for $R_s = 5M_{\text{BH}}$ and at $\theta_r \approx 157.8^\circ$ (blue dotdashed line).

Through Figs. 6.12, 6.13 and 6.14, we have shown that the scattering cross section can be described and understood in terms of the Regge Poles, i.e., in terms of various contributions from different types of resonances. In particular, we have identified different branches associated with the properties of the light-rings and the shell position and/or its matter content. To conclude our description of the differential scattering cross section, we return to the discussion of critical effects associated with geodesic motion described in section 6.3. We can indeed understand qualitatively the observed scattering cross sections from the various critical effects. As in the case of the isolated black hole, the orbiting effect and the glory (associated with a single light-ring) will result in oscillations in the scattering cross section as well as an increase for $\theta \sim 180^\circ$. In DBH spacetimes, we have shown that we may expect modulations due to the rainbow effect and to grazing (creeping modes) or secondary orbiting. The rainbow effect will lead to a local amplification of the scattering cross section around the rainbow angle. Grazing, i.e., the edge rays (creeping modes) or second orbiting will lead to further oscillations and global modulations of the scattering cross section. This is illustrated in Fig. 6.15. Note the qualitative difference that for configurations where the shell is outside the outer light-ring, the scattering cross is mainly modulated around the rainbow angle while for the case where the shell lies between the two light-rings the scattering cross sections exhibit noticeable modulation at all angles. Isolating and identifying quantitatively the different contributions of each the critical effect would require asymptotic formulae from the RPs and their residues which are beyond the scope of this work.

6.7 Summary

We investigated the scattering of planar waves incident on a dirty black hole spacetime. We showed that different DBH configurations depends on the shell position exhibited different scattering phenomena relevant to optical scattering. We recalled general results concerning the differential scattering cross section in the classical limit through a null geodesic analysis by exploring different configurations of the shell. In particular, we show that dirty black hole spacetimes may exhibit various critical effects for geometrical optics.

We computed the Regge pole spectrum for various shell configurations and found that it exhibits two or three distinct branches of poles, labelled inner surface waves, broad resonances and outer surface waves. In the latter, two subfamilies were identified, the surface waves associated with the outer light-ring and the creeping modes associated with the surface of the shell. We applied WKB analysis and found that the position of the shell sets the real part of the broad resonances while its energy-momentum and the discontinuity of the potential at the shell's surface set their imaginary part.

We provided the complex angular momentum representation of the differential scattering cross section and examined the role of the different Regge pole branches. We computed the differential scattering cross section for various configurations at several frequencies and showed a very good agreement with the partial-wave calculations.

Finally, we highlighted the role of the critical effects, i.e., orbiting, glory, grazing, and rainbow scattering, and their impact on the differential scattering cross section.

Chapter 7

Conclusion and outlook

This thesis explored various aspects of black holes and the vacuum. In Chapter 1, we presented the motivation for our research and outlined the structure of the thesis. In Chapter 2, We reviewed the historical background of black holes, contemporary observational results, and different black hole models to provide an overview of the background for the presented research. Chapter 3, covered instanton and bounce solutions in one-dimensional quantum mechanics and generalized these concepts to the studies of false vacuum decay in quantum field theory, including the effects of gravity. Chapters 1, 2, and 3 formed the introductory part of this thesis, laying out the groundwork for the technical research presented in the subsequent chapters.

The key research conclusions of this thesis can be divided into two main topics. The first topic focused on black holes seeded vacuum decay in different scenarios, as explored in Chapters 4 and 5. The second topic involved the study of black hole scattering represented by Regge Poles, as detailed in Chapter 6. The conclusions drawn from these individual research studies will be discussed separately.

7.1 Black hole catalysed vacuum decay

7.1.1 Vacuum metastability with primordial black holes

In Chapter 4, we studied the electroweak vacuum phase transition catalysed by primordial black holes using the Euclidean path integral. We proposed that PBHs live in a thermal plasma that is originally heated by Hawking radiation, which reaches a thermal equilibrium and remains till the end of the PBH's life. The temperature of the ambient plasma was much hotter than the surrounding Universe at that time but colder than Hawking temperature. This scenario provides an ideal mechanism for calculating the decay rate using the Euclidean methodology. We showed that PBHs, indeed, favour bubble nucleation within such a realistic environment. We compared the false vacuum decay rate Γ_{FVD} with Hawking evaporation rate Γ_{ev} and found that the ratio of Γ_{FVD}/Γ_{ev} is larger than one for the mass range of PBH we cared. This implied that false vacuum decay occurred before the PBH completely evaporated, further ensuring the reliability of our method.

Given the results of PBH favouring the false vacuum decay that occurred in our early Universe, we inferred the light PBH abundance that formed in the early Universe, which lacks observational results. We derived the most stringent constraints on the abundance of light PBHs and invalided most known results from different cosmological models that have predicted the existence of light PBHs with $0.8g < M_i < 5 \times 10^{14} g$.

7.1.2 Seeded vacuum decay with Gauss-Bonnet

In Chapter 5, we studied the impact of Guass-Bonnet terms on the false vacuum decay via two types of false vacuum decay – bubble nucleation and Hawking Moss instanton. We derived the general equations of motion for a bubble and calculated the decay rate using the Euclidean saddle point approximation, with the inclusion of the additional Gauss-Bonnet term in the gravitational action. The GB black holes are found to considerably enhance the probability of vacuum decay and these findings remain consistent even when considering extra dimensions. We also studied the Hawking-Moss transition and found a picture similar to the Einstein case, with one curious five-dimensional exception (due to a mass gap).

Note that the study of bubble nucleation in EGB gravity was presented using the thin wall approximation, in which the vacuum transitions completely and instantaneously across the wall. The thin wall approximation is only a good approximation when the potential barrier is sharp (which might not always be the case in reality, we will discuss it later.). However, it is still applicable to our research as the aim was to investigate the gravitational aspects of the problem, and we do not expect such higher derivative terms to significantly change the discussion for scalar field decay.

In four dimensions, we found as expected that the Gauss-Bonnet term only impacts topology-changing transitions. For example, in bubble nucleation, the GB term does not impact instantons that have both seed and remnant black holes. However, the GB term suppresses the transition (for positive α) when vacuum decay removes the seed black hole altogether. The other possible way is in a transition where a black hole is created. We concluded that only HM transition can result in a geometry with a remnant black hole, and here, the GB term enhances the decay, although the lack of continuity of the action as a function of black hole mass means that an arbitrarily small mass black hole would have the lowest action, likely taking the spacetime outside of the semi-classical regime.

Interestingly, there are problems with generic higher order curvature terms in the action. Without the well-posedness of these Lovelock terms, the higher order derivatives mean that singular instantons cannot be regularised in a well-defined and rigorous manner without UV completion. It is also likely the case that the generalised Birkhoff theorems which specify the form of bubble transitions are no longer applicable in the presence of such terms [244, 245].

7.1.3 The controversy on black hole seeded false vacuum decay

As previously mentioned, the main results related to false vacuum decay in this thesis are under the thin wall approximation. However, for vacuum energy sourced by a scalar field, there is a region around the “wall” where the scalar rolls to its vacuum value and for the important physical application of Higgs vacuum decay, the “wall” is a rather broad scalar distribution around the black hole. On top of this, Strumia [91] has raised a controversial argument on whether black holes can seed vacuum decay. There have been several studies on this problem [109–114], exploring whether thermal fluctuations might stabilize the Higgs potential and thus preclude decay. Qualitative arguments might indicate that tunnelling would be suppressed or removed due to the thermal corrections, however, this is not the full story. Precisely computing the thermal effects, however, is a challenging task as it requires going beyond the saddle point and including not only field theory corrections, but also considering the gravitational aspects of the problem.

Alternately, studies using a Euclidean approach or in lower dimensions, leave a more mixed picture. One problem is that the thermal corrections to the Higgs potential are only part of the question; one has to consider the cosmological setting more holistically to get a physically complete picture. In Chapter 4, we studied vacuum decay within an interstellar medium impacted by the radiation from an evaporating black hole. A hot spot forms, surrounding the primordial black hole, and provides an equilibrium temperature higher than the Universe but lower than the Hawking temperature of the black hole. This gives rise to thermal corrections that tend to suppress decay. Meanwhile, we considered the gravitational aspect, where the conical deficits near the event horizon give an extra contribution to the bubble action. Through our study, we justified the suppression from the thermal corrections is not a complete picture, the importance of how the decay rate changes also depends on the realistic environment as well as the gravitational effects from black holes.

We also reviewed the controversy in the work presented in Chapter 5, although the primary focus is to extract the impact of higher derivative terms. Moving to the higher dimensions and higher curvature gravity, we found interestingly the GB term lowers the temperature of a black hole of a given mass relative to its Einstein value. This would further mitigate any thermal corrections to the Higgs potential, hence lessening the relevance of such corrections. We also note that if there are any couplings of the Higgs to the GB term, then even in 4D, the GB will now acquire some dynamical input into the different decay channels – this is an interesting and open question.

We concluded that there is still a lack of consensus on the precise magnitude of any suppression. The problems are mainly about the choice of vacuum for the Higgs, as well as the validity of calculational methods. In essence, the problem centres around how to correctly incorporate gravity in non-perturbative processes that do not even have experimental verification in the absence of gravity.

7.2 Scattering of dirty black holes

In Chapter 6, we studied the scattering of planar waves incident on a dirty black hole spacetime, that is, a black hole surrounded by a thin shell of matter. There are three different shell configurations with one or two light rings exist in the spacetime, which account for various critical scattering phenomena similar to optical scatterings. We considered cases where the shell contributes substantially to the scattering, thereby complementing the analyses presented in [203, 204]. We focused our attention on the spectrum of resonances of DBHs and calculated the Regge pole spectrum of different DBH configurations.

We identified two key properties of the RP spectrum of DBHs: i) the existence of two branches and ii) the possible existence of a third branch with a nearly constant imaginary part. The first two branches are associated with the inner light-ring and with either the outer light-ring or the shell, depending on the DBH configuration. It appears that the two branches emerge from the original isolated black hole spectrum. The separation from the original branch to the two distinct ones appears first for large overtone numbers while the two branches may overlap for low overtone. The separation is also more prominent for high frequencies and for DBH configuration where the shell contributes significantly. The existence of the two branches results in modulation of the scattering cross section. Such modulations were not seen in previous studies due to the specific DBH configuration considered by the authors.

In addition to these two branches, we have identified a third branch corresponding to broad resonances trapped between the inner light-ring and the thin shell. This interpretation was supported by a WKB analysis of the RP spectrum and is reminiscent of the resonances obtained for compact objects [233, 242, 246].

Building on the identification of the RP spectrum, we constructed the complex angular momentum representation of the scattering. We showed that the RP spectrum and their associated residues accurately describe the scattering cross section, including the modulations and deviations from the case of an isolated black hole. The accurate reconstruction of the scattering cross-section also confirms that the resonances have been correctly identified and further validates our results.

7.3 Future work

As we have studied different aspects of black holes, future research interests can also be divided into two distinct avenues. First, we consider future directions for seeded false vacuum decay. FVD can be triggered by impurities in the early Universe. A black hole is a good candidate as it provides the simplest model, allowing for symmetric and spherical geometries we can play with. However, other defects in the early Universe that act as nucleation sites have their own significance and merit further investigation. The study on domain walls in [74] proposed the possible two-step transition of seeded false vacuum decay: The early stage is the formation of domain walls, which can then act as nucleation sites for the second step of bubble nucleation. They concluded that a seeded phase transition is generically faster than the standard homogeneous rate, and it ultimately determines the way the phase transition is completed.

This seeded phase transition mechanism can be applied to other defects in the same manner, such as monopoles. In monopole-catalysed tunnelling, the first step involves the production of metastable monopoles, followed by the expansion in its core, which resembles the lower energy vacuum state. The number density of monopoles is a key parameter that determines the significance of this decay mechanism. A recent study showed that PBH evaporation heats up the ambient plasma, creating an optimal thermal milieu for intriguing physical processes. Within this hot plasma, monopoles produced via the Kibble-Zurek mechanism are significant [92]. Therefore, we expect that the strategy may be similarly applied to the scenario involving monopoles, which may lead to potentially observable gravitational wave signals.

Another well-motivated and important idea we learned from previous works is to look at the controversy on black hole seeding, as we mentioned in 7.1.3. The decay rate of transition was perceived through the solutions of Euclidean field equations. The semi-analytical description requires the field profiles to have the O(3) or O(4) symmetry. It is difficult to be generalised to its physical application of Higgs decay, where the transition occurs dynamically in a thick-wall region.

The decay rate formula shown in this thesis is essentially calculated at the “one-loop”. One in principle can compute higher-order corrections for more precise results. Recently, a new method using the effective action formalism to obtain higher-order corrections to the decay rate has been developed in [67]. This provides a promising approach to further investigate the significance of the first-order phase transitions in the early Universe. Additionally, incorporating these results with the thermal corrections to the Higgs potential as well as the gravitational field offers an intriguing direction for future exploration.

Regarding the studies of the scattering of dirty black holes. Our study fits into the general goal of modelling and understanding black holes within their environments. We have considered here a toy model of a black hole surrounded by a static and spherically symmetric thin shell of matter. In order to account for even more realistic scenarios, we need to account for asymmetric distributions of matter and take into account the dynamical evolution of the environment. The thin shell model provides only a practical toy model for the latter as the dynamics of the shell can be found exactly. It would be an interesting extension of our work to investigate the resonances of dynamical dirty black holes. Indeed, some literature about resonances of dynamical black holes mostly relies on numerical that still lack a complete theoretical description [247, 248]. The ultimate goal is to apply our toy model to explore the resonances of dynamical dirty black holes. It is a promising and interesting direction for future research.

Another interesting avenue to explore would be the impact of the environment and its dynamics on the resonance spectrum to mimic gravitational effects using condensed matter platforms. This field of research, known as analogue gravity [249], has allowed us to observe and better understand several effects predicted from field theory in curved spacetimes. Recently, analogue simulators have investigated experimentally the ringdown phase of analogue black holes [250], and more experiments are being developed within the Quantum Simulators for Fundamental Physics research programme (https://www.qsimfp.org/). In analogue experiments, environmental and dynamical effects will inherently be present and accurate modelling of their impact will be necessary. These simulators will provide valuable insights to build the necessary tools to describe dynamic dirty black holes.

References

[1] Jacob D. Bekenstein. Black holes and entropy. *Phys. Rev. D*, 7:2333–2346, 1973.

[2] S. W. Hawking. Particle Creation by Black Holes. *Commun. Math. Phys.*, 43:199–220, 1975.

[3] Samir D. Mathur. The Information paradox: A Pedagogical introduction. *Class. Quant. Grav.*, 26:224001, 2009.

[4] Georges Aad et al. Observation of a new particle in the search for the Standard Model Higgs boson with the ATLAS detector at the LHC. *Phys. Lett. B*, 716:1–29, 2012.

[5] Georges Aad et al. Measurements of Higgs boson production and couplings in diboson final states with the ATLAS detector at the LHC. *Phys. Lett. B*, 726:88–119, 2013.

[6] Georges Aad et al. Combined Measurement of the Higgs Boson Mass in pp Collisions at $\sqrt{s} = 7$ and 8 TeV with the ATLAS and CMS Experiments. *Phys. Rev. Lett.*, 114:191803, 2015.

[7] Serguei Chatrchyan et al. Observation of a New Boson at a Mass of 125 GeV with the CMS Experiment at the LHC. *Phys. Lett. B*, 716:30–61, 2012.

[8] Serguei Chatrchyan et al. Measurement of the Properties of a Higgs Boson in the Four-Lepton Final State. *Phys. Rev. D*, 89(9):092007, 2014.

[9] Vardan Khachatryan et al. Measurement of the top quark mass using proton-proton data at $\sqrt{(s)} = 7$ and 8 TeV. *Phys. Rev. D*, 93(7):072004, 2016.

[10] Sidney R. Coleman. The Fate of the False Vacuum. 1. Semiclassical Theory. *Phys. Rev. D*, 15:2929–2936, 1977.

[11] Curtis G. Callan, Jr. and Sidney R. Coleman. The Fate of the False Vacuum. 2. First Quantum Corrections. *Phys. Rev. D*, 16:1762–1768, 1977.

[12] Sidney R. Coleman and Frank De Luccia. Gravitational Effects on and of Vacuum Decay. *Phys. Rev. D*, 21:3305, 1980.

[13] Kazunori Akiyama et al. First M87 Event Horizon Telescope Results. I. The Shadow of the Supermassive Black Hole. *Astrophys. J. Lett.*, 875:L1, 2019.

[14] B. P. Abbott et al. Observation of Gravitational Waves from a Binary Black Hole Merger. *Phys. Rev. Lett.*, 116(6):061102, 2016.

[15] Kenneth W Ford and John A Wheeler. Semiclassical description of scattering. *Annals of Physics*, 7(3):259–286, 1959.

[16] S. W. Hawking. Black hole explosions. *Nature*, 248:30–31, 1974.

[17] A. M. Ghez, B. L. Klein, M. Morris, and E. E. Becklin. High proper motion stars in the vicinity of Sgr A*: Evidence for a supermassive black hole at the center of our galaxy. *Astrophys. J.*, 509:678–686, 1998.

[18] Kazunori Akiyama et al. First Sagittarius A* Event Horizon Telescope Results. I. The Shadow of the Supermassive Black Hole in the Center of the Milky Way. *Astrophys. J. Lett.*, 930(2):L12, 2022.

[19] B. J. Carr and James E. Lidsey. Primordial black holes and generalized constraints on chaotic inflation. *Phys. Rev. D*, 48:543–553, Jul 1993.

[20] P. Ivanov, P. Naselsky, and I. Novikov. Inflation and primordial black holes as dark matter. *Phys. Rev. D*, 50:7173–7178, Dec 1994.

[21] Juan Garcia-Bellido, Andrei D. Linde, and David Wands. Density perturbations and black hole formation in hybrid inflation. *Phys. Rev. D*, 54:6040–6058, 1996.

[22] Dejan Stojkovic and Katherine Freese. A Black hole solution to the cosmological monopole problem. *Phys. Lett. B*, 606:251–257, 2005.

[23] Dejan Stojkovic, Katherine Freese, and Glenn D. Starkman. Holes in the walls: Primordial black holes as a solution to the cosmological domain wall problem. *Phys. Rev. D*, 72:045012, 2005.

[24] George F. Chapline. Cosmological effects of primordial black holes. *Nature*, 253(5489):251–252, 1975.

[25] Bernard Carr, Florian Kuhnel, and Marit Sandstad. Primordial Black Holes as Dark Matter. *Phys. Rev. D*, 94(8):083504, 2016.

[26] Bernard Carr and Florian Kuhnel. Primordial Black Holes as Dark Matter: Recent Developments. *Ann. Rev. Nucl. Part. Sci.*, 70:355–394, 2020.

[27] Misao Sasaki, Teruaki Suyama, Takahiro Tanaka, and Shuichiro Yokoyama. Primordial Black Hole Scenario for the Gravitational-Wave Event GW150914. *Phys. Rev. Lett.*, 117(6):061101, 2016.

[28] Sebastien Clesse and Juan García-Bellido. Seven Hints for Primordial Black Hole Dark Matter. *Phys. Dark Univ.*, 22:137–146, 2018.

[29] Misao Sasaki, Teruaki Suyama, Takahiro Tanaka, and Shuichiro Yokoyama. Primordial black holes—perspectives in gravitational wave astronomy. *Class. Quant. Grav.*, 35(6):063001, 2018.

[30] Simeon Bird, Ilias Cholis, Julian B. Muñoz, Yacine Ali-Haïmoud, Marc Kamionkowski, Ely D. Kovetz, Alvise Raccanelli, and Adam G. Riess. Did LIGO detect dark matter? *Phys. Rev. Lett.*, 116(20):201301, 2016.

[31] Stephen Hawking. Gravitationally collapsed objects of very low mass. *Mon. Not. Roy. Astron. Soc.*, 152:75, 1971.

[32] Bernard J. Carr and S. W. Hawking. Black holes in the early Universe. *Mon. Not. Roy. Astron. Soc.*, 168:399–415, 1974.

[33] Jane H. MacGibbon, Robert H. Brandenberger, and U. F. Wichoski. Limits on black hole formation from cosmic string loops. *Phys. Rev. D*, 57:2158–2165, 1998.

[34] Eric Cotner and Alexander Kusenko. Primordial black holes from supersymmetry in the early universe. *Phys. Rev. Lett.*, 119(3):031103, 2017.

[35] Shi Pi, Ying-li Zhang, Qing-Guo Huang, and Misao Sasaki. Scalaron from R^2-gravity as a heavy field. *JCAP*, 05:042, 2018.

[36] Jing Liu, Ligong Bian, Rong-Gen Cai, Zong-Kuan Guo, and Shao-Jiang Wang. Primordial black hole production during first-order phase transitions. *Phys. Rev. D*, 105(2):L021303, 2022.

[37] C. Brans and R. H. Dicke. Mach's principle and a relativistic theory of gravitation. *Phys. Rev.*, 124:925–935, 1961.

[38] E. S. Fradkin and Mikhail A. Vasiliev. On the Gravitational Interaction of Massless Higher Spin Fields. *Phys. Lett. B*, 189:89–95, 1987.

[39] Constantinos Skordis. The Tensor-Vector-Scalar theory and its cosmology. *Class. Quant. Grav.*, 26:143001, 2009.

[40] J. W. Moffat. Scalar-tensor-vector gravity theory. *JCAP*, 03:004, 2006.

[41] V. A. Rubakov. Large and infinite extra dimensions: An Introduction. *Phys. Usp.*, 44:871–893, 2001.

[42] Lisa Randall and Raman Sundrum. A Large mass hierarchy from a small extra dimension. *Phys. Rev. Lett.*, 83:3370–3373, 1999.

[43] Lisa Randall and Raman Sundrum. An Alternative to compactification. *Phys. Rev. Lett.*, 83:4690–4693, 1999.

[44] D. Lovelock. The Einstein tensor and its generalizations. *J. Math. Phys.*, 12:498–501, 1971.

[45] D. Lovelock. The four-dimensionality of space and the einstein tensor. *J. Math. Phys.*, 13:874–876, 1972.

[46] Antonio De Felice and Shinji Tsujikawa. f(R) theories. *Living Rev. Rel.*, 13:3, 2010.

[47] Shin'ichi Nojiri and Sergei D. Odintsov. Unified cosmic history in modified gravity: from F(R) theory to Lorentz non-invariant models. *Phys. Rept.*, 505:59–144, 2011.

[48] Timothy Clifton, Pedro G. Ferreira, Antonio Padilla, and Constantinos Skordis. Modified Gravity and Cosmology. *Phys. Rept.*, 513:1–189, 2012.

[49] Marek A. Abramowicz and P. Chris Fragile. Foundations of Black Hole Accretion Disk Theory. *Living Rev. Rel.*, 16:1, 2013.

[50] Enrico Barausse, Vitor Cardoso, and Paolo Pani. Can environmental effects spoil precision gravitational-wave astrophysics? *Phys. Rev. D*, 89(10):104059, 2014.

[51] Enrico Barausse, Vitor Cardoso, and Paolo Pani. Environmental Effects for Gravitational-wave Astrophysics. *J. Phys. Conf. Ser.*, 610(1):012044, 2015.

[52] Caio F. B. Macedo, Paolo Pani, Vitor Cardoso, and Luís C. B. Crispino. Into the lair: gravitational-wave signatures of dark matter. *Astrophys. J.*, 774:48, 2013.

[53] Bradley J. Kavanagh, David A. Nichols, Gianfranco Bertone, and Daniele Gaggero. Detecting dark matter around black holes with gravitational waves: Effects of dark-matter dynamics on the gravitational waveform. *Phys. Rev. D*, 102(8):083006, 2020.

[54] Masha Baryakhtar et al. Dark Matter In Extreme Astrophysical Environments. In *2022 Snowmass Summer Study*, 3 2022.

[55] V. V. Kiselev. Quintessential solution of dark matter rotation curves and its simulation by extra dimensions. 3 2003.

[56] Thomas P. Sotiriou and Valerio Faraoni. Black holes in scalar-tensor gravity. *Phys. Rev. Lett.*, 108:081103, 2012.

[57] Sarah Chadburn and Ruth Gregory. Time dependent black holes and scalar hair. *Class. Quant. Grav.*, 31(19):195006, 2014.

[58] Matt Visser. Dirty black holes: Thermodynamics and horizon structure. *Phys. Rev. D*, 46:2445–2451, 1992.

[59] Matt Visser. Dirty black holes: Entropy versus area. *Phys. Rev. D*, 48:583–591, 1993.

[60] Matt Visser. Dirty black holes: Entropy as a surface term. *Phys. Rev. D*, 48:5697–5705, 1993.

[61] David J. Griffiths and Darrell F. Schroeter. *Introduction to quantum mechanics*. Cambridge University Press, Cambridge ; New York, NY, third edition edition, 2018.

[62] Sidney Coleman. *Aspects of Symmetry: Selected Erice Lectures*. Cambridge University Press, Cambridge, U.K., 1985.

[63] Jean-Loup Gervais and B. Sakita. Extended Particles in Quantum Field Theories. *Phys. Rev. D*, 11:2943, 1975.

[64] Anders Andreassen, David Farhi, William Frost, and Matthew D. Schwartz. Precision decay rate calculations in quantum field theory. *Phys. Rev. D*, 95(8):085011, 2017.

[65] Wen-Yuan Ai, Björn Garbrecht, and Carlos Tamarit. Functional methods for false vacuum decay in real time. *JHEP*, 12:095, 2019.

[66] R. Jackiw. Functional evaluation of the effective potential. *Phys. Rev. D*, 9:1686, 1974.

[67] Wen-Yuan Ai, Jean Alexandre, and Sarben Sarkar. False vacuum decay rates, more precisely. *Phys. Rev. D*, 109(4):045010, 2024.

[68] W. Israel. Singular hypersurfaces and thin shells in general relativity. *Nuovo Cim. B*, 44S10:1, 1966.

[69] Naritaka Oshita, Masaki Yamada, and Masahide Yamaguchi. Compact objects as the catalysts for vacuum decays. *Phys. Lett. B*, 791:149–155, 2019.

[70] Reuven Balkin, Javi Serra, Konstantin Springmann, Stefan Stelzl, and Andreas Weiler. Density induced vacuum instability. *SciPost Phys.*, 14(4):071, 2023.

[71] U. A. Yajnik. PHASE TRANSITION INDUCED BY COSMIC STRINGS. *Phys. Rev. D*, 34:1237–1240, 1986.

[72] U. A. Yajnik and T. Padmanabhan. ANALYTICAL APPROACH TO STRING INDUCED PHASE TRANSITION. *Phys. Rev. D*, 35:3100, 1987.

[73] Bum-Hoon Lee, Wonwoo Lee, Richard MacKenzie, M. B. Paranjape, U. A. Yajnik, and Dong-han Yeom. Battle of the bulge: Decay of the thin, false cosmic string. *Phys. Rev. D*, 88(10):105008, 2013.

[74] Simone Blasi and Alberto Mariotti. Domain Walls Seeding the Electroweak Phase Transition. *Phys. Rev. Lett.*, 129(26):261303, 2022.

[75] Paul Joseph Steinhardt. Monopole and Vortex Dissociation and Decay of the False Vacuum. *Nucl. Phys. B*, 190:583–616, 1981.

[76] Brijesh Kumar and Urjit Yajnik. Graceful exit via monopoles in a theory with O'Raifeartaigh type supersymmetry breaking. *Nucl. Phys. B*, 831:162–177, 2010.

[77] Brijesh Kumar, M. B. Paranjape, and U. A. Yajnik. Fate of the false monopoles: Induced vacuum decay. *Phys. Rev. D*, 82:025022, 2010.

[78] Prateek Agrawal and Michael Nee. The Boring Monopole. *SciPost Phys.*, 13(3):049, 2022.

[79] Ruth Gregory, Ian G. Moss, and Benjamin Withers. Black holes as bubble nucleation sites. *JHEP*, 03:081, 2014.

[80] Philipp Burda, Ruth Gregory, and Ian Moss. Vacuum metastability with black holes. *JHEP*, 08:114, 2015.

[81] Philipp Burda, Ruth Gregory, and Ian Moss. Gravity and the stability of the Higgs vacuum. *Phys. Rev. Lett.*, 115:071303, 2015.

[82] Philipp Burda, Ruth Gregory, and Ian Moss. The fate of the Higgs vacuum. *JHEP*, 06:025, 2016.

[83] Peter Bowcock, Christos Charmousis, and Ruth Gregory. General brane cosmologies and their global space-time structure. *Class. Quant. Grav.*, 17:4745–4764, 2000.

[84] S. W. Hawking and I. G. Moss. Supercooled Phase Transitions in the Very Early Universe. *Phys. Lett. B*, 110:35–38, 1982.

[85] Ruth Gregory, Ian G. Moss, and Naritaka Oshita. Black Holes, Oscillating Instantons, and the Hawking-Moss transition. *JHEP*, 07:024, 2020.

[86] Ruth Gregory, Ian G. Moss, Naritaka Oshita, and Sam Patrick. Hawking-Moss transition with a black hole seed. *JHEP*, 09:135, 2020.

[87] Louis Hamaide, Lucien Heurtier, Shi-Qian Hu, and Andrew Cheek. Primordial black holes are true vacuum nurseries. *Phys. Lett. B*, 856:138895, 2024.

[88] Don N. Page. Particle Emission Rates from a Black Hole: Massless Particles from an Uncharged, Nonrotating Hole. *Phys. Rev. D*, 13:198–206, 1976.

[89] J. B. Hartle and S. W. Hawking. Path Integral Derivation of Black Hole Radiance. *Phys. Rev. D*, 13:2188–2203, 1976.

[90] W. G. Unruh. Notes on black hole evaporation. *Phys. Rev. D*, 14:870, 1976.

[91] Alessandro Strumia. Black holes don't source fast Higgs vacuum decay. *JHEP*, 03:039, 2023.

[92] Saurav Das and Anson Hook. Black hole production of monopoles in the early universe. *JHEP*, 12:145, 2021.

[93] Minxi He, Kazunori Kohri, Kyohei Mukaida, and Masaki Yamada. Formation of hot spots around small primordial black holes. *JCAP*, 01:027, 2023.

[94] De-Chang Dai, Ruth Gregory, and Dejan Stojkovic. Connecting the Higgs Potential and Primordial Black Holes. *Phys. Rev. D*, 101(12):125012, 2020.

[95] J. H. MacGibbon and B. R. Webber. Quark and gluon jet emission from primordial black holes: The instantaneous spectra. *Phys. Rev. D*, 41:3052–3079, 1990.

[96] Jane H. MacGibbon. Quark and gluon jet emission from primordial black holes. 2. The Lifetime emission. *Phys. Rev. D*, 44:376–392, 1991.

[97] Andrei D. Linde. Fate of the False Vacuum at Finite Temperature: Theory and Applications. *Phys. Lett. B*, 100:37–40, 1981.

[98] Ian Affleck. Quantum Statistical Metastability. *Phys. Rev. Lett.*, 46:388, 1981.

[99] Armen Tumasyan et al. Measurement of the top quark mass using a profile likelihood approach with the lepton + jets final states in proton–proton collisions at $\sqrt{s} = 13\,\text{TeV}$. *Eur. Phys. J. C*, 83(10):963, 2023.

[100] Colin Poole and Anders Eller Thomsen. Constraints on 3- and 4-loop β-functions in a general four-dimensional Quantum Field Theory. *JHEP*, 09:055, 2019.

[101] Lohan Sartore and Ingo Schienbein. PyR@TE 3. *Comput. Phys. Commun.*, 261:107819, 2021.

[102] Giuseppe Degrassi. The role of the top quark in the stability of the SM Higgs potential. *Nuovo Cim. C*, 037(02):47–53, 2014.

[103] S. Alekhin, A. Djouadi, and S. Moch. The top quark and Higgs boson masses and the stability of the electroweak vacuum. *Phys. Lett. B*, 716:214–219, 2012.

[104] Jose R. Espinosa, Gian F. Giudice, Enrico Morgante, Antonio Riotto, Leonardo Senatore, Alessandro Strumia, and Nikolaos Tetradis. The cosmological Higgstory of the vacuum instability. *JHEP*, 09:174, 2015.

[105] Dario Buttazzo, Giuseppe Degrassi, Pier Paolo Giardino, Gian F. Giudice, Filippo Sala, Alberto Salvio, and Alessandro Strumia. Investigating the near-criticality of the Higgs boson. *JHEP*, 12:089, 2013.

[106] Bernard J. Carr. The Primordial black hole mass spectrum. *Astrophys. J.*, 201:1–19, 1975.

[107] B. J. Carr, Kazunori Kohri, Yuuiti Sendouda, and Jun'ichi Yokoyama. New cosmological constraints on primordial black holes. *Phys. Rev. D*, 81:104019, 2010.

[108] Bernard Carr, Kazunori Kohri, Yuuiti Sendouda, and Jun'ichi Yokoyama. Constraints on primordial black holes. *Rept. Prog. Phys.*, 84(11):116902, 2021.

[109] Takumi Hayashi, Kohei Kamada, Naritaka Oshita, and Jun'ichi Yokoyama. On catalyzed vacuum decay around a radiating black hole and the crisis of the electroweak vacuum. *JHEP*, 08:088, 2020.

[110] Andrey Shkerin and Sergey Sibiryakov. Black hole induced false vacuum decay from first principles. *JHEP*, 11:197, 2021.

[111] Vadim Briaud, Andrey Shkerin, and Sergey Sibiryakov. Thermal false vacuum decay around black holes. *Phys. Rev. D*, 106(12):125001, 2022.

[112] Andrey Shkerin and Sergey Sibiryakov. Black hole induced false vacuum decay: the role of greybody factors. *JHEP*, 08:161, 2022.

[113] Taiga Miyachi and Jiro Soda. False vacuum decay in a two-dimensional black hole spacetime. *Phys. Rev. D*, 103(8):085009, 2021.

[114] Kazunori Kohri and Hiroki Matsui. Electroweak Vacuum Collapse induced by Vacuum Fluctuations of the Higgs Field around Evaporating Black Holes. *Phys. Rev. D*, 98(12):123509, 2018.

[115] Keisuke Inomata, Masahiro Kawasaki, Kyohei Mukaida, Takahiro Terada, and Tsutomu T. Yanagida. Gravitational Wave Production right after a Primordial Black Hole Evaporation. *Phys. Rev. D*, 101(12):123533, 2020.

[116] Basabendu Barman, Debasish Borah, Suruj Jyoti Das, and Rishav Roshan. Gravitational wave signatures of a PBH-generated baryon-dark matter coincidence. *Phys. Rev. D*, 107(9):095002, 2023.

[117] Nilanjandev Bhaumik, Anish Ghoshal, Rajeev Kumar Jain, and Marek Lewicki. Distinct signatures of spinning PBH domination and evaporation: doubly peaked gravitational waves, dark relics and CMB complementarity. *JHEP*, 05:169, 2023.

[118] Logan Morrison, Stefano Profumo, and Yan Yu. Melanopogenesis: Dark Matter of (almost) any Mass and Baryonic Matter from the Evaporation of Primordial Black Holes weighing a Ton (or less). *JCAP*, 1905:005, 2019.

[119] Paolo Gondolo, Pearl Sandick, and Barmak Shams Es Haghi. Effects of primordial black holes on dark matter models. *Phys. Rev. D*, 102(9):095018, 2020.

[120] Nicolás Bernal and Óscar Zapata. Gravitational dark matter production: primordial black holes and UV freeze-in. *Phys. Lett. B*, 815:136129, 2021.

[121] Suruj Jyoti Das, Devabrat Mahanta, and Debasish Borah. Low scale leptogenesis and dark matter in the presence of primordial black holes. *JCAP*, 11:019, 2021.

[122] Yuta Hamada and Satoshi Iso. Baryon asymmetry from primordial black holes. *PTEP*, 2017(3):033B02, 2017.

[123] Dan Hooper and Gordan Krnjaic. GUT Baryogenesis With Primordial Black Holes. *Phys. Rev. D*, 103(4):043504, 2021.

[124] A. Chaudhuri and A. Dolgov. PBH Evaporation, Baryon Asymmetry, and Dark Matter. *J. Exp. Theor. Phys.*, 133(5):552–566, 2021.

[125] Teruyuki Kitabayashi. Primordial black holes and scotogenic dark matter. *Int. J. Mod. Phys. A*, 36(18):2150139, 2021.

[126] Andrew Cheek, Lucien Heurtier, Yuber F. Perez-Gonzalez, and Jessica Turner. Primordial black hole evaporation and dark matter production. I. Solely Hawking radiation. *Phys. Rev. D*, 105(1):015022, 2022.

[127] Jérôme Martin, Theodoros Papanikolaou, and Vincent Vennin. Primordial black holes from the preheating instability in single-field inflation. *JCAP*, 01:024, 2020.

[128] Jérôme Martin, Theodoros Papanikolaou, Lucas Pinol, and Vincent Vennin. Metric preheating and radiative decay in single-field inflation. *JCAP*, 05:003, 2020.

[129] Pierre Auclair and Vincent Vennin. Primordial black holes from metric preheating: mass fraction in the excursion-set approach. *JCAP*, 02:038, 2021.

[130] Andrew Cheek, Lucien Heurtier, Yuber F. Perez-Gonzalez, and Jessica Turner. Redshift effects in particle production from Kerr primordial black holes. *Phys. Rev. D*, 106(10):103012, 2022.

[131] Dan Hooper, Gordan Krnjaic, and Samuel D. McDermott. Dark Radiation and Superheavy Dark Matter from Black Hole Domination. *JHEP*, 08:001, 2019.

[132] Andrew Cheek, Lucien Heurtier, Yuber F. Perez-Gonzalez, and Jessica Turner. Primordial black hole evaporation and dark matter production. II. Interplay with the freeze-in or freeze-out mechanism. *Phys. Rev. D*, 105(1):015023, 2022.

[133] Yuber F. Perez-Gonzalez and Jessica Turner. Assessing the tension between a black hole dominated early universe and leptogenesis. *Phys. Rev. D*, 104(10):103021, 2021.

[134] Nicolás Bernal and Óscar Zapata. Self-interacting Dark Matter from Primordial Black Holes. *JCAP*, 03:007, 2021.

[135] Satyabrata Datta, Ambar Ghosal, and Rome Samanta. Baryogenesis from ultralight primordial black holes and strong gravitational waves from cosmic strings. *JCAP*, 08:021, 2021.

[136] Isabella Masina. Dark Matter and Dark Radiation from Evaporating Kerr Primordial Black Holes. *Grav. Cosmol.*, 27(4):315–330, 2021.

[137] Nicolás Bernal and Óscar Zapata. Dark Matter in the Time of Primordial Black Holes. *JCAP*, 03:015, 2021.

[138] Iason Baldes, Quentin Decant, Deanna C. Hooper, and Laura Lopez-Honorez. Non-Cold Dark Matter from Primordial Black Hole Evaporation. *JCAP*, 08:045, 2020.

[139] Rouzbeh Allahverdi, James Dent, and Jacek Osinski. Nonthermal production of dark matter from primordial black holes. *Phys. Rev.*, D97(5):055013, 2018.

[140] Isabella Masina. Dark matter and dark radiation from evaporating primordial black holes. *Eur. Phys. J. Plus*, 135(7):552, 2020.

[141] Cecilia Lunardini and Yuber F Perez-Gonzalez. Dirac and Majorana Neutrino Signatures of Primordial Black Holes. *JCAP*, 08:014, 2020.

[142] Keith R. Dienes, Lucien Heurtier, Fei Huang, Doojin Kim, Tim M. P. Tait, and Brooks Thomas. Primordial Black Holes Place the Universe in Stasis. 12 2022.

[143] Theodoros Papanikolaou. Gravitational waves induced from primordial black hole fluctuations: the effect of an extended mass function. *JCAP*, 10:089, 2022.

[144] Ryo Saito and Jun'ichi Yokoyama. Gravitational wave background as a probe of the primordial black hole abundance. *Phys. Rev. Lett.*, 102:161101, 2009.

[145] Md Riajul Haque, Essodjolo Kpatcha, Debaprasad Maity, and Yann Mambrini. Primordial Black Hole versus Inflaton: Two Chief Systems of the World. 9 2023.

[146] Md Riajul Haque, Essodjolo Kpatcha, Debaprasad Maity, and Yann Mambrini. Primordial black hole reheating. *Phys. Rev. D*, 108(6):063523, 2023.

[147] Ruth Gregory and Shi-Qian Hu. Seeded vacuum decay with Gauss-Bonnet. *JHEP*, 11:072, 2023.

[148] Ruth Gregory and Shi-Qian Hu. Testing Higher Derivative Gravity through Tunnelling. *Particles*, 7(1):144–160, 2024.

[149] T. Padmanabhan and D. Kothawala. Lanczos-Lovelock models of gravity. *Phys. Rept.*, 531:115–171, 2013.

[150] Cornelius Lanczos. A Remarkable property of the Riemann-Christoffel tensor in four dimensions. *Annals Math.*, 39:842–850, 1938.

[151] Bruno Zumino. Gravity Theories in More Than Four-Dimensions. *Phys. Rept.*, 137:109, 1986.

[152] Barton Zwiebach. Curvature Squared Terms and String Theories. *Phys. Lett. B*, 156:315–317, 1985.

[153] David G. Boulware and Stanley Deser. String Generated Gravity Models. *Phys. Rev. Lett.*, 55:2656, 1985.

[154] Dražen Glavan and Chunshan Lin. Einstein-Gauss-Bonnet Gravity in Four-Dimensional Spacetime. *Phys. Rev. Lett.*, 124(8):081301, 2020.

[155] Julio Arrechea, Adrià Delhom, and Alejandro Jiménez-Cano. Comment on "Einstein-Gauss-Bonnet Gravity in Four-Dimensional Spacetime". *Phys. Rev. Lett.*, 125(14):149002, 2020.

[156] Metin Gurses, Tahsin Çağrı Şişman, and Bayram Tekin. Comment on ”Einstein-Gauss-Bonnet Gravity in 4-Dimensional Space-Time”. *Phys. Rev. Lett.*, 125(14):149001, 2020.

[157] Wen-Yuan Ai. A note on the novel 4D Einstein–Gauss–Bonnet gravity. *Commun. Theor. Phys.*, 72(9):095402, 2020.

[158] Pedro G. S. Fernandes, Pedro Carrilho, Timothy Clifton, and David J. Mulryne. Derivation of Regularized Field Equations for the Einstein-Gauss-Bonnet Theory in Four Dimensions. *Phys. Rev. D*, 102(2):024025, 2020.

[159] H. Lu and Yi Pang. Horndeski gravity as $D \to 4$ limit of Gauss-Bonnet. *Phys. Lett. B*, 809:135717, 2020.

[160] Pedro G. S. Fernandes, Pedro Carrilho, Timothy Clifton, and David J. Mulryne. The 4D Einstein–Gauss–Bonnet theory of gravity: a review. *Class. Quant. Grav.*, 39(6):063001, 2022.

[161] Robert C. Myers and M. J. Perry. Black Holes in Higher Dimensional Space-Times. *Annals Phys.*, 172:304, 1986.

[162] Robert C. Myers. Higher Derivative Gravity, Surface Terms and String Theory. *Phys. Rev. D*, 36:392, 1987.

[163] Robert C. Myers and Jonathan Z. Simon. Black Hole Thermodynamics in Lovelock Gravity. *Phys. Rev. D*, 38:2434–2444, 1988.

[164] James T. Wheeler. Symmetric Solutions to the Gauss-Bonnet Extended Einstein Equations. *Nucl. Phys. B*, 268:737–746, 1986.

[165] James T. Wheeler. Symmetric Solutions to the Maximally Gauss-Bonnet Extended Einstein Equations. *Nucl. Phys. B*, 273:732–748, 1986.

[166] Christos Charmousis and Antonio Padilla. The Instability of Vacua in Gauss-Bonnet Gravity. *JHEP*, 12:038, 2008.

[167] D. L. Wiltshire. Spherically Symmetric Solutions of Einstein-maxwell Theory With a Gauss-Bonnet Term. *Phys. Lett. B*, 169:36–40, 1986.

[168] Christos Charmousis and Jean-Francois Dufaux. General Gauss-Bonnet brane cosmology. *Class. Quant. Grav.*, 19:4671–4682, 2002.

[169] Charalampos Bogdanos. Extensions of Birkhoff’s Theorem in 6D Gauss-Bonnet Gravity. In Jean-Michel Alimi and André Fuözfa, editors, *Invisible Universe*, volume 1241 of *American Institute of Physics Conference Series*, pages 521–527, June 2010.

[170] Stephen C. Davis. Generalized Israel junction conditions for a Gauss-Bonnet brane world. *Phys. Rev. D*, 67:024030, 2003.

[171] Yves Brihaye and Eugen Radu. Black objects in the Einstein-Gauss-Bonnet theory with negative cosmological constant and the boundary counterterm method. *JHEP*, 09:006, 2008.

[172] Yves Brihaye and Eugen Radu. Einstein-Gauss-Bonnet black holes in de Sitter spacetime and the quasilocal formalism. *Phys. Lett. B*, 678:204–212, 2009.

[173] James T. Liu and Wafic A. Sabra. Hamilton-Jacobi Counterterms for Einstein-Gauss-Bonnet Gravity. *Class. Quant. Grav.*, 27:175014, 2010.

[174] G. W. Gibbons and S. W. Hawking. Classification of Gravitational Instanton Symmetries. *Commun. Math. Phys.*, 66:291–310, 1979.

[175] N. Deppe, C. D. Leonard, T. Taves, G. Kunstatter, and R. B. Mann. Critical Collapse in Einstein-Gauss-Bonnet Gravity in Five and Six Dimensions. *Phys. Rev. D*, 86:104011, 2012.

[176] Nils Deppe, Allison Kolly, Andrew Frey, and Gabor Kunstatter. Stability of anti–de sitter space in einstein-gauss-bonnet gravity. *Phys. Rev. Lett.*, 114:071102, Feb 2015.

[177] Valeri P. Frolov. Mass-gap for black hole formation in higher derivative and ghost free gravity. *Phys. Rev. Lett.*, 115(5):051102, 2015.

[178] Rong-Gen Cai. Gauss-Bonnet black holes in AdS spaces. *Phys. Rev. D*, 65:084014, 2002.

[179] Chen-Hao Wu, Ya-Peng Hu, and Hao Xu. Hawking evaporation of Einstein–Gauss–Bonnet AdS black holes in $D \geqslant 4$ dimensions. *Eur. Phys. J. C*, 81(4):351, 2021.

[180] Hidekazu Nariai. On some static solutions of einstein's gravitational field equations in a spherically symmetric case. *Sci. Rep. Tohoku Univ. Eighth Ser.*, 34:160, 1950.

[181] Hidekazu Nariai. On a new cosmological solution of einstein's field equations of gravitation. *General Relativity and Gravitation*, 31:963–971, 1951.

[182] Edward Witten. (2+1)-Dimensional Gravity as an Exactly Soluble System. *Nucl. Phys. B*, 311:46, 1988.

[183] Maximo Banados, Claudio Teitelboim, and Jorge Zanelli. The Black hole in three-dimensional space-time. *Phys. Rev. Lett.*, 69:1849–1851, 1992.

[184] Tim Clunan, Simon F. Ross, and Douglas J. Smith. On Gauss-Bonnet black hole entropy. *Class. Quant. Grav.*, 21:3447–3458, 2004.

[185] Theo Torres, Mohamed Ould El Hadj, Shi-Qian Hu, and Ruth Gregory. Regge pole description of scattering by dirty black holes. *Phys. Rev. D*, 107(6):064028, 2023.

[186] J. A. H. Futterman, F. A. Handler, and R. A. Matzner. *SCATTERING FROM BLACK HOLES*. Cambridge Monographs on Mathematical Physics. Cambridge University Press, 5 2012.

[187] Norma G. Sanchez. Absorption and Emission Spectra of a Schwarzschild Black Hole. *Phys. Rev. D*, 18:1030, 1978.

[188] Chris Doran, Anthony Lasenby, Sam Dolan, and Ian Hinder. Fermion absorption cross section of a Schwarzschild black hole. *Phys. Rev. D*, 71:124020, 2005.

[189] Luis C. B. Crispino and Ednilton S. Oliveira. Electromagnetic absorption cross section of Reissner-Nordstrom black holes. *Phys. Rev. D*, 78:024011, 2008.

[190] Luis C. B. Crispino, Sam R. Dolan, and Ednilton S. Oliveira. Scattering of massless scalar waves by Reissner-Nordström black holes. *Phys. Rev. D*, 79:064022, 2009.

[191] Sam R. Dolan. Scattering and Absorption of Gravitational Plane Waves by Rotating Black Holes. *Class. Quant. Grav.*, 25:235002, 2008.

[192] Vitor Cardoso and Francisco Duque. Environmental effects in gravitational-wave physics: Tidal deformability of black holes immersed in matter. *Phys. Rev. D*, 101(6):064028, 2020.

[193] Vitor Cardoso, Kyriakos Destounis, Francisco Duque, Rodrigo Panosso Macedo, and Andrea Maselli. Black holes in galaxies: Environmental impact on gravitational-wave generation and propagation. *Phys. Rev. D*, 105(6):L061501, 2022.

[194] J. David Brown and Viqar Husain. Black holes with short hair. *Int. J. Mod. Phys. D*, 6:563–573, 1997.

[195] Shijun Yoshida and Toshifumi Futamase. Numerical analysis of quasinormal modes in nearly extremal Schwarzschild-de Sitter space-times. *Phys. Rev. D*, 69:064025, 2004.

[196] Paolo Pani, Emanuele Berti, Vitor Cardoso, Yanbei Chen, and Richard Norte. Gravitational wave signatures of the absence of an event horizon. I. Nonradial oscillations of a thin-shell gravastar. *Phys. Rev. D*, 80:124047, 2009.

[197] José Luis Jaramillo, Rodrigo Panosso Macedo, and Lamis Al Sheikh. Pseudospectrum and black hole quasinormal mode instability. *Phys. Rev. X*, 11:031003, Jul 2021.

[198] José Luis Jaramillo, Rodrigo Panosso Macedo, and Lamis Al Sheikh. Gravitational wave signatures of black hole quasinormal mode instability. *Phys. Rev. Lett.*, 128:211102, May 2022.

[199] A. J. M. Medved, Damien Martin, and Matt Visser. Dirty black holes: Quasinormal modes. *Class. Quant. Grav.*, 21:1393–1406, 2004.

[200] A. J. M. Medved, Damien Martin, and Matt Visser. Dirty black holes: Quasinormal modes for 'squeezed' horizons. *Class. Quant. Grav.*, 21:2393–2405, 2004.

[201] P. T. Leung, Y. T. Liu, W. M. Suen, C. Y. Tam, and K. Young. Quasinormal modes of dirty black holes. *Phys. Rev. Lett.*, 78:2894–2897, 1997.

[202] P. T. Leung, Y. T. Liu, W. M. Suen, C. Y. Tam, and K. Young. Perturbative approach to the quasinormal modes of dirty black holes. *Phys. Rev. D*, 59:044034, 1999.

[203] Caio F. B. Macedo, Luiz C. S. Leite, and Luís C. B. Crispino. Absorption by dirty black holes: null geodesics and scalar waves. *Phys. Rev. D*, 93(2):024027, 2016.

[204] Luiz C. S. Leite, Caio F. B. Macedo, and Luís C. B. Crispino. Black holes with surrounding matter and rainbow scattering. *Phys. Rev. D*, 99(6):064020, 2019.

[205] V. de Alfaro and T. Regge. *Potential Scattering*. North-Holland Publishing Company, Amsterdam, 1965.

[206] R. G. Newton. *Scattering Theory of Waves and Particles*. Springer-Verlag, New York, second edition, 1982.

[207] George Neville Watson and John William Nicholson. The diffraction of electric waves by the earth. *Proceedings of the Royal Society of London. Series A, Containing Papers of a Mathematical and Physical Character*, 95(666):83–99, 1918.

[208] A. Sommerfeld. *Partial Differential Equations of Physics*. Academic Press, New York, 1949.

[209] Herch Moysés Nussenzveig. *Diffraction effects in semiclassical scattering*, volume 1. Cambridge University Press, 2006.

[210] W. T. Grandy. *Scattering of Waves from Large Spheres*. Cambridge University Press, Cambridge, 2000.

[211] H. Überall. *Acoustic Resonance Scattering*. Gordon and Breach, New York, 1992.

[212] K. Aki and P. Richards. *Quantitative Seismology*. University Science Book, Sausalito, second edition, 2002.

[213] V. N. Gribov. *The Theory of Complex Angular Momenta: Gribov Lectures on Theoretical Physics*. Cambridge University Press, Cambridge, 2003.

[214] P. D. B. Collins. *An Introduction to Regge Theory and High-Energy Physics*. Cambridge University Press, Cambridge, 1977.

[215] V. Barone and E. Predazzi. *High-Energy Particle Diffraction*. Springer-Verlag, Berlin, 2002.

[216] S. Donnachie, G. Dosch, P. V. Landshoff, and O. Nachtmann. *Pomeron Physics and QCD*. Cambridge University Press, Cambridge, 2005.

[217] Nils Andersson and Karl-Erik Thylwe. Complex angular momentum approach to black-hole scattering. *Classical and Quantum Gravity*, 11(12):2991–3001, dec 1994.

[218] Nils Andersson. Complex angular momenta and the black-hole glory. *Classical and Quantum Gravity*, 11(12):3003–3012, dec 1994.

[219] Yves Decanini, Antoine Folacci, and Bruce Jensen. Complex angular momentum in black hole physics and the quasinormal modes. *Phys. Rev. D*, 67:124017, 2003.

[220] Yves Decanini, Gilles Esposito-Farese, and Antoine Folacci. Universality of high-energy absorption cross sections for black holes. *Phys. Rev.*, D83:044032, 2011.

[221] A. Folacci and M. Ould El Hadj. Alternative description of gravitational radiation from black holes based on the Regge poles of the S-matrix and the associated residues. *Phys. Rev. D*, 98(6):064052, 2018.

[222] Antoine Folacci and Mohamed Ould El Hadj. Regge pole description of scattering of scalar and electromagnetic waves by a Schwarzschild black hole. *Phys. Rev. D*, 99(10):104079, 2019.

[223] Antoine Folacci and Mohamed Ould El Hadj. Regge pole description of scattering of gravitational waves by a Schwarzschild black hole. *Phys. Rev.*, D100:064009, 2019.

[224] Vitor Cardoso, Alex S. Miranda, Emanuele Berti, Helvi Witek, and Vilson T. Zanchin. Geodesic stability, Lyapunov exponents and quasinormal modes. *Phys. Rev. D*, 79(6):064016, 2009.

[225] Gaurav Khanna and Richard H. Price. Black Hole Ringing, Quasinormal Modes, and Light Rings. *Phys. Rev. D*, 95(8):081501, 2017.

[226] P A Collins, R Delbourgo, and R M Williams. On the elastic schwarzschild scattering cross section. *Journal of Physics A: Mathematical, Nuclear and General*, 6(2):161, feb 1973.

[227] John A. Adam. The mathematical physics of rainbows and glories. *Physics Reports*, 356(4):229–365, 2002.

[228] Sam R. Dolan and Tom Stratton. Rainbow scattering in the gravitational field of a compact object. *Phys. Rev. D*, 95(12):124055, 2017.

[229] Theo Torres, Max Lloyd, Sam R. Dolan, and Silke Weinfurtner. Wave focusing by submerged islands and gravitational analogues. *Phys. Rev. Res.*, 4(3):033210, 2022.

[230] Nils Andersson and Bruce P. Jensen. Scattering by black holes. Chapter 0.1. pages 1607–1626, 11 2000.

[231] H. M. Nussenzveig. *Diffraction Effects in Semiclassical Scattering*. Cambridge University Press, Cambridge, 1992.

[232] H. M. Nussenzveig. Highâ frequency scattering by a transparent sphere. i. direct reflection and transmission. *Journal of Mathematical Physics*, 10(1):82–124, 1969.

[233] Mohamed Ould El Hadj, Tom Stratton, and Sam R. Dolan. Scattering from compact objects: Regge poles and the complex angular momentum method. *Phys. Rev. D*, 101(10):104035, 2020.

[234] E. W. Leaver. An Analytic representation for the quasi normal modes of Kerr black holes. *Proc. Roy. Soc. Lond. A*, 402:285–298, 1985.

[235] Edward W Leaver. Solutions to a generalized spheroidal wave equation: Teukolsky's equations in general relativity, and the two-center problem in molecular quantum mechanics. *Journal of mathematical physics*, 27(5):1238–1265, 1986.

[236] Omar Benhar, Emanuele Berti, and Valeria Ferrari. The Imprint of the equation of state on the axial w modes of oscillating neutron stars. *Mon. Not. Roy. Astron. Soc.*, 310:797–803, 1999.

[237] B. Majumdar and N. Panchapakesan. Schwarzschild black-hole normal modes using the Hill determinant. *Phys. Rev. D*, 40:2568, 1989.

[238] Yves Décanini and Antoine Folacci. Regge poles of the schwarzschild black hole: A wkb approach. *Phys. Rev. D*, 81:024031, Jan 2010.

[239] Herch Moysés Nussenzveig. *Diffraction effects in semiclassical scattering*. Number 1. Cambridge University Press, 2006.

[240] M V Berry and K E Mount. Semiclassical approximations in wave mechanics. *Reports on Progress in Physics*, 35(1):315–397, jan 1972.

[241] M V Berry. Semiclassically weak reflections above analytic and non-analytic potential barriers. *Journal of Physics A: Mathematical and General*, 15(12):3693–3704, dec 1982.

[242] Y. J. Zhang, J. Wu, and P. T. Leung. High-frequency behavior of w-mode pulsations of compact stars. *Phys. Rev. D*, 83:064012, 2011.

[243] M. Abramowitz and I. A. Stegun. *Handbook of Mathematical Functions*. Dover, New-York, 1965.

[244] Julio Oliva and Sourya Ray. Birkhoff's Theorem in Higher Derivative Theories of Gravity. *Class. Quant. Grav.*, 28:175007, 2011.

[245] Julio Oliva and Sourya Ray. Birkhoff's Theorem in Higher Derivative Theories of Gravity II. *Phys. Rev. D*, 86:084014, 2012.

[246] Sebastian H Völkel and Kostas D Kokkotas. On the inverse spectrum problem of neutron stars. *Classical and Quantum Gravity*, 36(11):115002, may 2019.

[247] Elcio Abdalla, Cecilia B. M. H. Chirenti, and Alberto Saa. Quasinormal modes for the Vaidya metric. *Phys. Rev. D*, 74:084029, 2006.

[248] Cecilia Chirenti and Alberto Saa. Quasinormal modes for the charged Vaidya metric. *J. Phys. Conf. Ser.*, 314:012086, 2011.

[249] W. G. Unruh. Experimental black hole evaporation. *Phys. Rev. Lett.*, 46:1351–1353, 1981.

[250] Theo Torres, Sam Patrick, Maurício Richartz, and Silke Weinfurtner. Quasinormal mode oscillations in an analogue black hole experiment. *Phys. Rev. Lett.*, 125(1):011301, 2020.

[251] David J. Griffiths and Darrell F. Schroeter. *Introduction to Quantum Mechanics*. Cambridge University Press, 3 edition, 2018.

Appendix A

WKB approximation

The WKB method is a practical means of approximating solutions to the Schrödinger equation and is excellent as a conceptual framework for understanding quantum tunnelling problems. In this appendix, we show how to compute the tunnelling rate by using the Wentzel-Kramers-Brillouin (WKB) approximation. We refer to [251] for more detailed derivation. Considering a particle moving in a potential barrier with width a, as sketched in Fig. A.1. The particle has total energy E and potential energy $U(x)$, the time-independent Schrödinger equation is

$$-\frac{\hbar^2}{2m}\frac{d^2\psi}{dx^2} + U(x)\psi = E\psi. \tag{A.1}$$

The wave function solution of the Schrödinger equation can be written as

$$\psi(x) = Ae^{\pm i\omega x} \tag{A.2}$$

where $\omega(x) = \sqrt{2m[E - U(x)]}$.

Let's consider the first case with $E > U(x)$, both ω is real. We propose a generic wave function that takes the form of $\psi(x) = A(x)e^{i\phi(x)}$, we have

$$\frac{d^2\psi}{dx^2} = [A'' + 2iA'\phi' + iA\phi'' - A(\phi')^2]. \tag{A.3}$$

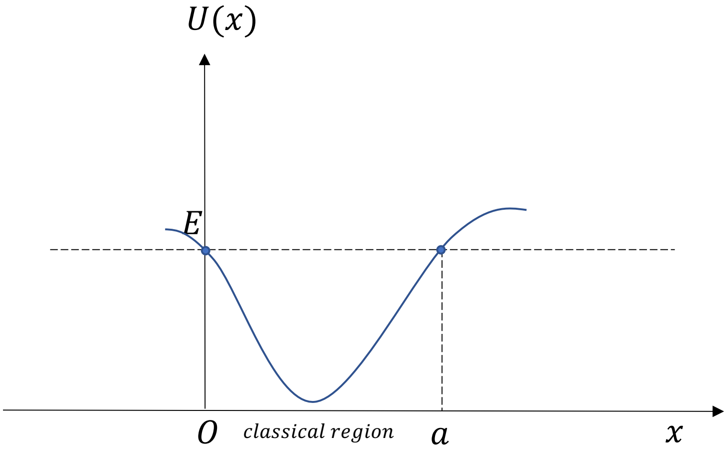

Fig. A.1 Classical region of a particle is moving in a one dimension potential with $E > U(x)$.

where the prime denotes the derivative with respect to x. Substituting this into (A.1), such that

$$A'' + 2iA'\phi' + iA\phi'' - A\phi'^2 = -\frac{\omega^2}{\hbar^2}A \tag{A.4}$$

where the real part is $A'' = A(\phi'^2 - \omega^2/\hbar^2)$ can be solved if we assume $A'' \sim 0$ (we assume that the amplitude A varies slowly), then $\phi'^2 - \omega^2/\hbar^2 = 0 \Longrightarrow \phi(x) = \pm\frac{1}{\hbar}\int \omega\ dx$. The imaginary part $2A'\phi' + A\phi'' = 0$ gives the exact form of $A = C/\sqrt{\phi'}$, with C is a constant. Recall that we start with $\psi(x) = A(x)e^{i\phi(x)}$, we then have the WKB approximation of the wave function is

$$\psi(x) \cong \frac{C}{\sqrt{\omega(x)}}e^{\pm\frac{i}{\hbar}\int \omega(x)\ dx} \tag{A.5}$$

We call this the “classical" region as the particle’s motion is only allowed in this region, $0 < x < a$. There are two turning points defined by $U(x) = E$, which are $x = 0$ or $x = a$.

In contrast, for $E < U(x)$, the region where $0 < x < a$ is non-classical. In this case, the tunnelling is switched on, and the corresponding result is

$$\psi(x) \approx \frac{C}{\sqrt{k(x)}}e^{\pm\frac{1}{\hbar}\int k(x)\ dx} \tag{A.6}$$

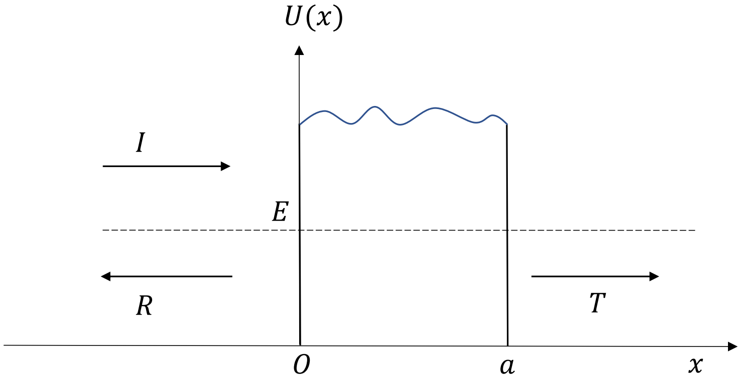

Fig. A.2 Scattering from a rectangular barrier with a bumpy top

and the kinetic energy will be imaginary. Considering a rectangular barrier with a bumpy top of Fig. A.2, we have

$$\begin{cases} \psi(x<0) = & Ie^{i\omega x} + Re^{-i\omega x} \\ \psi(0<x<a) = & C_1 e^{kx} + C_2 e^{-kx} \\ \psi(x>a) = & Te^{i\omega x} \end{cases} \tag{A.7}$$

where we assume the particle is moving from the left to the right of the potential. The probability that a particle tunnels through the barrier is given by

$$\Gamma = \frac{|T|^2}{|I|^2} \tag{A.8}$$

If the barrier is very high and/or very wide (which is to say, if the probability of tunnelling is small), then the coefficient of the exponentially increasing term C_1 must be small or even zero for infinitely broad barriers. The relative amplitudes of the incident and transmitted waves are determined essentially by the total decrease of the exponential over the nonclassical region,

$$\frac{|T|}{|I|} = exp\left(-\frac{1}{\hbar}\int_0^a |k(x)|\,dx\right) \tag{A.9}$$

and

$$\Gamma \cong e^{-2\gamma}, \quad \text{with} \quad \gamma \equiv \frac{1}{\hbar}\int_0^a |k(x)|\,dx \tag{A.10}$$

Appendix B

Conical deficit

For the seeded vacuum decay, one may encounter a conical singularity at the centre of Euclidean space $r = r_h$ when the periodicity β differs from the natural periodicity of the black hole geometry, $\beta_0 = 4\pi/f(r_h)$. In this appendix, we provided a detailed computation of a conical deficit action. We consider the following metric

$$ds^2 = d\rho^2 + A^2(\rho)d\chi^2 + C^2(\rho)d\Omega_H{}^2, \tag{B.1}$$

where we assume the conical deficit in a 2-plane, parametrized by local cylindrical coordinates $\{\rho, \chi\}$, with a conical singularity residues at $\rho \to 0$. H is the transverse space, which is independent of these coordinates, such that we have $C'(0) = 0$.

We integrate from a proper distance ε from the horizon and take $A'(0) = 1$, $A'(\varepsilon) = (1-\delta)$, where $\mathcal{A}$ and δ are defined as the area of the conical deficit and the deficit angle respectively. We then smooth out the conical deficit in the proper distance $\rho < \varepsilon$ from the horizon. The Ricci scalar is calculated by substituting the metric (B.1) as

$$\mathcal{R} = -2\frac{A''}{A} - 4\left(\frac{A'C'}{AC} - \frac{C''}{C}\right) + 2\frac{(1-C'^2)}{C^2} \tag{B.2}$$

Taking the limit of $\varepsilon \to 0$, only the A''/A term contributes to the integral as $A'' = O((A'(\epsilon) - A'(0))/\epsilon)$. The overall contribution of the conical deficit can be given by

$$\int_{\rho<\varepsilon} d^4x\sqrt{g}\,\mathcal{R} \sim \mathcal{A}[A'(0) - A'(\varepsilon)] = 4\pi\delta\mathcal{A} \tag{B.3}$$

To get the contribution from the Gibbons-Hawking boundary term, we compute the extrinsic curvature $K = -A'/A - 4C'/C$, which gives the following contribution

$$\int_{\rho=\varepsilon} d\chi d\Omega_H A C^2 K \; -2\pi\mathcal{A}A'(\varepsilon) = -2\pi\mathcal{A}(1-\delta) \tag{B.4}$$

Note that we neglect higher orders of ε as it is small.

Finally, we conclude that the contribution from the conical deficit cancels out, and the overall action is

$$I_{\mathcal{B}} = -\frac{1}{16\pi G}\int d^4x\,\sqrt{g}\,\mathcal{R} + \frac{1}{8\pi G}\int d^3x\,K = -\frac{\mathcal{A}}{4G} \tag{B.5}$$